Manufacturing and Mechanical Testing of Composite T-Joints with Carbon Nanotube Interleaves

Master of Science Thesis

Danyu Qiao

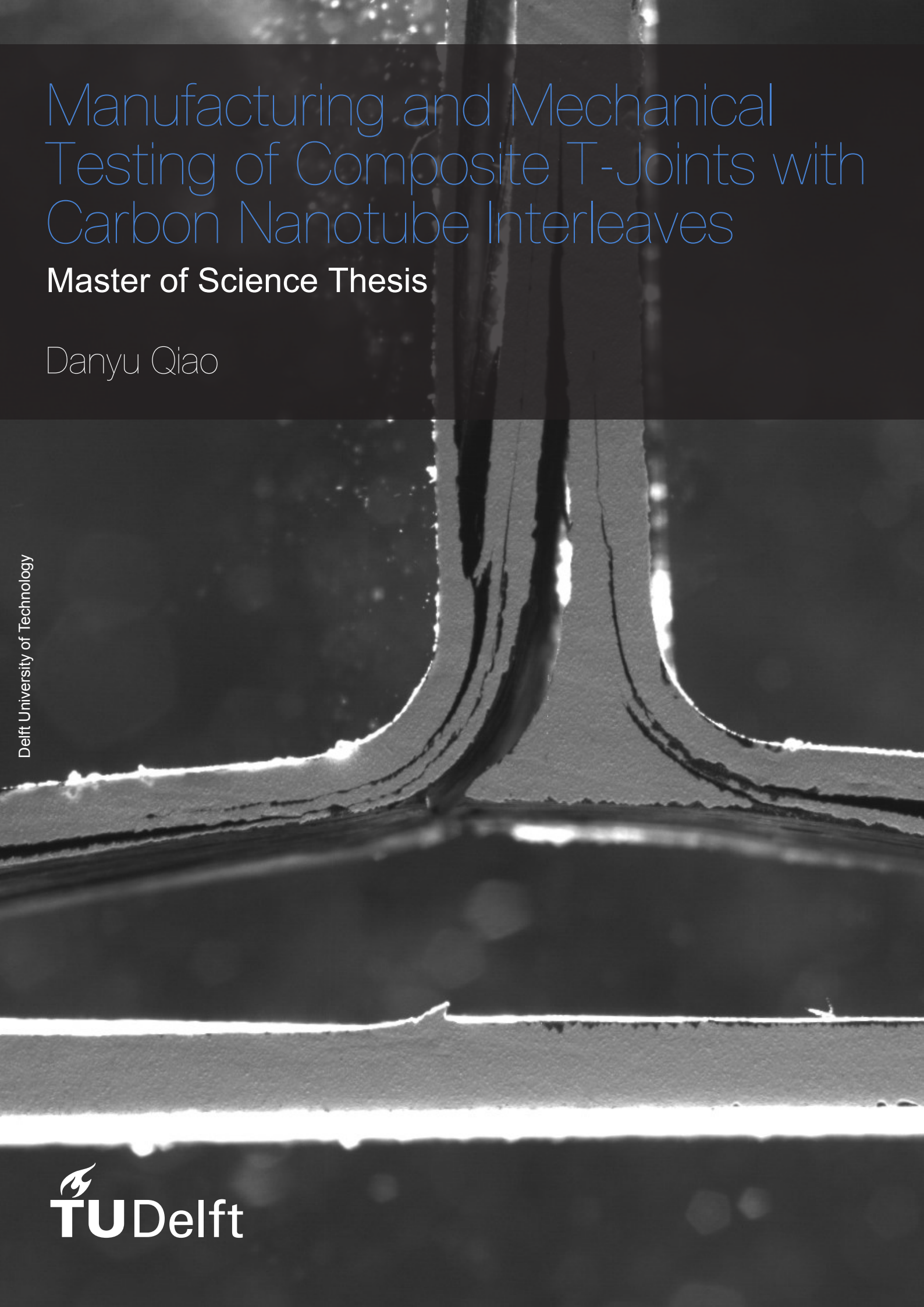

Delft University of Technology

TU Delft

Manufacturing and Mechanical Testing of Composite T-Joints with Carbon Nanotube Interleaves

Master of Science Thesis

by

Danyu Qiao

to obtain the degree of Master of Science
at the Delft University of Technology,
to be defended publicly on Friday November 18, 2022 at 12:00 PM.

Student number:	5245273	
Project duration:	November 25, 2021 – November 18, 2022	
Thesis committee:	Prof. Dr. C. Bisagni	TU Delft, supervisor
	Dr. Ir. D.M.J. Peeters	TU Delft
	Dr. K. Masania	TU Delft
	Dr. N. Subramanian	TU Delft

TU Delft

Preface

This thesis is dedicated to all the people who have been and continue to be my source of inspiration.

I am forever indebted to my supervisors, Chiara and Nithya, for the opportunity of this thesis. I could not have completed the journey without their most patient guidance and unwavering support.

I would also like to express my deepest appreciation to my defence committee members, Dr. Ir. Daniël Peeters and Dr. Kunal Masania, for generously lending their knowledge and expertise.

Special thanks to members of the research group for sharing their own journeys into science with me. To Arne, especially, for his invaluable advice.

None of my experiments would have worked out without the heroes in the lab - Victor, Alexander, Dave, Johan, Ed, and Rob. Thank you so much for taking care of me.

A big THANK YOU to my friends in Delft, my little family - Frankie, Sara, Fra, Yazzy, Lucas and Siti, and my girlfriend Kahina. You have always been there for me and words cannot express how fortunate I am to have you in my life.

And finally, to my parents, thank you for always standing behind me as I continue the pursuit of my ambitions.

What an adventure it has been!

Danyu Qiao
Delft & Voorburg, November 2022

Summary

In recent decades, fibre-reinforced polymer composite structures have seen increased aerospace applications. A typical composite structural element widely used in primary load-bearing aircraft components is the T-joint, which is formed when two orthogonal laminates are joined in a T-shaped arrangement to enable out-of-plane load transfer. Under tensile loading, the structure tends to fail by the separation of the horizontal and vertical laminates at the joining interface. The incorporation of an interleaf, i.e. a thin layer of material with good interfacial bonding properties, may prevent or delay the failure event. A potential interleaf material is the carbon nanotube (CNT). In the literature, its addition as a reinforcing phase in interleaves has been shown to improve fracture toughness in standard coupon tests, but the technique has yet to be tested on a structural element level.

This thesis research investigated the effect of CNT interleaves on the mechanical behaviour of composite T-joints. Manufacturing processes were developed to produce test samples consistent in quality. T-joint samples with CNT-modified interleaves were manufactured alongside neat samples with zero CNT content. The joints were formed using custom-built tools and co-cured in an autoclave. Tensile tests were carried out and the T-joints were loaded until failure. Load-displacement data were acquired and further supported by results from a Digital Image Correlation (DIC) system.

Data analysis suggested that CNT interleaves modified the mechanical behaviour of T-joints by delaying the failure of the structure. While their stiffness and ultimate strength were largely unaltered, the CNT-modified T-joints were able to undergo higher displacements and absorb higher strain energy before failure compared to the neat samples. The delay of failure was enabled by extensive crack development within CNT interleaves preceding the final rupture. In comparison, the neat samples failed abruptly after very limited damage evolution. Observation of the crack surfaces revealed evidence of tortuous crack paths through CNT interleaves. The finding suggests that CNT interleaves are capable of improving the failure resistance of the T-joint structure in a targeted fashion.

Contents

Nomenclature

Abbreviations

Abbreviation	Definition
ASTM	American Society for Testing and Materials
CFRP	Carbon-fibre-reinforced polymer
CNT	Carbon nanotube
CNF	Carbon nanofibre
DCB	Double cantilever beam
DIC	Digital image correlation
ENF	End notched flexure
FRP	Fibre-reinforced polymer
GNP	Graphene nanoplatelet
MMB	Mixed-mode bending
MWCNT	Multi-wall carbon nanotube
PE	Polyethylene
PAN	Polyacrylonitrile
RTM	Resin transfer moulding
SEM	Scanning electron microscope
SHM	Structural health monitoring
SWCNT	Single-wall carbon nanotube
UD	Unidirectional

List of Figures

List of Tables

1

Introduction

Composite materials, specifically carbon-fibre-reinforced polymers (CFRP), are increasingly replacing metals in the production of aerospace structures. Using composite structures, the same load-carrying capacity can be attained with reduced weight. Lighter, more efficient and thus more sustainable structures can therefore be designed. However, traditional engineering practices cannot be easily transferred to cover the new design concerns created by composite materials. For example, mechanical fasteners such as bolts and rivets widely for joining metallic components are not ideal for composite structures, as the fastener holes tend to disrupt fibre continuity and attract stress concentration [1]. Composite materials are also inherently non-homogeneous and are prone to delamination. New manufacturing pathways also need to be developed for CFRP structures, as metalwork processes such as extrusion, casting and sheet forming are not always compatible with composite materials. These concerns pose challenges to the development of composite structures.

One of the structures being increasingly manufactured using composites is the T-joint. It is formed when two orthogonal laminates are connected for out-of-plane load transfer, forming a T shape. The structure can be commonly found in stiffened panels and wing box structures [2], [3]. Figure 1.1 shows a generic T-joint as a constituent element of a wingbox. The horizontal laminate is usually referred to as the skin, to which the orthogonal laminate - the stiffener - is joined. In a typical T-joint construction, the vertical section of the stiffener (the web) splits in the middle to become two flanges that would be joined to the skin. In order to maintain fibre continuity and effective load transfer, a minimum radius needs to be maintained as the web bends to form the flange [4]. This leaves a cavity at the intersection, which is typically filled by a piece of material called the delta fillet. Typically, the delta fillet is produced using resin, continuous fibre or chopped fibre [5].

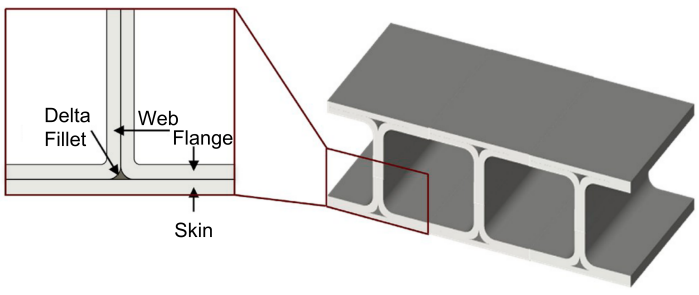

Figure 1.1: T-joint found in a wingbox structure. Image reproduced from Dahmen et al. [3]

The mechanical behaviour of a simplified T-joint element under out-of-plane tensile loading can be effectively evaluated using a stiffener pull-off test configuration. It has been widely adopted by researchers studying the structural element [2], [3], [5]–[15]. During a pull-off test, the flanges and skin are supported while the web is clamped and a tensile load is applied. The resultant stress field usually causes

cracks to initiate within or around the delta fillet region, and then propagate in the form of delaminations between the flange and the skin. Past research has investigated the practice of embedding a thin layer of material in the critical interfaces to change the structure's mechanical behaviour under stiffener pull-off loading [14]–[16]. This layer - called the interleaf - would be produced using material that modifies interfacial bonding properties.

Carbon nanotube (CNT) exhibits the potential for an effective interleaf material owing to its high strength and bonding properties. The nanoparticle consists of carbon atoms linked by double bonds and arranged in the form of a slender tube. The carbon-carbon covalent bonds lead to high tensile strength, while the high surface area relative to the small size of the particle promises high abilities to form bonds with surrounding materials. CNT has proven to have an effect on the elastic properties of polymers [17], [18] and, when introduced into the composite matrix, the damage resistance of composite structures [1]. Epoxy interleaves containing CNT exhibited increased fracture toughness in standard coupon tests [19]. However, it remains to be investigated how the material properties measured on a coupon level will translate into modified mechanical behaviours of a structural element such as the T-joint.

The objective of the current research was to investigate the effect of CNT interleaves on the mechanical behaviour of composite T-joints by developing manufacturing processes capable of producing high-quality test samples. T-joints with CNT interleaves and delta fillets were fabricated, alongside neat samples with zero CNT content. The samples were formed using custom-built tools and co-cured in an autoclave. After post-processing and measurements, the samples were loaded in a stiffener pull-off test setup. Load-displacement data were acquired, supplemented by images captured by a Digital Image Correlation (DIC) system.

Data analysis revealed that the inclusion of CNT interleaves contributed to the delay of structural failure. The CNT-modified samples were able to undergo higher displacements and absorb higher strain energy before failure. The damage delay was enabled by steady crack propagation in the interleaves. In comparison, the control group samples failed explosively at low displacements, after limited visible damage evolution. The tests demonstrated that CNT interleaf is an effective method to improve damage resistance of the T-joint in an efficient and targeted manner.

This report begins by reviewing existing literature in Chapter 2. This is followed by detailed documentation of the design and manufacturing of T-joint samples in Chapter 3. The test setup and procedure are discussed in Chapter 4. Chapter 5 presents the results of data post-processing and analyses the implications. Finally, Chapter 6 reexamines the research effort and discusses potential improvement, as well as offers recommendations for future research.

2

Literature Review

This chapter examines existing literature with the objective of establishing a theoretical basis for the current research. The first section reviews CNT as a reinforcing phase for composite structures. Past and ongoing efforts into the properties and application of CNT are examined. This is followed by an introduction to composite T-joints. Various test schemes to characterise its mechanical properties are discussed, together with existing methods of T-joint reinforcement.

2.1. CNT as a Reinforcing Phase for Composite Structures

This section sets the stage for the research by reviewing the properties of CNT and the various approaches to its application in composite structures, notably in an interleaf format.

2.1.1. CNT: An Overview

CNT falls within a family of carbon-based nanoparticles characterised by their small size (dimension in at least one direction measures less than 100nm) [20]. They are tubes formed by a single layer (single-wall carbon nanotubes, SWCNT) or multiple layers (multi-wall carbon nanotubes, MWCNT) of hexagonally-arranged, doubly bonded carbon atoms, similar to that in a graphene layer. In Figure 2.1 MWCNT are shown under the microscope at different resolutions. Their distinct tubular geometry differentiates them from the other nanoparticles in the same family, including graphene nanoplatelets (GNP), or the much longer carbon nanofibres (CNF). The carbon-carbon covalent bond gives CNT its exceptionally high tensile modulus [21] while the large surface area relative to its small size suggests promising interfacial bonding properties. Moreover, CNT can be functionalised using certain chemicals, e.g. amino groups, to further improve the bonding strength with epoxy [22], [23]. It is therefore not surprising that numerous research projects have selected CNT as a reinforcing phase for fibre-reinforced polymer (FRP) structures. It must be noted, however, that nano-reinforcements have yet to see wider industrial applications due to their relatively high cost [4]. Additionally, the lack of systematic research leads to a large scatter in available data.

Research has shown that CNT can greatly enhance the properties of polymers. Liu et al. [17] reported that by incorporating less than 2 wt.% MWCNT, they were able to increase the tensile modulus of Nylon-6 by 214%, yield strength by 162%, and hardness by 83%. Scanning electron microscope (SEM) images of the dog-bone tensile samples revealed that CNT contributed to the absorption of fracture energy mainly by bridging the cracks, stretching, and finally breaking. Only a few tubes exhibited a pull-out, indicating strong adhesion between CNT and the matrix material. In a similar experiment, Ruan et al. [18] produced a 25% gain in modulus and 47.6% in yield strength by adding 1 wt.% MWCNT to polyethylene (PE). Adopting a different sample format, Weisenberger et al. [24] manufactured polyacrylonitrile (PAN) fibres dispersed with 5 wt% MWCNT, which yielded a 36% improvement in modulus and 46% in yield strength. Zhang et al. [25] investigated the fatigue response of CNT-modified epoxy, and recorded a significant reduction in the crack expansion rate. The enhanced elastic and fatigue properties suggest that CNT-dosed polymer has a high potential for use in FRP structures.

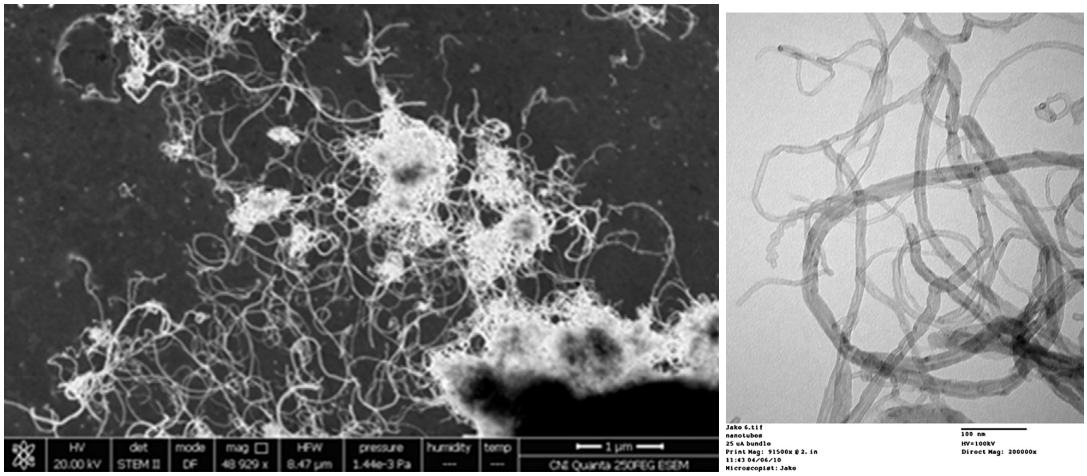

(a) (b)

Figure 2.1: Microscopic images of MWCNT taken at different resolutions. Images copied from Wernik and Meguid [23].

The application of CNT in adhesively bonded structures also showcases its potential. Wernik and Meguid [23] have shown that a critical concentration of CNT dispersed in epoxy adhesives increased the critical strain energy release rate by up to 36% in a coupon test, effectively raising the threshold for crack propagation. However, adhesive bonding does not realise the full potential of CNT as the molecules cannot easily migrate into the fully-cured adherents and form interlinks. Adhesively bonded joints also face certification issues, as they are currently not certified for use in primary structures such as wing boxes and fuselage sections.

It must be noted that all of the works just presented utilised MWCNT to enhance polymers. Experimental research using SWCNT is rather lacking in comparison. Gojny et al. [22] tested low concentrations of SWCNT (0.05-0.3 wt.%) in an epoxy matrix and significant improvements in strength and modulus were observed. It was reasoned that the contrast between high gains and low concentration was a result of the absence of inactive inner layers. Han and Elliott [26] constructed molecular dynamics models of a unit cell containing one SWCNT enclosed by polymers and obtained results showing a drastic increase in tensile modulus in the longitudinal direction, coupled with a slight increase in the transverse direction. Despite these positive indications, the challenges involved in the manufacturing and dispersion of SWCNT likely led to less attention in the literature.

2.1.2. Influence of CNT Morphology

CNT morphology, which refers to the amount, dispersion, positioning, and, when it can be adjusted in a controlled manner, the orientation of the nanoparticle, has been shown to affect the behaviour of CNT-modified materials.

The general trend observed in the literature has been improvements in material properties with increasing CNT content until an optimal concentration is reached. Beyond the tipping point, properties will begin to degrade as more CNT are added. This trend is reflected in Figure 2.2, which shows the relationship between CNT concentration and the tensile strength of adhesive material. Two curves represent samples with and without Polyvinylpyrrolidone (PVP), a surfactant used to disperse and stabilise CNT. In this study, an optimal CNT concentration of 1.5 wt.% yielded a 25% gain in tensile strength. The optimal concentration tends to vary between studies depending on the CNT integration method, material combination, and the material property in question, although it seems that a range of 0-3 wt.% CNT is enough to experimentally capture the tipping point. The trend has been observed by Wernik and Meguid [23] and Gojny et al. [22]. Drawing observations from micrographs of material samples, the former attributed the reversal to the increased resin viscosity with the addition of more CNT, which renders the dispersion method (ultrasonication in this case) less effective. Large agglomerations could be observed in samples with high CNT content. The formation of agglomerates not only deprives the surrounding matrix of reinforcing CNT but also causes incomplete resin impregnation, which can be

considered a defect [22]. Models constructed by Subramanian et al. [27] further confirmed the existence of an optimal CNT concentration, albeit at a higher 6 wt.%, beyond which ineffective load transfer caused by large CNT agglomerates degraded the matrix properties.

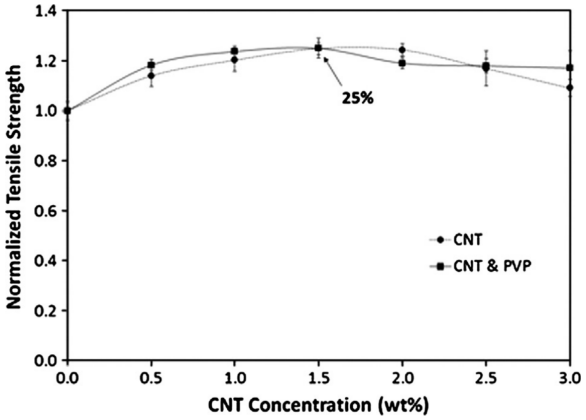

Figure 2.2: Influence of CNT content on material tensile strength. Image copied from Wernik and Meguid [23].

The positioning and orientation of CNT can also be optimised within a structural element. Strategic non-uniform placement of CNT has been shown to modify the structural behaviours better than uniform dispersion [28]–[30]. Modelling an open hole structure under tensile loading, the researchers optimised the spatial positioning and orientation of CNT networks. The algorithm directed higher CNT content to locations of stress concentration, allowing more CNT to engage in stress diffusion and crack branching. The simulation demonstrated significantly more effective suppression of stress concentrations compared to homogenised CNT placement. That being said, it remains to be seen how the optimised CNT orientation and non-homogeneous positioning can be achieved in practice.

2.1.3. Standard Tests for Interface Toughness Characterisation

Before delving into the application of CNT to fibre-reinforced composites, an account of standard coupon tests for interfacial fracture toughness, which are frequently used in the literature to evaluate the CNT-modified composites, is first given to equip the reader with the necessary background knowledge.

Most authors reviewed followed the American Society for Testing and Materials (ASTM) standards: D5528 for the double cantilever beam (DCB) test [31], and D7905/D7905M for the end-notched flexure (ENF) test [32]. These tests are intended for the evaluation of fracture toughness under mode I fracture (crack opening under out-of-plane tensile load), and mode II fracture (crack opening under in-plane shear load), respectively. The samples for DCB and ENF tests, as well as their respective test setup, are shown in Figure 2.3. In the DCB test, the out-of-plane load is introduced via hinge blocks bonded to the face of the specimen, while the ENF test uses rollers to generate in-plane shear loading.

All test standards require the sample to be manufactured out of unidirectional (UD) laminates to eliminate the effect of coupled deformation and ensure a straight crack front. A pre-crack is embedded in the mid-plane to control the location of damage initiation in a precise manner. Using the load, displacement and crack length data obtained from the tests, fracture toughness under the respective crack opening mode can be calculated. The values enable the evaluation of damage resistance capabilities across different materials.

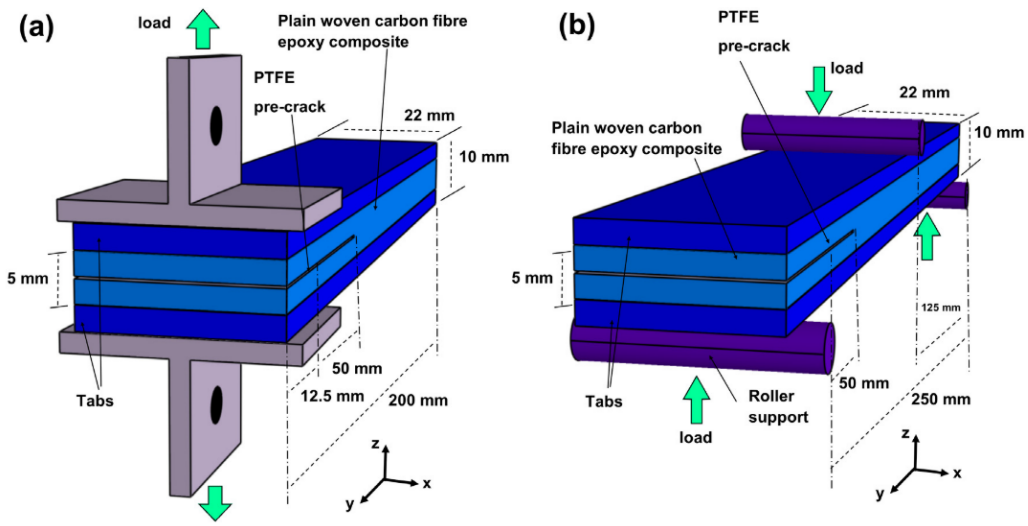

Figure 2.3: Schematic of (a) double cantilever beam (DCB) [31] and (b) end notch flexure (ENF) [32] test setup. Image copied from Ravindran et al. [1]

2.1.4. Application of CNT in Composite Structures

This section discusses two methods through which CNT can be applied to composite structures: as a component in the matrix, and as an interleaf.

CNT-Modified FRP Matrix

CNT can be mixed into the epoxy resin matrix of composite materials. Ravindran et al. [1] impregnated fibres with CNT-modified resin in a vacuum infusion process. ENF and DCB tests showed significant improvement in mode II fracture toughness, and a slight gain in mode I. Various toughening mechanisms could be observed from the fracture surface, notably interfacial debonding between CNT and resin, plastic void growth, and CNT pull-out and rupture.

The disadvantage of this CNT integration approach lies in its low efficiency. While CNT has been shown to also modify the tensile modulus of polymers, it does little to change the stiffness of composite laminates because the latter is largely dominated by continuous fibres [1], [33]–[35]. This makes the improved fracture toughness of CNT-modified material the more relevant property in the context of polymer composites. As CNT in the composite remains largely dormant until damage occurs, it would be a more sensible practice to strategically direct more CNT towards locations where stress concentration and damage are predicted than to distribute them evenly across the structure, especially considering the high cost of CNT. One way to achieve such targeted CNT distribution is the placement of interleaves.

CNT Interleaf

An interleaf, in the context of fibre matrix composites, refers to a thin layer of material introduced in between fibre plies. The interleaf can be introduced during the layup step between uncured laminates and integrated by co-curing. Existing literature saw CNT incorporated as a sprayed-on layer and in the form of film interleaves.

A spray-on method was adopted by Li et al. [14] to introduce a layer of MWCNT between laminates. CNT were dispersed in a solvent and sprayed onto the surface of carbon fibre prepreg using the technique from [36], then co-cured into the structure. The researchers recorded a 26.3% increase in mode I ultimate tensile strength, and 23.4% in single lap shear strength. However, the test results cannot easily be compared to other's works as the ASTM standards were not followed.

Film interleaves, which refer to a polymer film embedded between plies [37], represent an easier method to integrate CNT in FRP structures. Compared to the spray-on technique, polymer film interleaves facilitate a more uniform dispersion of CNT across the surface. Grimsley et al. [21] manu-

factured DCB and ENF test samples using Hexcel IM7/8552 carbon fibre prepreg with epoxy interleaf containing CNT. While it would be desirable to match the interleaf material properties with the prepreg matrix as closely as possible, the authors were unable to obtain neat Hexcel 8552 resin, and thus opted for toughened epoxy API-60 with similar properties. The interleaves were prepared by manually coating pre-fabricated CNT sheets with API-60 resin. While the inclusion of CNT interleaves almost doubled the mode II fracture toughness, the mode I fracture toughness value was halved compared to the control group. The low mode I toughness was attributed to poor CNT-epoxy adhesion within the interleaf, as confirmed by microscopic fractography. Widespread CNT pull-out was observed on the fracture surface whereas no sign of CNT breakage could be found.

More recently, manufacturing techniques were developed to improve the quality and facilitate the handling of CNT-epoxy interleaves. One disadvantage of uncured epoxy interleaves is difficulty in maintaining constant thickness. In the previously discussed study by Grimsley et al. [21], the thickness of the uncured epoxy interleaf was controlled by mere visual inspection. The epoxy's tendency to flow could further distort the thickness profile of the interleaf during integration with the laminate. Subramanian and Bisagni [38] addressed the issues by introducing a semi-curing (also called B-staging) step. Oven cycles were developed to push epoxy interleaves into a degree of cure between 30% and 35%. This value was low enough to allow laminates containing the interleaf to still be certified as co-cured structures, but rendered the epoxy stiff enough such that the interleaves could easily be removed from its linings and placed within the CFRP layup while retaining their thickness. The method was first proven effective based on two neat epoxy systems without any CNT content. DCB and ENF test samples were manufactured, with a pre-crack-inducing Teflon inserted according to the standards to initiate failure in the interleaf layer. Figure 2.4 shows a cross-section of the DCB sample. UD prepreg plies can be seen around the interleaf in the middle. To the left of the interleaf is the Teflon insert.

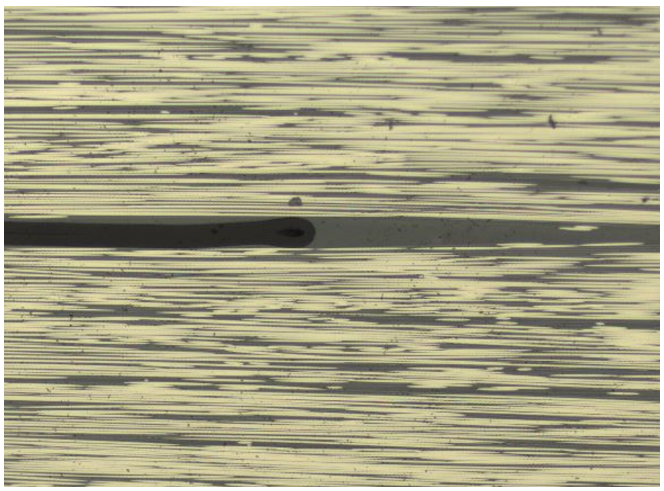

Figure 2.4: DCB coupon cross-section showing neat epoxy interleaf and Teflon precrack. Image courtesy of Nithya Subramanian

The semi-curing method was then tested on CNT-modified epoxy interleaves [19]. DCB coupons containing interleaves with various CNT content (0.5%, 1% and 2% by weight) and thickness (200µ and 500µ) were manufactured. The test results were compared against the baseline coupons containing 200µ neat epoxy interleaves. At 200µ thickness, CNT-modified interleaves doubled mode I fracture toughness irrespective of CNT concentration. At 500µ, the most significant improvements were observed in the coupons with 1% CNT interleaves, which exhibited up to four times higher mode I fracture toughness. A two-scale crack delay behaviour activated by CNT interleaves was observed. On the macro scale, the crack front was repeatedly arrested and released, forming multiple load peaks and drops. On the micro scale, undulations could be observed in the residual interleaf on the crack surface, which indicate tortuous crack paths.

The current research further explores the application of CNT interleaves by following the building block

approach of airworthiness certification [39]. As visualised by the pyramid of tests in Figure 2.5, coupons form the bottom level of the certification process. Previous investigations within the research group [19], [38] completed this step by characterising the mode I fracture toughness of CNT interleaves. This research expands into the second level (elements) by implementing the interleaves into a T-joint - an element with slightly more complex geometry that represents a simplification of detailed structural designs.

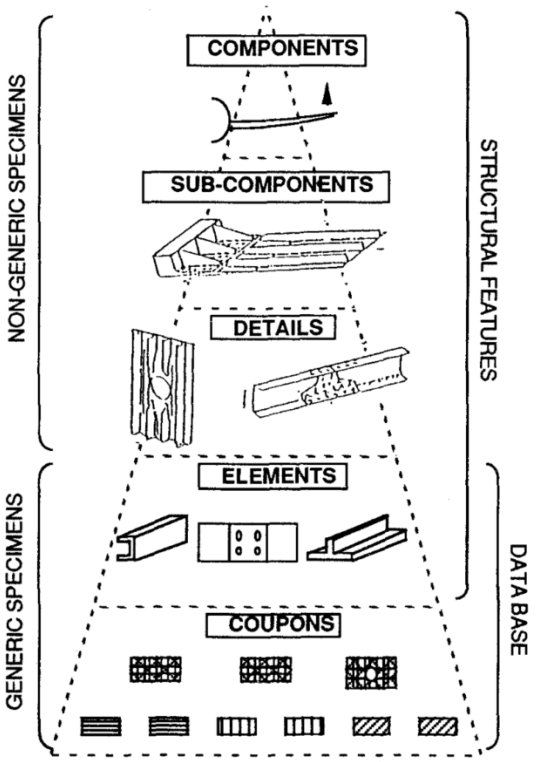

Figure 2.5: Test pyramid for airworthiness approval. Image copied from Rouchon [39]

2.1.5. Extended Functions of CNT

The many non-mechanical properties of CNT further add to its potential as a functional phase in aerospace composite structures. Some of these functions are briefly summarised as they are worthy of future exploration.

CNT can potentially be utilised to improve the quality of composite products. Hank et al. [40] demonstrated that the inclusion of a nanofibre network between prepreg plies can effectively reduce the void content through the capillary effect. Lee et al. [41] tested the same concept by placing a layer of vertically aligned CNT between plies of a Hexcel AS4/8552 prepreg laminate, which was then cured in a vacuum bag-only process. The void content of the product was comparable to that produced by an autoclave. The function promises to free designers from the size constraint imposed by the autoclave.

The excellent electrical and thermal conductivity of CNT also implies interesting applications. Yao et al. [42] investigated an aircraft de-icing system using highly aligned CNT. Show et al. [43] produced an anti-corrosion coating using CNT. Sanchez-Romate et al. [44] suggested the use of CNT as an apparatus for structural health monitoring (SHM). As cracks propagate within a CNT layer, the electrical resistance increases and measurements can be interpreted to indicate crack lengths. Similar experiments were conducted by Wan et al. [8]. Grimsley et al. [21] proved that the inclusion of CNT interleaves significantly improved the electrical conductivity of CFRP structures. The method sees potential application in aircraft lightning strike mitigation, replacing the copper mesh currently in use.

2.2. Composite T-Joint and its Reinforcement

This section discusses the T-joint - the structural element on which the application of CNT interleaves would be tested. A T-joint is formed when two composite laminates are joined at a right angle to transfer out-of-plane loads. It sees wide application in aerospace structures such as fuselage stiffened panels and wing boxes [2], [3]. The joint type is also common in, among others, the naval, automotive, civil, and wind energy industries [1], [5], [13], [45].

The typical FRP T-joint between two orthogonal laminates is shown in Figure 1.1, as a constituent element of a wingbox. The horizontal laminate is often called skin or platform, on top of which a stiffener (also called stringer) stands. The stiffener consists of two L-shaped half laminates placed back-to-back. The segment of the stiffener in contact with the skin is termed the flange, while the free-standing part is referred to as the web. The intersection between the web and the flange forms a delta region not filled by the FRP plies. Typically, this delta region is filled by a fillet of neat resin, continuous fibre composite or chopped fibre composite material [5].

2.2.1. T-Joint Configuration

The T-joint's configuration is a direct reflection of the characteristics of composite materials. As fibres are the main load-carrying elements within FRP materials, the plies cannot be bent to form sharp right angles because doing so poses the risk of damaging fibres [4]. Instead, a curvature should be formed, as is the case with the stiffener laminate in Figure 1.1. A delta fillet is therefore necessary, as it helps define the curvature of surrounding plies and ensures continuity of load transfer [3].

Alternative FRP T-joint configurations have also been investigated by researchers. Two examples are shown in Figure 2.6. In Figure 2.6a, Qin et al. [46] placed a U-shaped end cap around the vertical web segment, forming two delta fillets on either side of the web. By contrast, Phillips and Shenoi [47] embedded the web member partially in the single delta fillet, as shown in Figure 2.6b. Both designs made use of separate laminates to form the web and flanges, with overlaminates supporting the web from both sides.

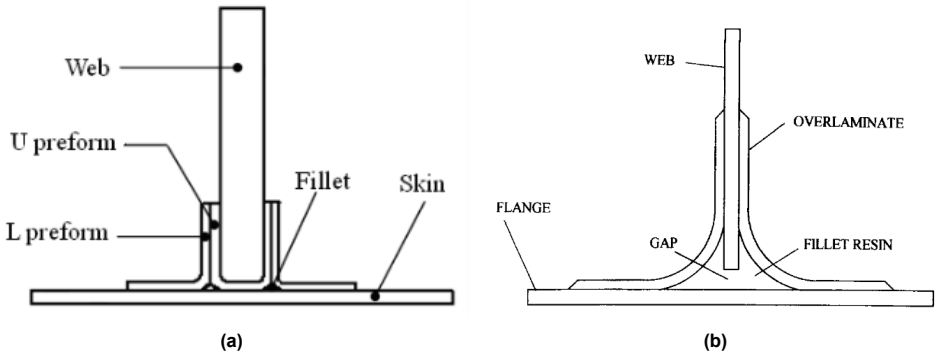

Figure 2.6: Alternative T-joint layouts from (a) Qin et al. [46] and (b) Phillips and Shenoi [47] and Shenoi and Hawkins [48]

Competing delta fillet profiles also exist. Figure 2.7 shows four possible profiles. The triangular profile has three straight sides, while the circular profile replaces two straight sides with circular curves tangent to the web and the flange. The sides can also be defined by more complex curves, as is the case for the elliptical and modified elliptical delta fillets. Cope and Pipes [49] demonstrated that the circular profile increased T-joint strength compared to the triangular profile, while Panigrahi and Pradhan [50] found that the modified elliptical shape seems to most effectively lower interlaminar normal stress compared to all alternatives.

The T-joint configuration with a circular delta fillet profile strikes a good balance between joint strength and simplicity. The geometry of the intersection can be defined by only one parameter, i.e. the radius of the circular curve, which facilitates manufacturing and quality control. This configuration also benefits

from ample previous research as it was the one adopted by most authors.

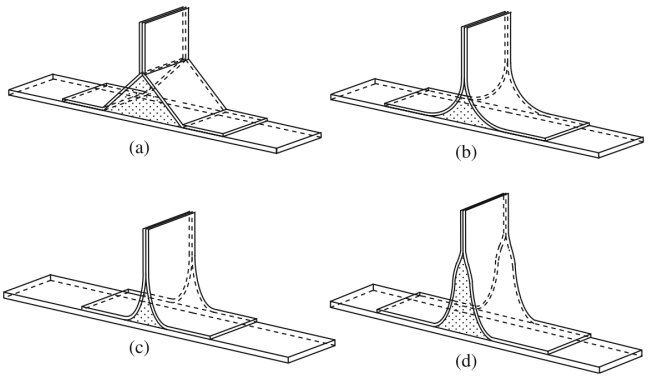

Figure 2.7: Alternative delta fillet profiles. (a) triangular, (b) circular, (c) elliptical, and (d) modified elliptical. Image copied from Panigrahi and Pradhan [50].

2.2.2. Mechanical Testing of Composite T-Joints

Research that investigated the mechanical behaviour of T-joints is reviewed in this section. According to Stickler and Ramulu [2] and Shenoi and Hawkins [48], the joint type can experience a mixture of flexure, tension, and shear in service. The many loading conditions create a scope that is without doubt too broad to be covered by a singular piece of research. The stiffener pull-off test is the focus of the review, as it induces local mode I loading and is therefore the most relevant to the current research built on previous mode I coupon test results.

Stiffener Pull-off Test

Most research papers, in particular the ones geared towards the aerospace industry, chose to apply or model a stiffener pull-off load, or tension load, to the T-joint specimens [2], [3], [5]–[15], [51], [52]. While the exact dimensions and boundary conditions vary, the basic setup can be represented by Figure 2.8, with the skin/flange fixed and a pull-up load applied through the clamped web. The popularity of the test should come as no surprise, as the pull-off test most accurately captures the out-of-plane loads carried by the T-joint as part of aircraft structures.

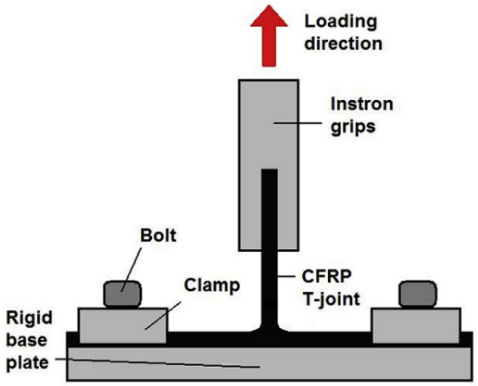

Figure 2.8: T-joint stiffener pull-off test setup from Burns et al. [5]

The choices of materials, boundary conditions, and sample dimensions by various authors are summarised in Table 2.1. As there is currently no commonly recognised standard for T-joint testing [3], a large scatter exists in the choice of parameters. Some authors replaced the clamps with rollers which create a simply supported boundary condition and allow free rotation of the skin and flanges. In some cases, the flanges terminated before the supports, while in others they extended until the edge of the

skin such that the flange length was exactly half that of the sample. Unifying rules for the pull-off test sample design could not be extracted from the literature, as it is largely down to the deliberation of individual authors based on factors such as the material and test equipment.

During the pull-off test, the most common failure mode involves crack initiation in or around the delta fillet, and propagation in the stiffener-skin interface, as can be seen in Figure 2.9. It can be observed that crack opening is largely in the direction of tensile load, i.e. mode I, similar to crack propagation in DCB coupons. This makes the stiffener pull-off test a suitable tool for evaluating the effect of CNT interleaves, as it can be reasonably inferred that the failure delay behaviour observed in DCB tests would repeat itself.

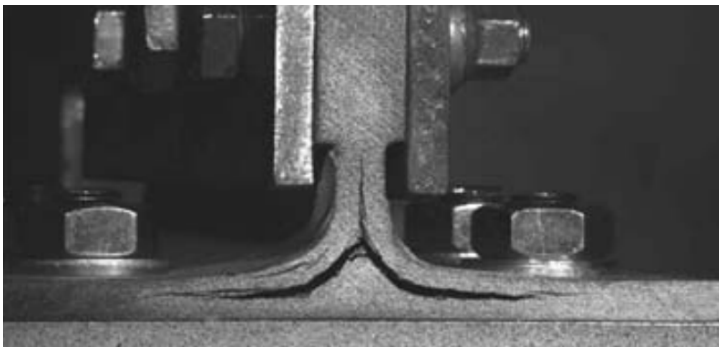

Figure 2.9: Typical T-joint failure mode under pull-off loading. Image copied from Davies and Ankersen [53]

The sample design can affect the failure mode. The mode I scenario just discussed requires the skin laminate to be relatively rigid. If the skin is too flexible and curvature begins to form under the pull-off load, the shear stress component increases which may ultimately induce mode II failure between the flange and the skin [54], [55].

Alternative Tests
While the stiffener pull-off test is the suitable setup to induce local mode I loading, it is by no means the sole test necessary for the full characterisation of a T-joint structural element. Some of the other setups used in the literature to test composite T-joints are briefly summarised below.

- A bending test was used by Stickler et al. [56], and Burns et al. [5]. In their bending test setup (Figure 2.10a), an orthogonal force is applied to the clamped web, causing damage initiation in the radius bend area at the intersection. A hinge integrated into the clamp allows free rotation of the web. The test typically induced multiple delaminations in several ply interfaces within the radius bend, before skin-stiffener separation.

- Focusing on naval applications, Phillips and Shenoi [47] designed the 45-degree pull-off test in Figure 2.10b and the three-point bending test in Figure 2.10c.

- Huang and Hsu [57] evaluated the strength of co-cured J-joints (T-joints with an additional top flange) by applying a downward compressive force onto the web using the setup shown in Figure 2.10d. Since the web was not clamped in this test setup nor was the skin fixed, the load experienced by the joint resembled that of a bending test once buckling in the web occurred.

- The rail shear test was designed by Stickler and Ramulu [2]. The specimen, as shown in Figure 2.10e, was bolted onto a fixtures at the flange while the web was mounted onto a parallel rail though which load was applied. Movements were limited such that only shear loading was introduced.

Table 2.1: T-joint material and geometry chosen by reviewed authors

Source	Burns et al. [5]	Ekermann and Hallström [12]	Sápi et al.[15]	Trask et al. [7]	Bianchi et al. [6]	Li et al. [14]
Material	T700 carbon/ epoxy prepreg tape	HexPly 6376 resin system/ Toho Tenax HTS fibres prepreg	Hexcel HexPly AS4/ 8552 prepreg	Hexcel IM7/ 8552 prepreg	T700 carbon/ epoxy prepreg tape	UD prepreg
Fixture type	clamps	clamps	rollers	rollers	clamps	rollers
Sample length (mm) (between supports)	150	66	80	80	200	150
Flange length (mm) (one side)	32	30	40	40	50	30
Web height (mm) (excluding clamped length)	70	88	40	40	70	80
Sample width (mm)	21	104	25	20	25.5	40
Outer bend radius (mm)	3	3	8	5	N/A	5

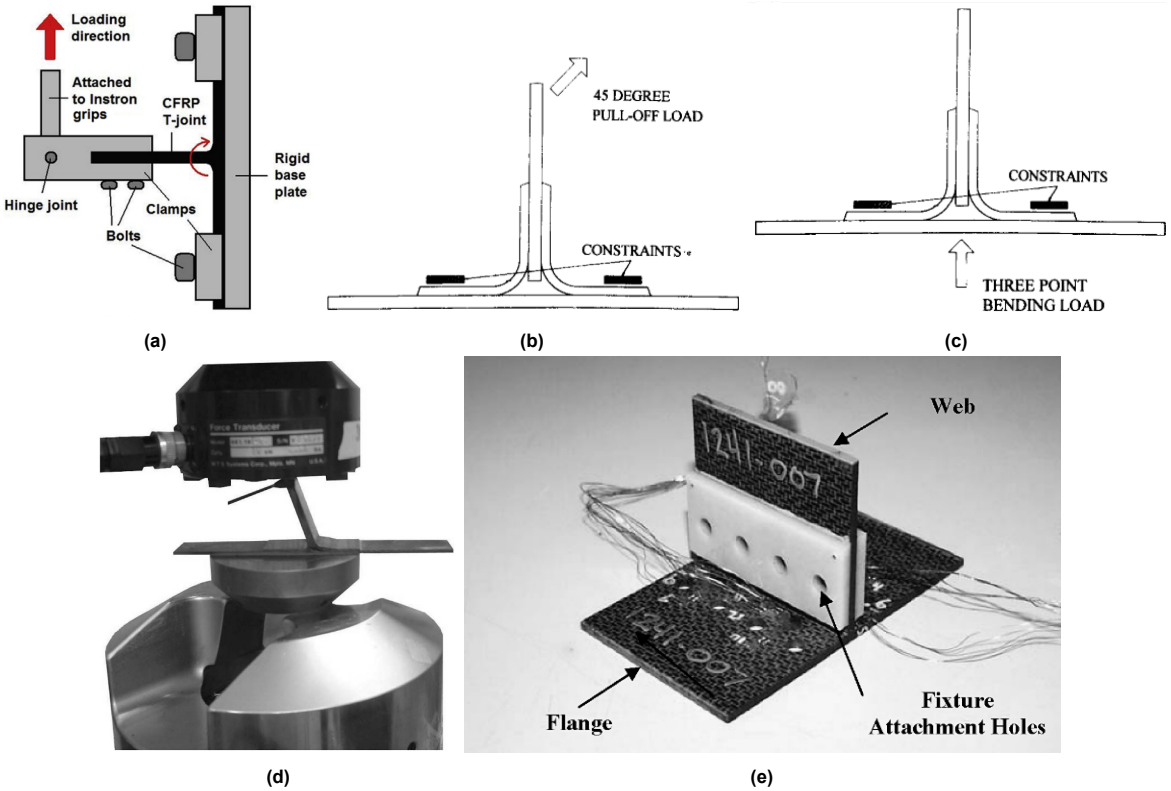

Figure 2.10: Alternative test setup for the evaluation of T-joint mechanical behaviour. (a) Bending test by Burns et al. [5]. (b) 45-degree pull-off test by Phillips and Shenoi [47]. (c) Three-point bending test by Phillips and Shenoi [47]. (d) Compression test by Huang and Hsu [57]. (e) T-joint sample used by Stickler and Ramulu [2] for the rail shear test

2.2.3. Reinforcement of T-Joints

This section reviews methods developed to modify the mechanical behaviour of composite T-joints, as found in the literature. Based on the philosophy they represent, the methods can be loosely categorised into three groups: mechanical fastener, thorough-thickness reinforcement, and the modification of interfacial bonding properties. Past research into the inclusion of CNT (interleaves) in T-joints will be discussed as part of the last category.

Mechanical Fastener

One of the most commonly adopted methods to reinforce a composite T-joint is the use of mechanical fasteners such as bolts and rivets [1]. However, the practice adopted from metallic structures is by no means best suited for FRP laminates. To begin with, metallic fasteners induce weight penalties, offsetting the weight reduction which is a key advantage of composites. They also require drilling holes into laminates, which severs load paths by causing fibre discontinuities and attracts stress concentration [1], [3]. Despite these disadvantages, rivets remain a feature in composite structures as it is a certified approach.

Through-Thickness Reinforcement

It is possible to implement the same philosophy behind the use of mechanical fasteners, i.e. applying high-strength materials in the through-thickness direction to compensate for the weak matrix-dominated properties, while avoiding some of its pitfalls. To be more specific, the problem of severed fibres and open-hole stress concentration can be avoided by making the size of the reinforcing member comparable to individual fibre bundles. Examples reviewed include stitching [10], tufting [58] and z-pinning [6], [58].

Tufting and stitching are both techniques that rely on continuous fibres to strengthen laminates in the through-thickness direction. Cartié et al. [58] modified T-joints with a tufting technique, where a continuous thread was pushed through the dry fibre preform to form individual loops which are then held

in place by friction. A schematic of the process is shown in Figure 2.11a. Pull-off tests showed that crack initiation load and failure mode were unaltered, while the ultimate failure load was almost doubled. In addition, the through-thickness fibres were able to arrest crack propagation to such an extent that the test ended with skin flexure failure rather than stiffener-skin debonding. Stitching enables more complex patterns. The pattern adopted by Bigaud et al. [10] places threads through the delta fillet region for targeted reinforcement, as shown in Figure 2.11b. The stitched specimens showed a 25% improvement in ultimate failure load compared to unstitched samples. Using digital image correlation (DIC) to observe the strain field, they confirmed that stitching aided in the suppression of non-visible damage initiation and consequently the retardation of rupture.

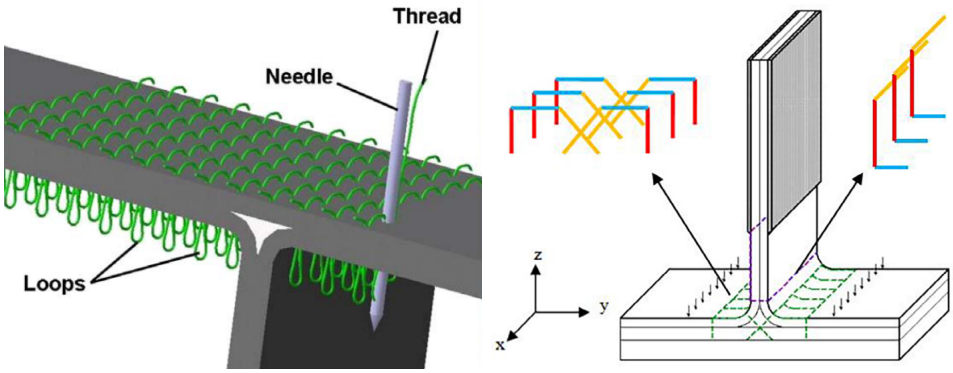

Figure 2.11: (a) Schematic of tufting. Image copied from Cartié et al. [58]. (b) Schematic of stitching. Image copied from Bigaud et al. [10]

Tufting and stitching are limited in their applications in that both processes are intended for dry fibre preforms. Where prepreg tape is used, gaps have to be maintained between neighbouring tapes to form through-thickness holes for the stitching thread [59], which can in turn reduce fibre volume fraction and induce defects.

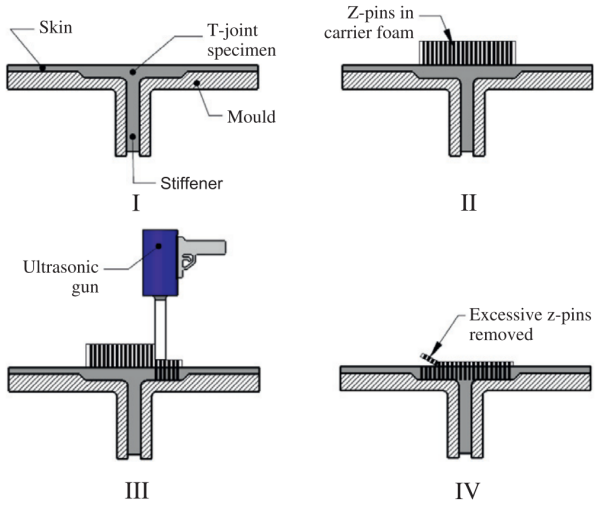

Figure 2.12: Z-pinning to reinforce a T-joint. Image copied from Koh et al. [60]

Z-pinning refers to the insertion of short stiff rods, usually fibres embedded in cured resin, in the orthogonal direction through the stiffener flange and the skin. Unlike stitching and tufting, this method is compatible with prepreg materials. The process is illustrated in Figure 2.12. Z-pins are driven into the laminate at high pressure using an ultrasonic gun. The technique was shown to improve the stiffener pull-off load to different degrees depending on the pinning density. An areal density of 0.5% used by

Cartié et al. [58] yielded a slight increase in the failure load and a 10% increase in the total energy absorbed. The crack initiated in the delta fillet area and, instead of propagating through the flange-skin interface, progressed vertically into the unpinned web. Koh et al. [60] further increased the pinning density to produce higher gains. At a volume content of 4%, the z-pins led to a 76% increase in ultimate load. However, the pins tended to degrade the in-plane properties by causing fibre misalignment and forming resin-rich zones [20], [61].

Modification of Interfacial Bonding Properties

This third category of reinforcement methods contains micro-scale modifications which come rather from a material science point of view. The inclusion of CNT as a matrix component and as an interleaf falls into this family of approaches.

The previously discussed research, which added CNT to the epoxy resin matrix [1], also investigated the application to T-joints. Results showed increased failure initiation load by roughly 30%, and final failure load by around 20%. However, as argued earlier in the chapter, this method lacks in efficiency and economic feasibility as only a small fraction of CNT is engaged in changing the mechanical behaviours.

In contrast to modifying the composite matrix as a whole, interleaves represent a more efficient and targeted way of reinforcing T-joints. Examples of interleaves include high-toughness veils, non-woven mats, and nanoparticles, e.g. CNT. Interleaves can be integrated using two strategies: only in the stringer-skin interface and around the delta fillet, as shown in Figure 2.13a, or in every ply interface as shown in Figure 2.13b. However, the first strategy has received much more attention as it specifically targets the interfaces where damage tends to occur.

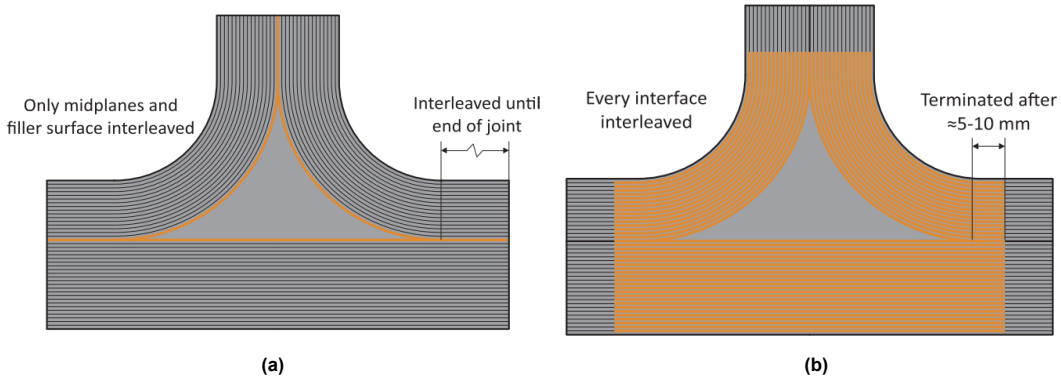

Figure 2.13: Two different interleaf placement strategies: (a) Interleaves around delta fillet and between stiffener and skin. (b) Interleaves in every ply interface. Images copied from Sápi et al. [15]

Research conducted by Wang and Soutis [16] involved the placement of a polyester veil as an interleaf between glass fibre stiffener and skin in order to increase the interlaminar fracture toughness. The joint showed a 44% increase in ultimate pull-off strength compared to the baseline sample without any interleaves. The failure mode remained unaltered compared to the baseline sample (initiation at the delta fillet, propagation first vertically inside the web, then horizontally between the flange and the skin). Sápi et al. [15] tested the performance of a polyamide (PA) non-woven mat co-cured into a T-joint. The samples underperformed by 25% compared to the baseline joint in pull-off tests. It was hypothesised that the interleaved mat was not properly wetted by resin. It was noticed, however, that despite the defect, the PA-interleaved samples were able to absorb a much higher amount of energy after the initial damage.

A sprayed-on CNT interleaf was applied to the T-joint by Li et al. [14]. CNT were deployed in the mid plane of the stiffener web and around the delta fillet, but not between the skin and the stiffener flange, as the buildup in Figure 2.14 shows. The specimens were co-cured and tested using a pull-off setup. The results of the pull-off test showed a higher failure initiation load, as well as an 18.8% increase in

the ultimate failure load. In addition, the location of damage migrated away from the critical interfaces after they were reinforced with interleaves. Unfortunately, this work was not able to explore the effect of CNT embedded in the interface between the skin and the stiffener flange, where damage usually propagates. The spray-on method adopted by the researchers to apply CNT also made it difficult to ensure even dispersion.

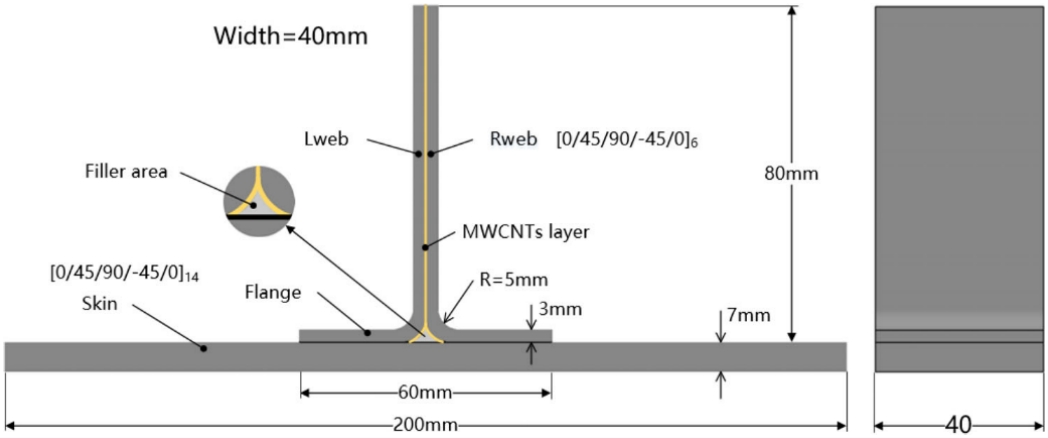

Figure 2.14: Schematic of T-joint buildup with sprayed-on CNT. Image copied from Li et al. [14]

Another application of CNT interleaves to T-joints was carried out by Sápi et al. [15]. The authors placed a forest of vertically aligned CNT around the delta fillet, in the web mid plane, and between the flange and skin, as shown in Figure 2.13a. During pull-off tests, no significant gains could be observed compared to the control group in terms of stiffness, damage initiation load and final failure load. It was hypothesised that the commercial product used as interleaf was not compatible with the Hexcel 8552 resin system.

The examination of the existing literature has led to the identification of a knowledge gap. Namely, a method has yet to be developed to produce composite T-joints reinforced with CNT interleaves of high and consistent enough quality that the effect of CNT could be faithfully quantified. The current research aims to offer a response to the knowledge gap by applying the technique of semi-curing CNT interleaves. The following chapter will document the manufacturing processes specifically developed to produce T-joint test specimens with CNT interleaves.

3

Design and Manufacturing of T-Joint Samples

This chapter presents the design and manufacturing steps of T-joint test samples. A total of five batches, each containing three samples, were produced. The chapter will describe the design of the T-joint sample, document the materials utilised, discuss the design iteration of forming tools, and finally explain the manufacturing steps.

3.1. Sample Design

The fundamental goal of the sample design was to enable the objective evaluation of CNT interleaves' effect on the mechanical behaviour of T-joints under a pull-off loading. This required that samples both with and without CNT interleaves be tested. The manufacturing steps would have to ensure consistent enough quality across specimens such that results from parallel sample groups can be fairly compared. The design should also be compatible with available materials and equipment. With these concerns in mind, the sample design was derived and presented in this section.

3.1.1. Dimensions and Layup

The overall configuration of the T-joint sample followed the most common design found in the literature. An exploded view of the design is shown in Figure 3.1. A flat laminate forms the skin of the joint, on top of which a stiffener stands. Two L-shaped half-laminates combine to form the stiffener. The void at the intersection is occupied by a delta fillet. The fillet has a triangular cross-section with two curved sides to accommodate the curvature of the L-shaped half-laminates. The interleaves are placed in the mid plane of the vertical section of the stiffener (the web), and between the horizontal sections (the flanges) and the skin. As can be seen in Figure 3.1, two pieces of interleaves are introduced with one of them terminating at the joint intersection.

The dimensions of the T-joint were determined by combining findings from the literature with constraints set by available equipment. The samples were designed to be 160mm in length, 90mm in height, and 20mm in width, as shown in Figure 3.2. The length was dictated by the roller fixture available in the laboratory, as shown in Figure 4.1. The two rollers are 10mm in diameter, and spaced 120mm apart. The 160mm length of the sample, therefore, created a 20mm overhang beyond the roller on either side to ensure that the flanges would not detach from the roller despite any slippage that might occur mid-test due to deformation of the sample. Since the load-carrying ability of the T-joint scales with the width, it needed to be designed to accommodate the testing machine. The 20mm width followed Trask et al. [7], whose T-joint samples with similar dimensions sustained maximum loads lower than 1.6kN, well within the capabilities of the 10kN tensile machines used for the tests. The height of the web accounted for 30mm at the tip of the web to be clamped and 60mm loaded.

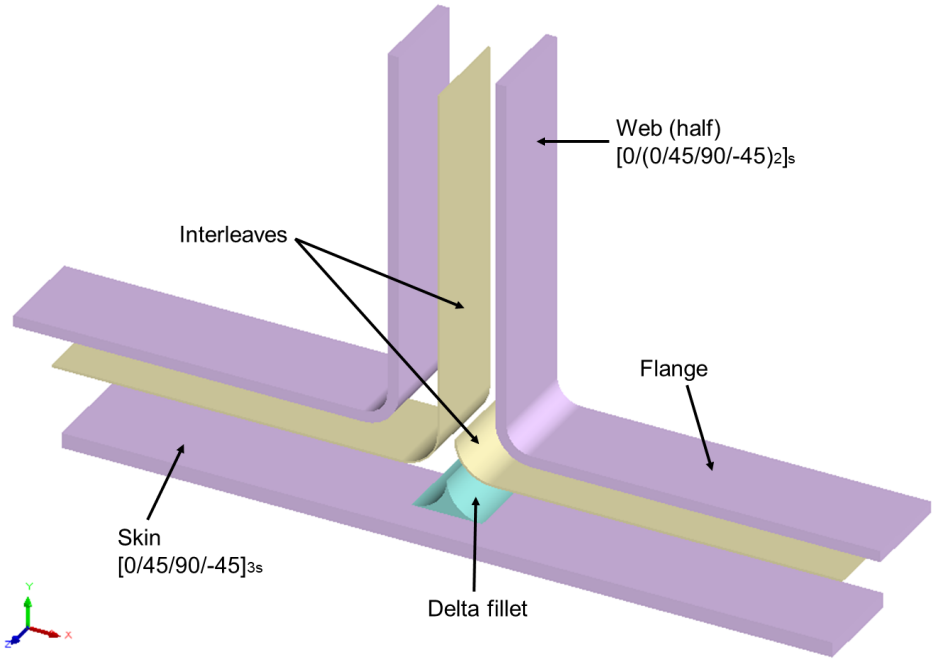

Figure 3.1: Exploded view of the T-joint sample

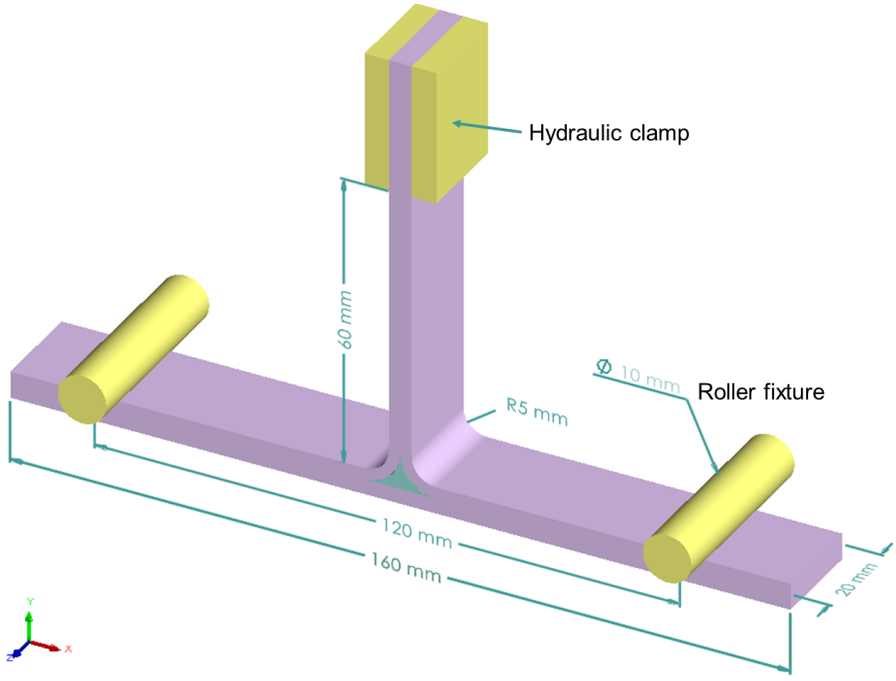

Figure 3.2: Dimensions of the T-joint sample

The layups of constituent laminates were designed in accordance with the rules of quasi-isotropy: balanced, symmetric, with at least 10% of the total plies in every direction and large groupings of similar plies avoided. The layup of the L-shaped laminate which forms half the stiffener was $[0/(0/45/90/-45)_2]_s$, while that of the skin was $[0/45/90/-45]_{3s}$. Here, 0° refers to the lengthwise direction of the samples, i.e. the X-axis direction in Figure 3.2 and Figure 3.1. It can be noted that only 0° plies were

placed at the interfaces with interleaves, in line with the construction of DCB specimens. Since damage arrest and delay mechanisms were observed in the CNT interleaves at the 0/0 interface in previous research [19], [38], a similar interface was maintained to test whether similar mechanisms apply to a structural element with more complex geometry but local mode I loading.

The outer bend radius at the intersection was 5mm, also following the design from the literature [7]. The thickness of the L-shaped laminate (18 plies of Hexcel IM7/8552 prepreg with a 0.131mm nominal ply thickness [62]) brought the inner bend radius up to 7.36mm. This gave the delta fillet a cross-section area of 23.25mm^2.

Accurate control over the sample dimensions was enabled by the manufacturing process summarised in the form of a flow chart in Figure 3.3, with details to follow later in the chapter. The process began with cutting the prepreg plies, which were laid up and debulked. One skin laminate and two stiffener half laminates would be produced this way. The delta fillets and interleaves (when used) were produced in parallel processes and integrated with the laminated to form the T-joint. The assembly was then placed inside a vacuum bag and co-cured in the autoclave. The process up till this point would produce a 180mm-long, 90mm-tall and 90mm-wide T-joint, which was then trimmed and cut to yield a batch of three samples with dimensions conforming to the design. Finally, the samples were polished and measurements were taken.

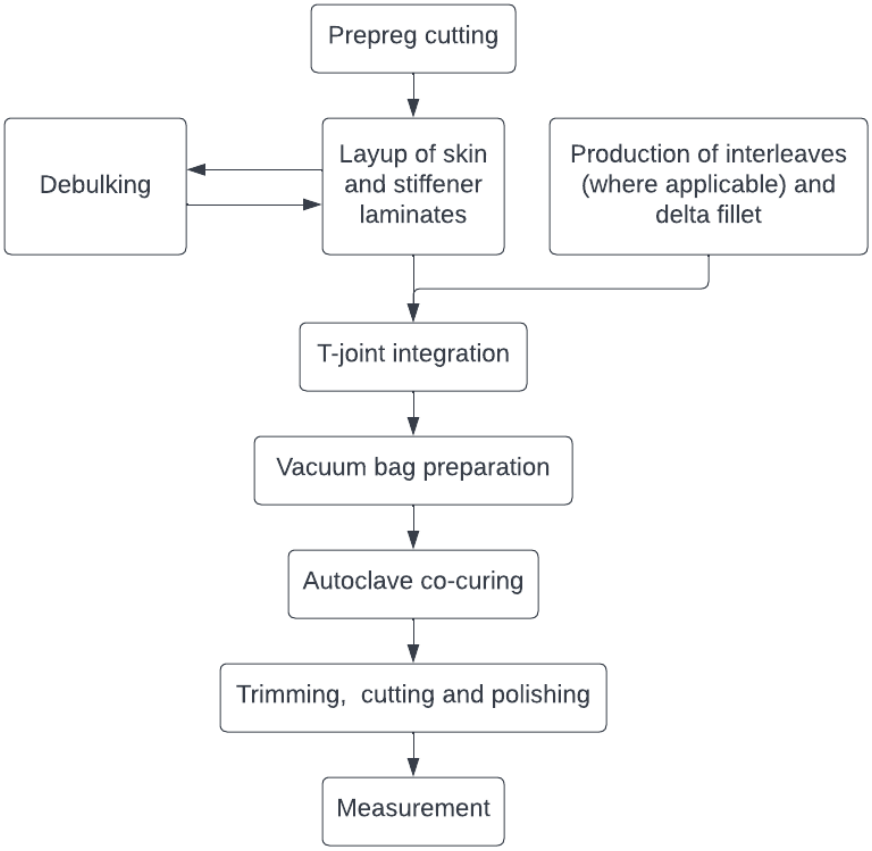

Figure 3.3: Manufacturing flow chart

3.1.2. Sample Groups

A total of five batches were produced and numbered from 1 to 5. Details of the groups are given in Table 3.1. Batches 1 to 3 were intended as control group samples, while batches 4 and 5 were test

groups containing CNT interleaves. The numbering system serves to facilitate the reader's understanding but does not indicate the order of manufacturing (the batches were in fact produced in the order of 1 - 4 - 2 - 5 - 3). A nomenclature is also assigned to each group.

T-joint 1 samples were produced without any interleaf and were intended to serve as the baseline reference. T-joints 2, 3 and 4 all contained 200µ thick interleaves, such that the effect of the interleaf layer on the thickness of the laminate and its stiffness was also controlled. Interleaves made from neat API-60 epoxy were used in T-joints 2 and 3, while T-joints 4 and 5 contained interleaves modified by 1% CNT by weight. Thicker 500µ CNT interleaves were placed inside T-joint 5 samples.

The decision to use CNT interleaves with the same 1% CNT content and different thicknesses was supported by previous research, which showed the most increase in mode I fracture toughness being achieved by 1% interleaves [19]. At this concentration, the thickness of interleaves had a strong effect on fracture toughness: the value almost doubled when 500µ interleaves were used instead of 200µ ones. Therefore, it was decided to investigate the effect of interleaf thickness, while keeping the CNT concentration constant across the CNT-modified sample groups.

The control group samples contained delta fillets produced from neat API-60 epoxy (T-joint 1 and 2) or UD prepreg (T-joint 3), which reflects common practice [5]. The group with UD prepreg delta fillet was added after the observation of severe defects in the neat epoxy fillet samples. Details on the sample quality are given in Chapter 5. In comparison, a CNT-modified epoxy paste was used to make the fillets in T-joint 4 and 5.

Table 3.1: Sample groups and their respective interleaf and fillet materials

Group code	Nomenclature	Interleaf	Delta fillet
T-joint 1	NoInterleaf	None	Neat API-60 epoxy
T-joint 2	200µNeat	200µ neat API-60 epoxy	Neat API-60 epoxy
T-joint 3	200µNeat-FibreFillet	200µ neat API-60 epoxy	UD IM7/8552 prepreg
T-joint 4	200µCNT	200µ 1% CNT-modified epoxy	CNT-modified epoxy paste
T-joint 5	500µCNT	500µ 1% CNT-modified epoxy	CNT-modified epoxy paste

After quality inspection, it was found that only T-joints 3, 4 and 5 were of quality consistent enough for a fair comparison to be made. Results from T-joint 3 and 4 were expected to show the effect of the inclusion of CNT in the interleaf layer, while T-joints 4 and 5 would help assess the effect of CNT interleaf thickness.

3.2. Materials

The T-joint test samples were manufactured out of carbon fibre prepreg material. The interleaves and delta fillets were produced using neat epoxy or a CNT-modified epoxy compound. The delta fillet in T-joint 3 was also produced with prepreg.

The carbon fibre prepreg was IM7/8552 supplied by Hexcel. The standard autoclave cure cycle of the material, as shown in Figure 3.4, has a maximum temperature of 180°C and a pressure of 7 bar [62]. A nominal ply thickness of 0.131mm, as given by the datasheet, was used in the design. Normally stored in the freezer, the prepreg roll was left at room temperature for around 16 hours to defrost before cutting.

The API-60 resin supplied by Kaneka Aerospace LLC [63] was selected for manufacturing the delta fillets and interleaves of control group T-joints. The product consists of a highly viscous liquid part A and a powdered part B. The two-part epoxy resin was chosen for its mechanical properties and cure cycle (maximum temperature 177°C) which closely match those of the Hexcel 8552 resin system. In addition, previous research [19], [38] already successfully demonstrated that API-60 can be semi-cured

(B-staged) into a film that could be integrated into composite laminates as an interleaf. The B-staging cycle was developed to achieve a degree of cure between 30% and 35%, which was low enough for subsequent co-curing cycles but high enough for the interleaf to be handled easily while retaining its uniform thickness.

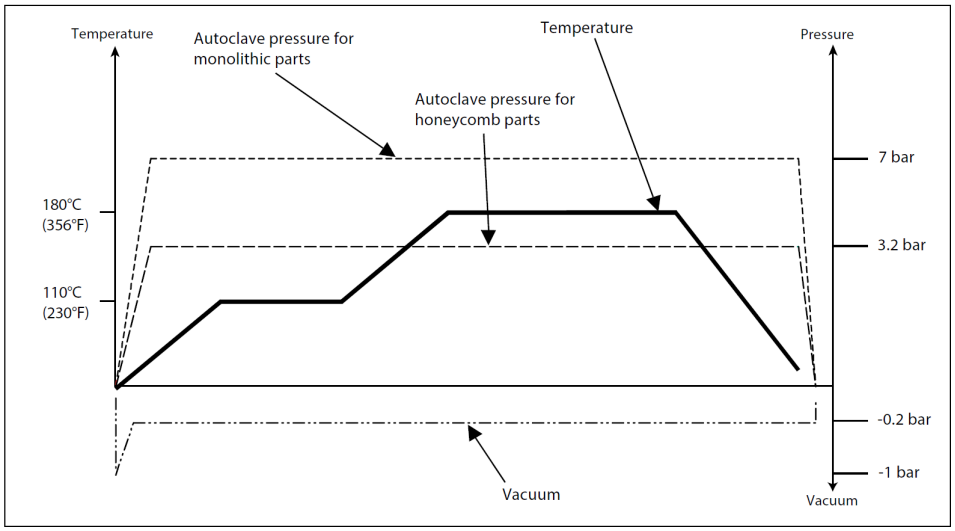

Figure 3.4: Standard autoclave cure cycle of Hexcel IM7/8552. Graph copied from product data sheet [62]

The test group samples with CNT were manufactured using a CNT-modified epoxy custom-made by NanoSperse [64]. It contained MWCNT with random orientation. The material was available in two formats: interleaves and paste. The interleaves were formed through a double nip roll mechanism and sandwiched between two layers of gloss paper. A similar product was manufactured by Shin et al. [65]. At cold storage or room temperature, the gloss paper could not be peeled off the interleaf without causing the uncured epoxy to flow and deform. Through a B-staging process similar to that of the aforementioned neat epoxy interleaves, the CNT interleaves could be partially cured such that they could be easily separated from the gloss paper. The degree of cure at the end of the B-staging process was comparable (30-35%) for both the neat epoxy and CNT interleaves [19]. Combinations of various thicknesses (200µ and 500µ) and CNT concentrations (0.5%, 1%, and 2% by weight) were available. The interleaves contained a proprietary epoxy resin, whose mechanical and cure properties were also compatible with Hexcel 8552, the epoxy system from the carbon fibre prepreg.

Figure 3.5: Strip of CNT-modified epoxy compound

The same material combination (proprietary epoxy and CNT) was also supplied in a paste format, in the form of a bar measuring roughly 40 by 20mm in cross-section, as well as thinner strips with a smaller cross-section of 25mm by 2mm (as shown in Figure 3.5). Compared to the interleaves, the paste had a higher CNT content (5% - 20% by weight). The hardness of the paste was high at its storage temperature (4°C) or even room temperature, making it difficult to cut and reshape. Still, the material quickly softened when heated up to 70°C using a hot air gun. After heating up, the material remained malleable during a brief window for reshaping. The process could be repeated as many times as needed without a noticeable change to the malleability, suggesting that the treatment had a negligible effect on the degree of cure of the epoxy.

3.3. Tool Design Iteration

Despite ample research into T-joints in the literature, the manufacturing steps of T-joints were often not documented in detail. Thus, the design of the forming tools had to go through several rounds of trial and error to ensure the quality of the test samples. The design iterations are briefly discussed here for future reference.

3.3.1. Layup Tools

In the literature, forming of the stiffener half laminates during layup and autoclave curing usually involved the use of metallic blocks [7], [8], [15], [57] or L-shaped caul plates [1], [3]. The caul plate is not an ideal layup tool, as the thickness of the plate is limited by the sheet metal bending process and a thin plate would not remain rigid under pressure during the vacuum debulking step. While metallic forming blocks are much less likely to deform severely, the high thermal inertia of the block can delay the temperature cycle experienced by the laminate, and thus affect the properties of the carbon fibre prepreg. The difference in temperature between the metal blocks and the rest of the autoclave setup would also likely lead to non-uniform heating. In addition, the high cost and long production time also render metallic blocks a less feasible option.

Additive manufacturing was then explored as a more cost-effective alternative with a relatively short production cycle. An Ultimaker 2+ Connect 3D printer based on polylactic acid (PLA) filament extrusion was used. A wedge design was devised as a solution to facilitate layup and debulking. Figure 3.6a shows the part preview in the Ultimaker Cura software interface where the print parameters were set, and Figure 3.6b shows the print being executed. The products are shown in Figure 3.7. The two orthogonal faces of the wedge were connected by a 5mm radius fillet and would be used to form the laminates. The sloped face of the wedge can be placed downwards while the laminate faces up to be compacted by the vacuum bag. The two L-shaped laminates would be laid up separately on two 3D-printed wedges, which would then be pushed together with alignment pins fixing their relative position. The alignment pin holes are highlighted in Figure 3.7. Given that the fillet radius of the wedge was the critical feature of the mould, the wedges were printed from the side up as seen in Figure 3.6, such that the radius could be smoothly defined by the printer nozzle. A drawing of the wedge is attached in Appendix B. As PLA would not be able to sustain the high temperature inside the autoclave, separate forming tools had to be made to maintain the shape of the T-joint inside during the co-curing cycle. These designs are discussed in a later section.

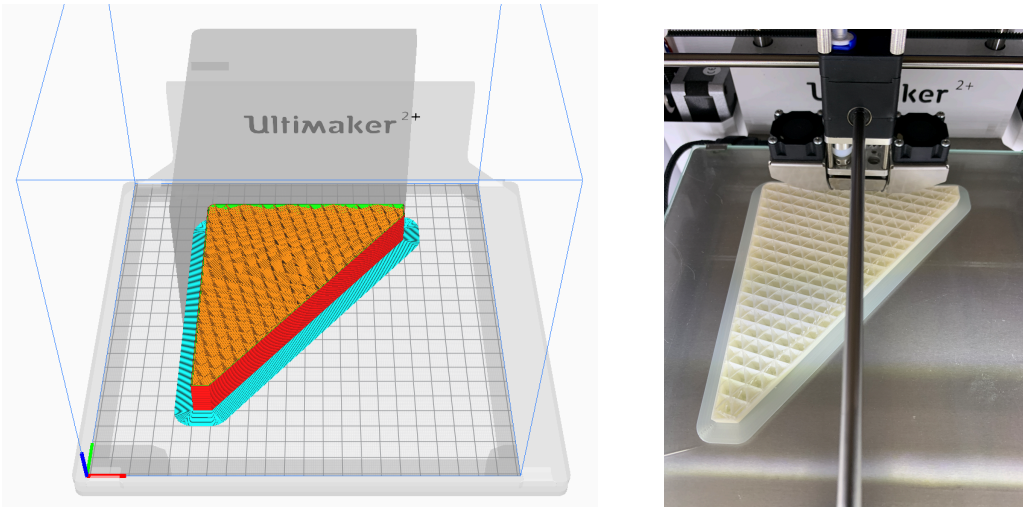

(a) (b)

Figure 3.6: (a) Print preview in the Ultimaker Cura software interface. (b) Print underway in an Ultimaker 3D printer

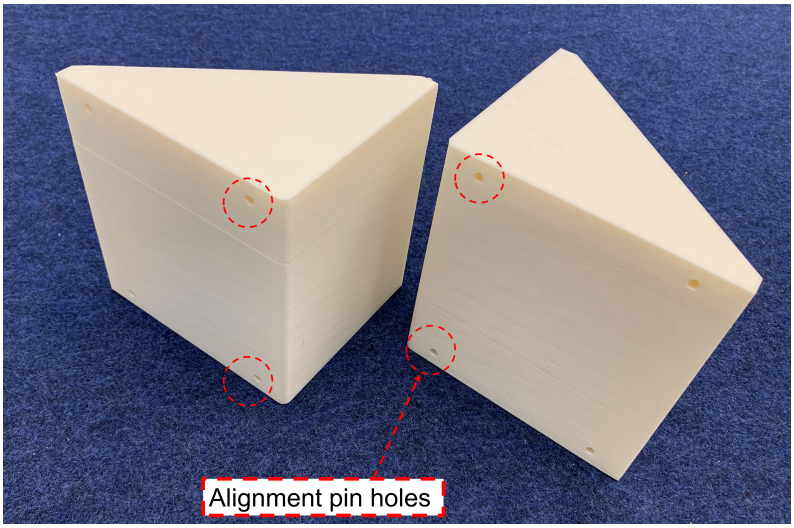

Figure 3.7: 3D printed layup tools

In view of the high material consumption expected from 3D printing the large mould blocks, several small test pieces were first produced to verify the design. The test pieces helped identify the suitable parameters that would produce acceptable surface smoothness, structural rigidity and alignment pin hole geometry. Shown in Figure 3.8 and as drawings in Appendix B, the test pieces were 37mm in length, and featured a 5mm radius fillet and six holes all with slightly different sizes and geometries. The material properties of the printed material were kept constant, and difference in colour simply indicates a different filament roll. After six trials with different printer settings as shown in Figure 3.8a, it was decided that a 0.23mm layer height could yield a satisfactory surface finish in a relatively short printing time. A cubic infill pattern, which consists of internal walls forming cubic cavities, was selected. The pattern was recommended for structures requiring rigidity in all three directions [66], so that the mould block could retain its geometrical accuracy under vacuum bag compression. Using the cubic pattern, sufficient rigidity was achieved by a mere 15% infill, meaning only 15% of the internal space was occupied by printing material. The cubic infill pattern can be seen in the part mid-print in Figure 3.6. The cubic cavities were rotated with respect to the part orientation, causing them to appear like triangles seen from the cross-section.

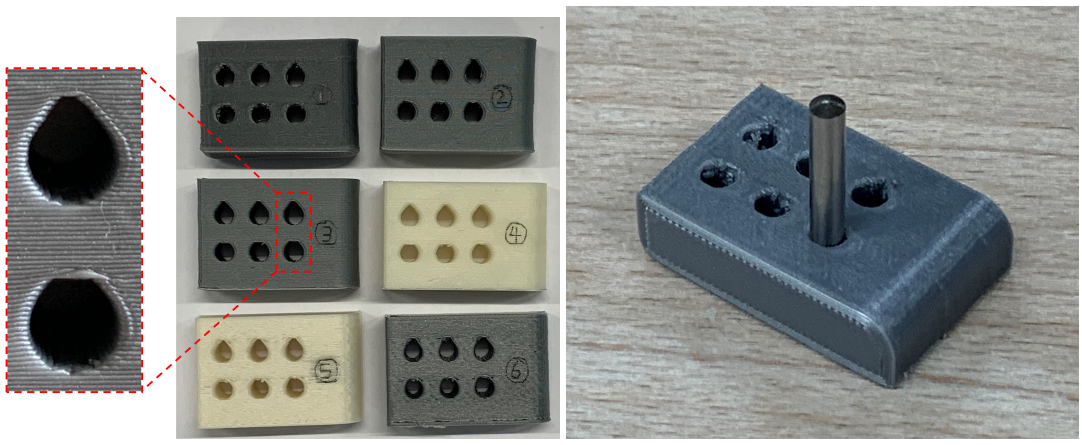

(a) (b)

Figure 3.8: 3D printed test pieces for the determination of print parameters

Finally, the size of the alignment pin hole needed to be verified. Deformation of the plastic during printing meant that 3D printed holes would often end up too tight if the printer nozzle follows the nominal dimension. Holes in the test pieces with incrementally increasing nominal diameters (4mm, 4,1mm and

4.2mm) were tested using a 4mm alignment pin for their respective fit. Figure 3.8b shows a printed part being tested. As mentioned before, the wedges were printed from the side up and the pin holes, therefore, had to be printed horizontally. Holes printed this way typically suffer from distortion in the profile, as the large overhang angle at the top part of the circle tends to cause drooping of the material. A teardrop-shaped hole design [67], where two straight edges with a 45° overhang replace the top section of the circular profile, was therefore also tested. Such a design prevented drooping without the need for support structures. As shown in Figure 3.8a, the bottom row of three holes had a circular profile and various nominal diameters. The top hole in each column had the same nominal diameter as the bottom one, but a teardrop profile. The zoomed-in view shows distortion to the circular profile of the bottom hole, while the teardrop hole on top maintains good clearance for the pin. Results showed that 4.2mm diameter holes with a teardrop profile made the best fit for the 4mm pins used. The pins would not wiggle when inserted, yet could still be easily removed.

3.3.2. In-Autoclave Caul Plates

As the 3D-printed mould blocks could not be used for the high-temperature autoclave cycle, metallic plates were employed to maintain the shape of the T-joint during co-curing. Initially, two large aluminium sheet metal brackets, shown in Figure 3.9a, were applied from outside the vacuum bag (as seen in Figure 3.23f) to maintain the right angle between the web and the flanges. However, the final product (T-joint 1 / NoInterleaf) turned out with a slightly tilted web, since the brackets could not be tightly clamped onto the laminate due to the many layers of soft vacuum bagging materials separating the laminate from the brackets. Moreover, the vacuum bag pushed into the radius bend, squeezing out the epoxy delta fillet and causing fibre waviness.

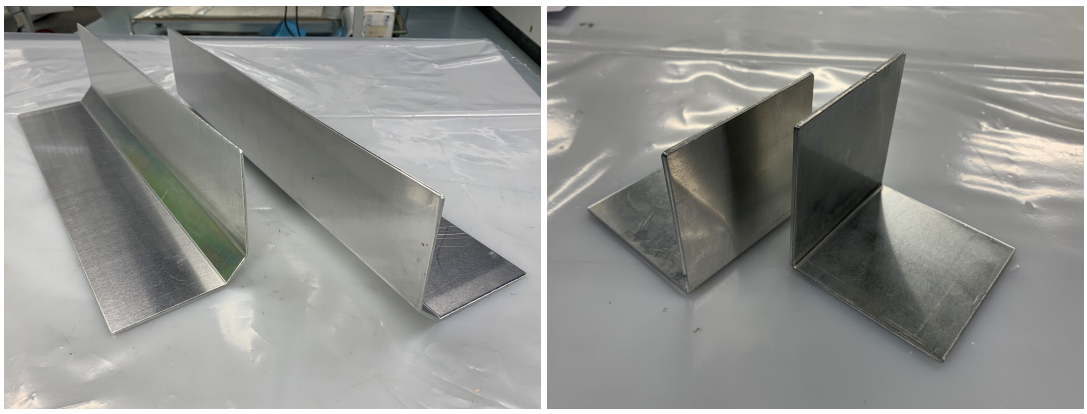

(a) (b)

Figure 3.9: In-autoclave forming tools (a) Aluminium brackets (b) Aluminium caul plates

For the later batches (T-joint 2, 3, 4, and 5), smaller caul plates with a well-defined bend radius were wrapped inside the vacuum bag together with the laminates, only separated by a layer of polytetrafluoroethylene (PTFE) release film. A pair of these plates are shown in Figure 3.9b. The new plates successfully protected the radius bend from overcompaction and resulted in well-defined part geometry. The caul plates applied to T-joint 4 were produced from 2mm aluminium stock. While the quality of the product was satisfactory, slight warpage of the plates was observed after the autoclave cycle. Another pair of 3mm thick caul plates were then produced and used in the last three batches (T-joint 2, 3 and 5) and the issue did not reoccur. While 5mm was the intended bend radius of the caul plates, manufacturing tolerances resulted in slight deviations within acceptable limits.

3.3.3. Delta Fillet Forming Tools

The design of the delta fillet forming tools followed the scheme developed by Trask et al. [7], as seen in Figure 3.10. The fillet material was rolled into a cylinder, and then pushed into the cavity formed by two half moulds. Compared to in-situ forming where the filler material is pressed into the delta void formed by laminates, a separate moulding technique will ensure geometric accuracy and uniform material distribution. The drawing of the mould is included in Appendix B. Additive manufacturing was investigated

as a first option for the moulds. The moulds are depicted during the printing process in Figure 3.11a. As with the layup tools, these moulds were also printed from the side up for accurate fillet geometry. Due to the high aspect ratio of the moulds, large bases were printed around to prevent the parts from toppling over mid-print. Unlike the prepreg layup moulds, the fillet moulds would need to go through an oven cycle for the B-staging of epoxy resins (115°C for API-60 and 80°C for the CNT-modified epoxy paste). In order to quantify the thermal deformation, the abovementioned test pieces were placed in the oven at 60°C for 30 minutes. Dimensions were measured before and after the oven cycle, and significant deformation was noticed. Expansion was measured in the direction through the layers, while shrinkage happened in the other two orthogonal directions. The degree of expansion increased with decreasing layer height, from 1.5% for a layer height of 0.23mm, up to 9.2% for a layer height of 0.06mm. This was due to the high temperature releasing the thermal stress introduced by the printer nozzle during filament extrusion. Trial moulds were printed and put to use, but severe warping would occur, forming gaps between the two half moulds through which the resin would leak.

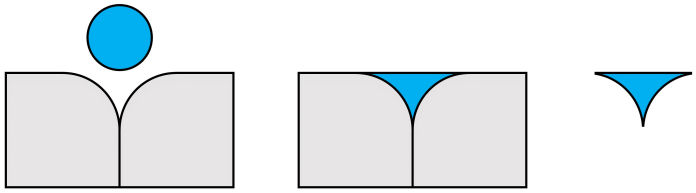

Figure 3.10: Delta fillet forming process

An alternative was then pursued by machining polytetrafluoroethylene (PTFE, or Teflon) blocks down to the exact dimensions. The material was rigid, exhibited minimal thermal deformation and, being inherently non-stick, rendered the application of release agents redundant. Figure 3.11b shows two sets of PTFE moulds. The pair on the right featured an updated design with end blocks to contain the resin flow, but no significant difference in delta fillet quality was observed.

(a) **(b)**

Figure 3.11: Delta fillet forming tools (a) 3D printed moulds (b) PTFE moulds

3.4. Manufacturing Steps

The following sections will describe in detail the steps carried out in the manufacturing stage. While the overall procedure shown in Figure 3.3 was applied to all batches, improvements to the process were continuously implemented to correct any defects observed.

3.4.1. Prepreg Cutting and Layup

The IM7/8552 prepreg roll was first removed from the freezer to defrost overnight. Until it was loaded onto the cutting bed, the roll remained sealed inside multiple layers of plastic bag to prevent moisture from affecting material quality. A Gerber cutting machine was employed to ensure accurate ply dimensions. As shown in Figure 3.12, the prepreg was kept flat on the vacuum suction table, while a numerically controlled circular blade cut out the plies following a predefined path. The plies - rectangles measuring 180mm by 90mm - were densely packed onto the 300mm-wide prepreg roll to minimise material wastage in the manner shown in Figure 3.13. Blue marks the plies used for the skin laminate, while orange marks what would be laid up into two stiffener half laminates. The 0° and 90° plies were produced in one continuous cutting sequence consuming around 2m of prepreg roll, while a second sequence yielded the 45° and -45° plies out of 2.7m of prepreg. A total length of around 4.7m of prepreg roll was used for each batch of samples.

(a) (b)

Figure 3.12: A roll of IM7/8552 prepreg on a Gerber cutting machine

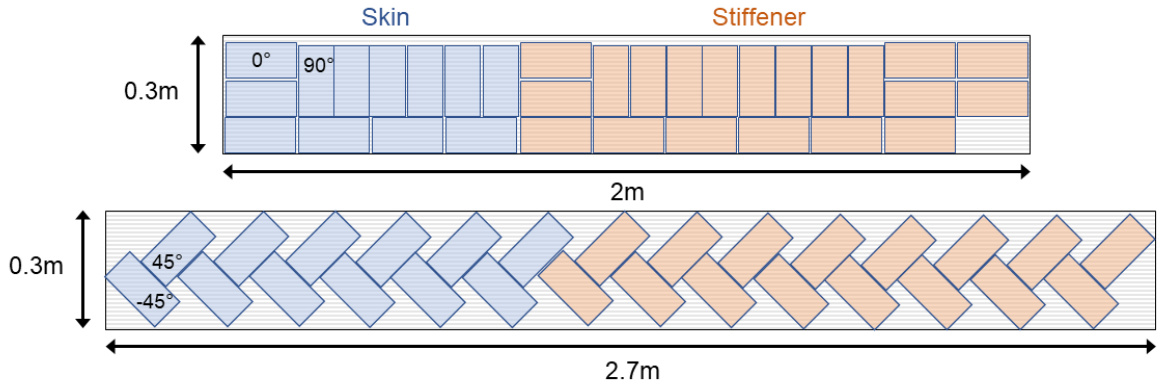

Figure 3.13: Cutting arrangement of plies on the prepreg roll

The plies were then laid up and debulked. The skin laminate was laid up on a flat table surface and placed inside a debulking table after the addition of every ply. The table would then be connected to a vacuum for three minutes at a time to consolidate the laminate and remove air trapped between plies. Figure 3.14 shows the laid-up skin laminate. Backing papers were kept on the top and bottom

to protect surfaces from contamination. The geometry of the L-shaped stiffener half laminates would not fit inside the same debulking table. They were therefore debulked inside a vacuum bag, as shown in Figure 3.15. It can be observed that the wedge design of the moulds allowed them to sit in a stable position while the laminates were evenly compacted by the vacuum bag. Debulking was performed after the addition of every three plies, for 10 minutes at a time. A layer of PTFE release film was taped onto the 3D-printed wedge before the placement of the first ply to separate the wedge surface from the prepreg and ensure easy removal later. After all the plies were laid up, the half laminates and the skin were kept inside the vacuum bag while the interleaves and the delta fillet were being prepared.

Figure 3.14: The skin laminate

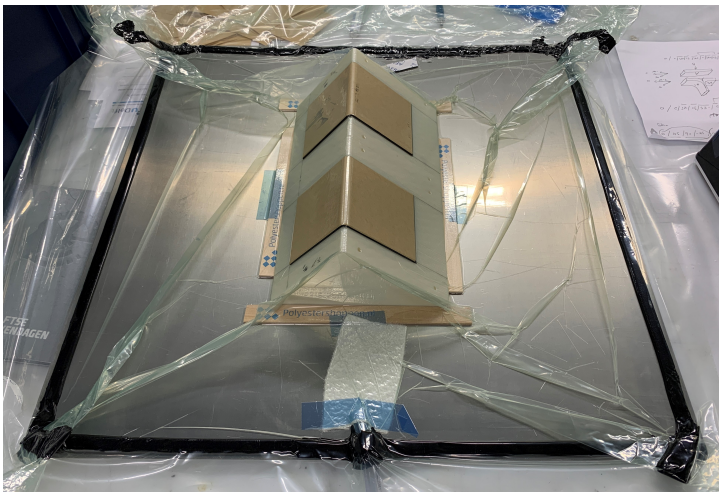

Figure 3.15: Vacuum bag debulking of stiffener half laminates

3.4.2. Manufacturing of Interleaves and Delta Fillets

Two types of interleaves (neat API-60 epoxy and CNT-modified epoxy) and three different delta fillets (neat epoxy, CNT-modified epoxy and UD IM7/8552 prepreg) were produced. Techniques tailored to the unique properties of the materials were developed to ensure consistent quality across all sample batches.

Neat Epoxy Interleaves and Fillets

Manufacturing of the neat API-60 epoxy interleaf (used in T-joint 2 / 200µNeat and T-joint 3 / 200µNeat-FibreFillet) began with preparing the resin according to the mixing ratio (100 part A : 45 part B by weight). A small amount of part A (around 200g) was taken from the bucket with an aluminium mixing stick and held in a beaker. The exact weight was measured and taken as the basis for calculating the weight of part B. Part B powder was added in small batches into the beaker. The mixture thickened up quickly at room temperature. To help with stirring, the beaker was intermittently placed in an oven at 100°C for three minutes at a time. The steps were repeated until all the part B powder was uniformly mixed in. The mixture was then transferred into a speed mixer for further mixing and de-gassing following a cycle developed for API-60 in previous research [19], [38]. Table 3.2 lists the three stages of the cycle. The first 50 seconds allowed the vacuum to drop to 25mBar. Afterwards, the mixer began spinning at 1200rpm for two minutes, while the vacuum further dropped to 10mBar. Finally, the mixing speed increased to 2300 for another minute under a 4mBar vacuum.

Table 3.2: Speed mixer cycle for neat API-60 epoxy

Step	Speed (rpm)	Time (min)	Vacuum (mBar)
A	0	0:50	25
B	1200	2:00	10
C	2300	1:00	4

As soon as the resin was removed from the speed mixer, still warm and fluid from the high-speed mixing, it was poured in one continuous strip onto a piece of Kapton film which had been treated with the Marbocote release agent. The film was placed on top of a 500mm by 200mm glass slab and lined with two 200µ-thick aluminium strips on either side to define the thickness of the interleaf. The size of the resin strip relative to the glass slab is shown in Figure 3.16a. The strip measured roughly 3mm by 15mm. Strict control over the amount of resin was not necessary, as excess would simply flow over the edge of the glass slabs. Another piece of Kapton film and a second glass slab were then placed on top. The weight of the top slab would help distribute the resin and spread it into a layer of constant thickness. The slabs were then wrapped in a PTFE release film and placed in the oven for the B-staging cycle, during which the resin was heated from room temperature to 115°C at a rate of 1°C/min, held at that temperature for 40 minutes, and then cooled down to room temperature at a rate of 2°C/min.

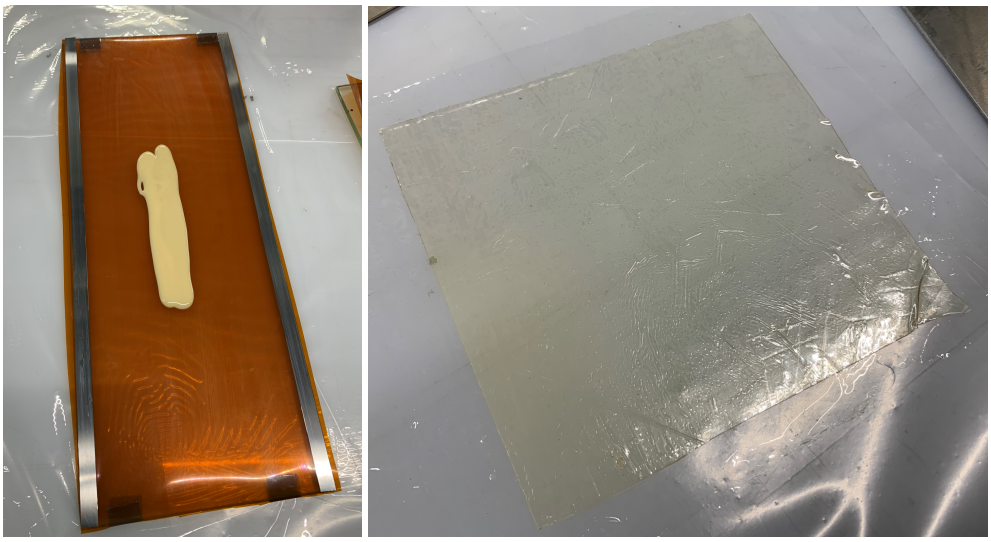

(a) (b)

Figure 3.16: Manufacturing of the neat API-60 epoxy interleaf. (a) Resin poured onto Kapton film (b) Sample of B-staged API-60 interleaf

After removal from the oven, the glass slabs were removed and the interleaf, sandwiched between two layers of Kapton film, was cooled down using ice packs. The quenching step prevented the interleaf from getting tugged by the blade as it was being trimmed to the desired shape. A sample of the interleaf removed from the Kapton films is shown in Figure 3.16b. Occasionally, small voids could be observed in the interleaf and were subsequently trimmed off. When that was not possible, the voids were kept as far from the critical region of the T-joint, i.e. the delta fillet, as possible.

The neat epoxy delta fillet was manufactured using API-60 resin prepared in the same manner just described. Once taken out of the speed mixer, the resin was poured into the cavity formed by the PTFE moulds. A piece of PTFE release film was placed on top of the mould and covered by a flat aluminium plate with a weight on top. The same B-staging oven cycle was applied. The fillet was cooled with ice packs and carefully demoulded. During the manufacturing of each batch, two fillets would be made and the one with better quality would be placed inside the T-joint. In Figure 3.17a, three delta fillets can be seen after the B-staging cycle, still in their respective moulds. The white moulds at the top and bottom of the image are the PTFE moulds, while the 3D printed moulds, which warped and caused resin leakage, are shown in the middle. The cross-section of the delta fillet can be seen in the side view in Figure 3.17b. Figure 3.17c shows the product being integrated into the T-joint.

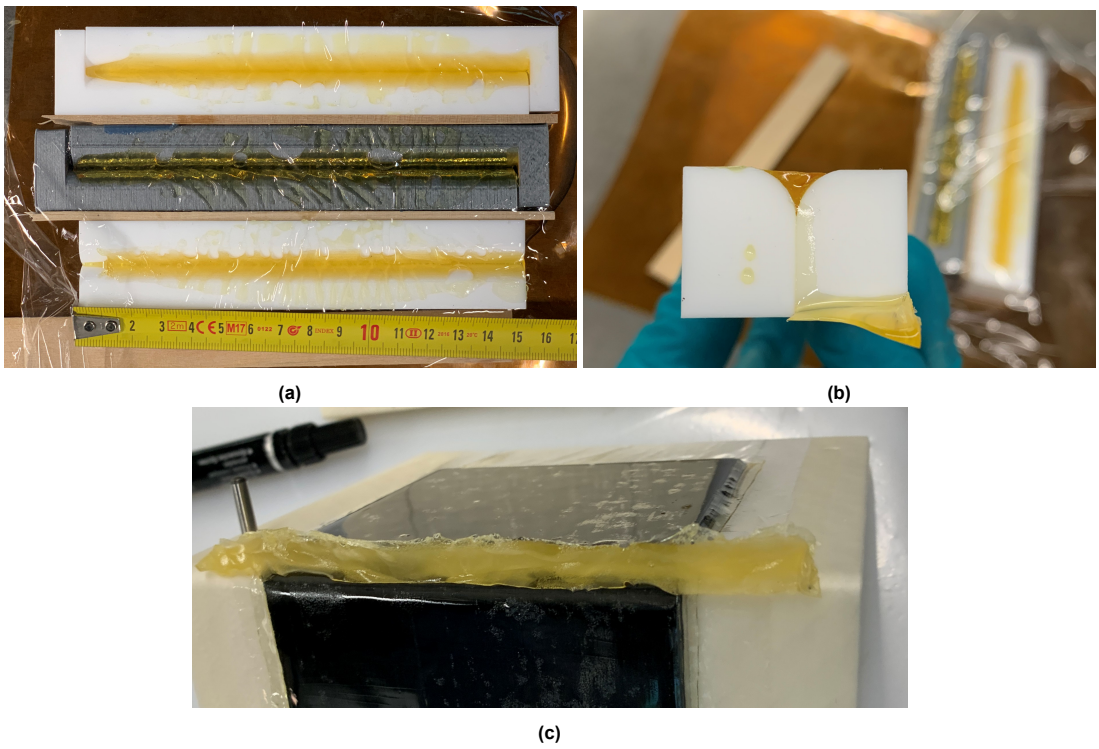

Figure 3.17: (a) Neat API-60 delta fillets after the B-staging oven cycle. (b) Side view of the PTFE moulds (c) Neat API-60 epoxy delta fillets during T-joint integration

CNT-Modified Interleaves and Fillets

The CNT-modified epoxy interleaves were outsourced, but a B-staging cycle was still necessary. Without this step, the epoxy would adhere to the gloss paper and deform as it was peeled off. The interleaves were first cut to dimension before being placed inside the oven. There, they were heated up to 130°C at a rate of 2°C/min. The high temperature was maintained for 55 minutes before cool-down began at a rate of 2°C/min till room temperature. Similarly, the interleaves were then quenched with ice packs. It was important to allow the interleaves to recover from the quenching step before peeling off the gloss paper. If the paper was removed too soon, the still brittle interleaf tended to crack. Figure 3.18 shows the 200µ interleaves containing 1% CNT, with gloss paper removed on one side. On the top left of the image, a small fracture can be noticed.

The CNT delta fillet was formed by first shaping a piece of CNT-modified epoxy paste into a long cylinder. The cylinder measured around 5.4mm in diameter, giving it a cross-section area matching the design. The cylinder was then pressed into the cavity of the PTFE mould and wrapped inside a vacuum bag, as shown in Figure 3.19a. This extra step was necessary because, unlike the API-60 resin, the CNT-modified epoxy had not been de-gassed. The vacuum-bagged mould was then placed inside an oven for the B-staging cycle. During lab trials, the same B-staging cycle applied to the CNT interleaves (130°C for 55 minutes) irreversibly hardened the paste. This was likely due to the higher percentage of CNT, which exhibits high thermal conductivity, accelerating the curing of the resin. In further trials, it was determined that a cure cycle which includes a ramp-up to 80°C at 1°C/min, a plateau for 40 minutes, and a ramp-down at 2°C/min allowed the CNT paste to flow and conform to the shape of the mould without over-curing it. After the cycle, the fillet was also quenched before being demoulded. Figure 3.19b shows the cross-section of the products. The epoxy material conformed well to the shape of the mould cavity, and the demoulding step did not cause noticeable distortion to the shape.

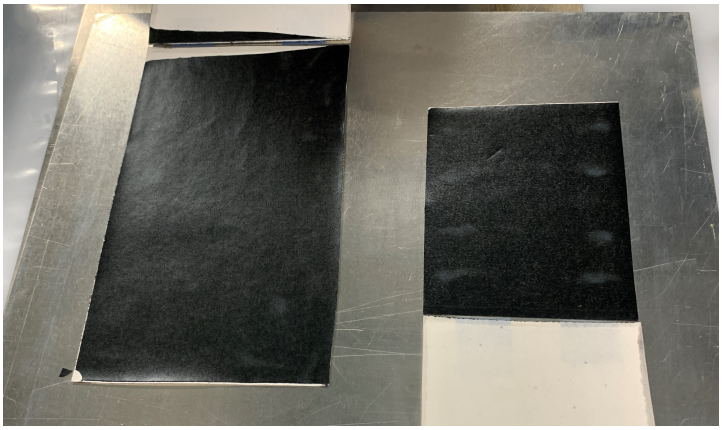

Figure 3.18: 200µ interleaves containing 1% CNT

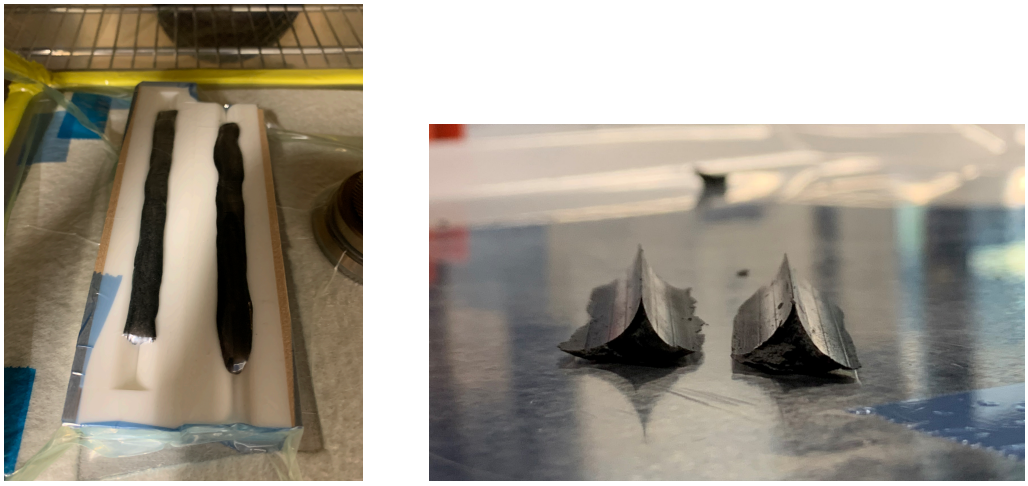

(a) **(b)**

Figure 3.19: CNT-modified epoxy delta fillets

UD Fibre Prepreg Fillet

The UD prepreg delta fillet was manufactured using a similar process but without an oven cycle. An amount of UD IM7/8552 prepreg was rolled into a cylinder with a cross-section area matching that of the delta fillet, as shown in Figure 3.20a. The cylinder was pressed into the mould, with an aluminium plate placed on top for compaction, and then vacuum bagged. The vacuum was maintained overnight (16 hours), which was sufficient to shape the fillets. The result can be seen in Figure 3.20b and the

products are shown in Figure 3.20c. Again, conformity to the mould shape was satisfactory.

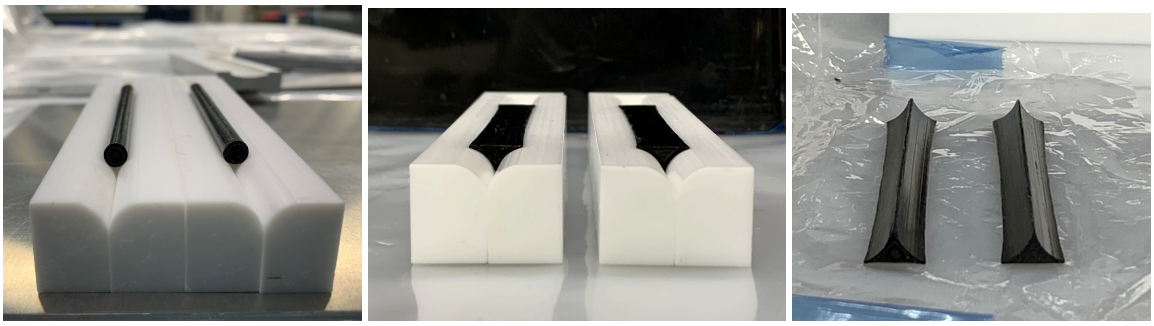

(a) (b) (c)

Figure 3.20: Manufacturing of UD prepreg delta fillets

3.4.3. T-Joint Integration and Co-Curing

Where interleaves were applied (batches 2, 3, 4 and 5), two pieces of interleaves were cut and integrated with the L-shaped laminates. One Kapton film (in the case of the neat epoxy interleaf) or gloss paper (for the CNT interleaf) was removed to expose the interleaf, which was then placed on top of the laminate and compacted. On one side, a large interleaf measuring roughly 100mm by 200mm covered the entire laminate from the web, around the radius bend and down to the flange. A smaller interleaf measuring around 100mm by 100mm covered the other L-shaped laminate, but only from the flange up to the radius bend. The configuration can be seen in the schematic in Figure 3.1, as well as in Figure 3.21. Note that the left laminate is fully covered by the interleaf, while the right laminate is only covered until the bend. This way, only one interleaf layer would be present anywhere.

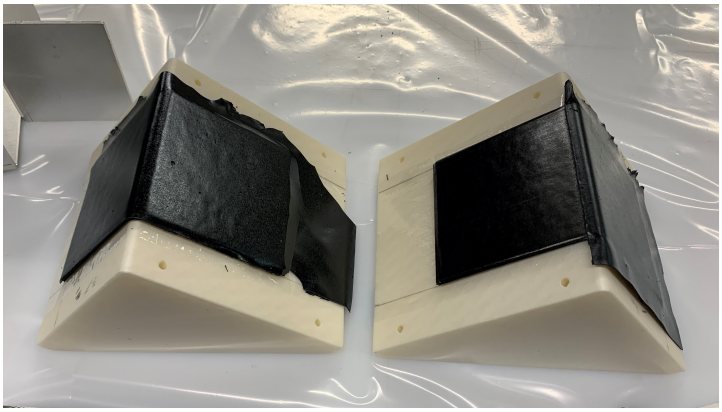

Figure 3.21: CNT interleaves being integrated into T-joint 5 (500µCNT)

The delta fillet would then be placed in contact with the bend of one of the two L-shaped laminates. The two 3D-printed mould wedges were then pushed together to join the L-shaped laminates and form the stringer, using alignment pins as guidance. This step is shown in Figure 3.22. One of the alignment pins used is visible in the gap between the mould wedges. Finally, the skin laminate was placed on top and compacted, thus completing the integration of the T-joint.

The T-joint was then prepared for the autoclave co-curing cycle. The preparation steps are shown in Figure 3.23. The T-joint was placed in an upright position on the mould plate. The mould wedges were then removed, while the PTFE release films previously placed between the mould and the prepreg were left on the laminate. The aluminium caul plates were then placed to take over the role of defining the radius of the joint. The mould plate and the T-joint were then covered under a layer of peel ply and breather fabric to absorb any residual resin. The excess interleaf hanging off the edge of the laminate

would also be absorbed by the peel ply and breather during the cure cycle. A vacuum bag was built up and the standard autoclave cure cycle for IM7/8552 (see Figure 3.4) was applied. In the case of T-joint 1 (NoInterleaf), instead of caul plates, two aluminium brackets (as seen in Figure 3.23f) were attached from outside the vacuum bag. This configuration was not used in later batches due to the substandard quality of the products.

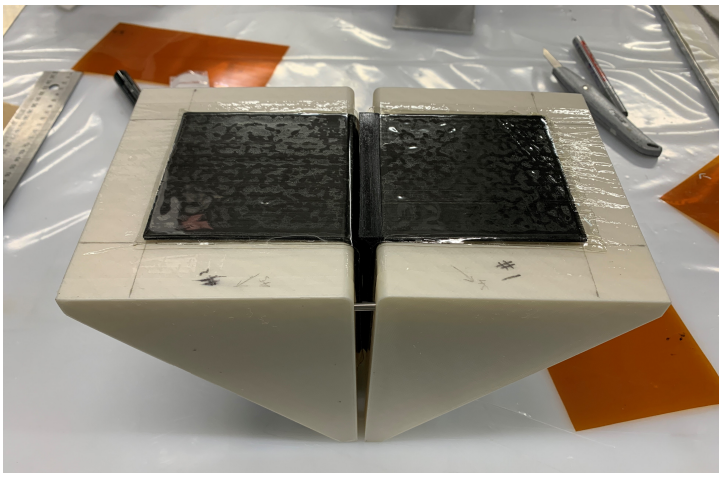

Figure 3.22: Final assembly of T-joint 3 (200µNeat-FibreFillet)

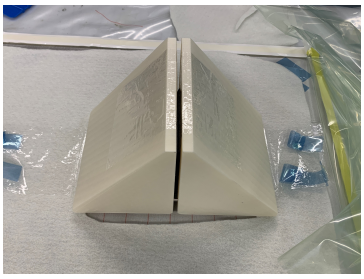

(a) The assembly was inverted and placed on the mould plate

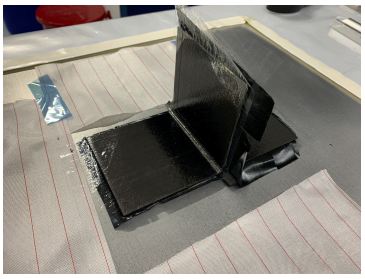

(b) The mould wedges were removed

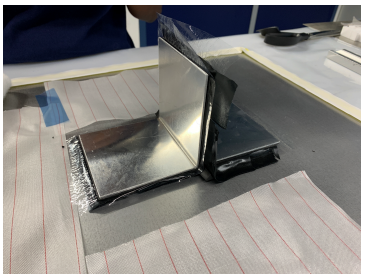

(c) Caul plates were placed onto the T-joint

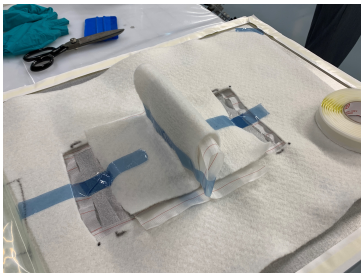

(d) The T-joint was covered by a layer of peel ply and breather fabric, then wrapped inside a vacuum bag

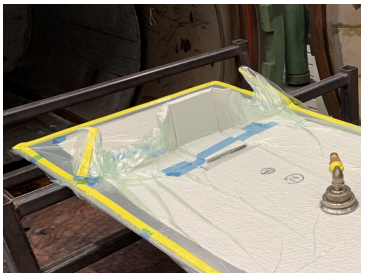

(e) The part was placed inside the autoclave for co-curing

(f) External brackets were used on T-joint 1 (NoInterleaf), but replaced by caul plates in later batches

Figure 3.23: Preparation for co-curing in the autoclave

After the completion of the autoclave cycle, the cured part was removed from the vacuum bag, cleaned, and marked for cutting and trimming. Figure 3.24 shows three cured parts ready the subsequent steps.

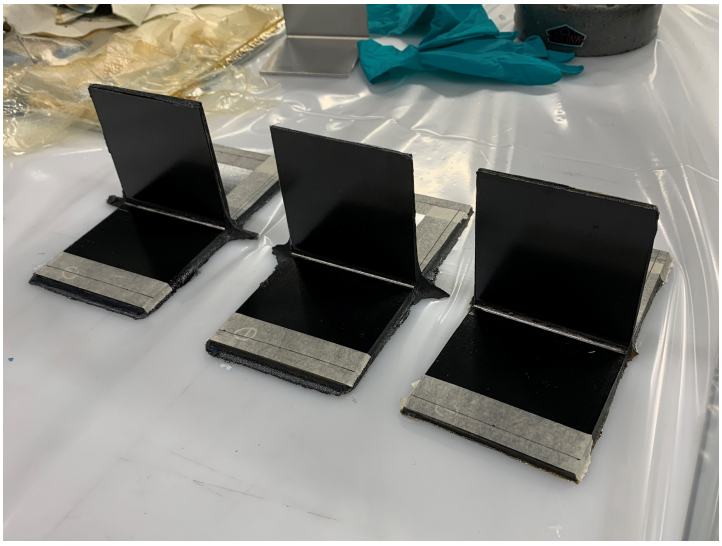

Figure 3.24: Co-cured T-joints

3.4.4. Sample Preparation

After the T-joint was removed from the vacuum bag, the ends of the flanges were first trimmed off using a Proth cutting machine to maintain equal length across all batches. Afterwards, the sides were also trimmed off and each product was sliced into three test samples using a diamond-coated circular saw blade. One of the sample batches is shown in Figure 3.25. On the left and right of the image are the sides that had been trimmed off, while the three T-joints in the middle are samples ready for testing. The cut surfaces were polished by hand using P400-grade sandpapers. The samples were then cleaned, weighed, measured using a calliper, and observed under a Keyence laser confocal microscope to evaluate conformity to the design. Finally, the front and back of the samples were spray-painted white to help make the cracks more visible. A speckle pattern as shown in Figure 3.26 was applied on one side using a matte black aerosol spray can to facilitate Digital Image Correlation (DIC). Accounting for the small area of interest, i.e. the delta fillet region, the pattern was made as fine as possible so that the correlation software could extract more local strain information [68].

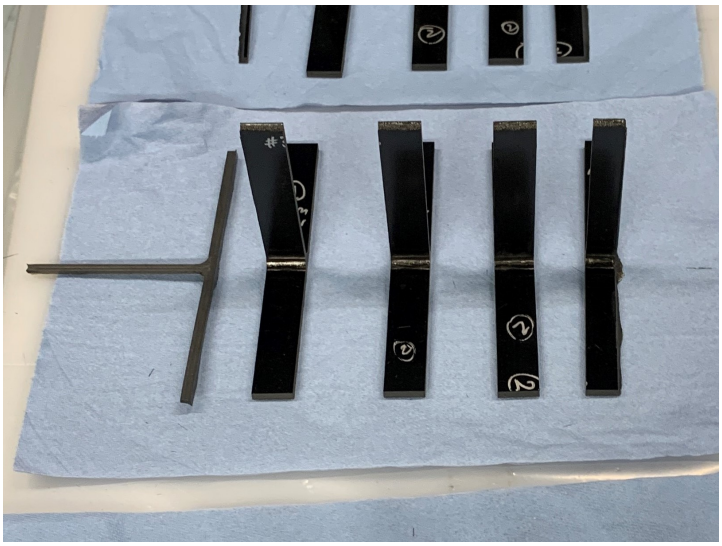

Figure 3.25: T-joint 2 (200µNeat) samples and trimmings

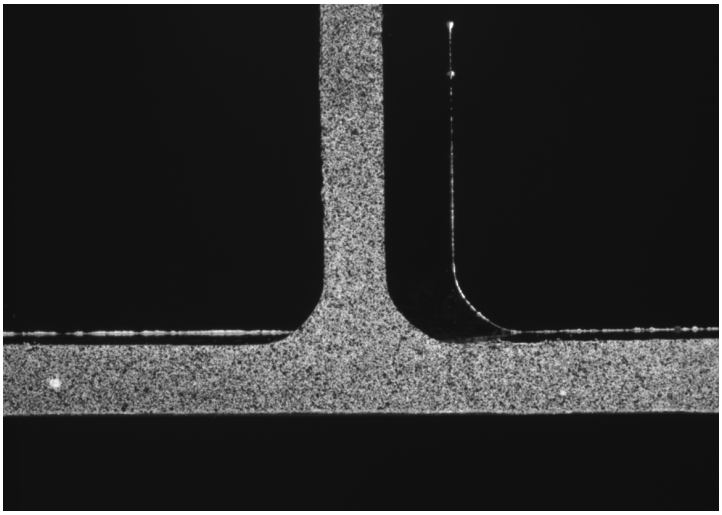

Figure 3.26: DIC speckle pattern

4

Mechanical Testing of Composite T-Joints

A stiffener pull-off load was applied to the T-joint samples to evaluate the mechanical behaviour of the structure. This chapter presents the test equipment used to apply the pull-off load, the data acquisition instruments, and the test procedure.

4.1. Test Equipment

The tests were performed on a Zwick 10kN tensile test machine, with the T-joints loaded via a roller fixture and a hydraulic clamp. The roller fixture setup (shown in close-up in Figure 4.1) was originally designed for a three-point bending test, but could nevertheless be easily repurposed for the T-joint pull-off test. Two free-rolling metallic rollers spaced 120mm apart would apply a simply supported boundary condition to the flanges of the T-joint and restrict its vertical motion. The web of the test sample was gripped by a hydraulic clamp. One side of the clamp was connected to the hydraulic piston, while the other side was static. The static clamping pad was adjusted to ensure that the T-joint was always centred between the rollers after the hydraulics were engaged. During the test, the roller fixture descended with the moving crosshead of the testing machine, while the clamped web remained stationary. The setup is shown in Figure 4.2, together with all the data acquisition apparatus including two Digital Image Correlation (DIC) cameras and one additional camera.

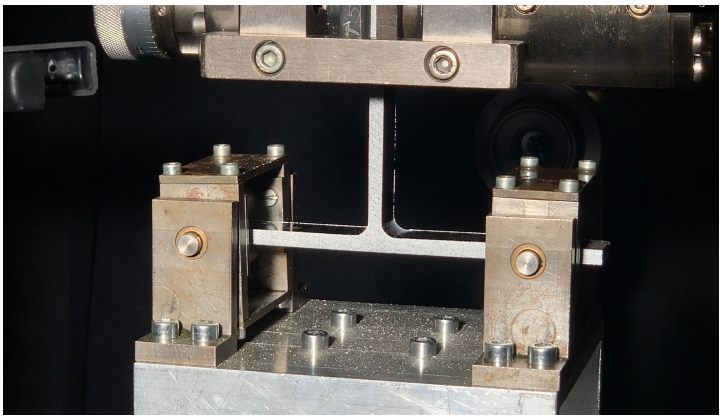

Figure 4.1: Close-up view of the test fixture and the T-joint

Maintaining enough grip on the vertical part of the T-joint posed challenges initially, and trial and error was necessary before the issue was solved with the hydraulic clamp with 150 bar hydraulic pressure. At the beginning, a wedge clamp was mounted onto the test machine as shown in Figure 4.3. The

advantage of the wedge clamp lies in its symmetric design. Since the two clamping jaws are engaged simultaneously from both sides, the T-joint sample would always be centred between the rollers. Unfortunately, the clamping force proved insufficient to prevent slippage. After the wedge clamp was replaced by a hydraulic clamp with 20 bar pressure, slippage was noticed again at high loading. Due to the incident, test data from one of the 200µCNT samples had to be excluded from further analysis. In subsequent tests, the hydraulic pressure was increased from 20 bar to 150 bar. No clamp slippage was observed again after.

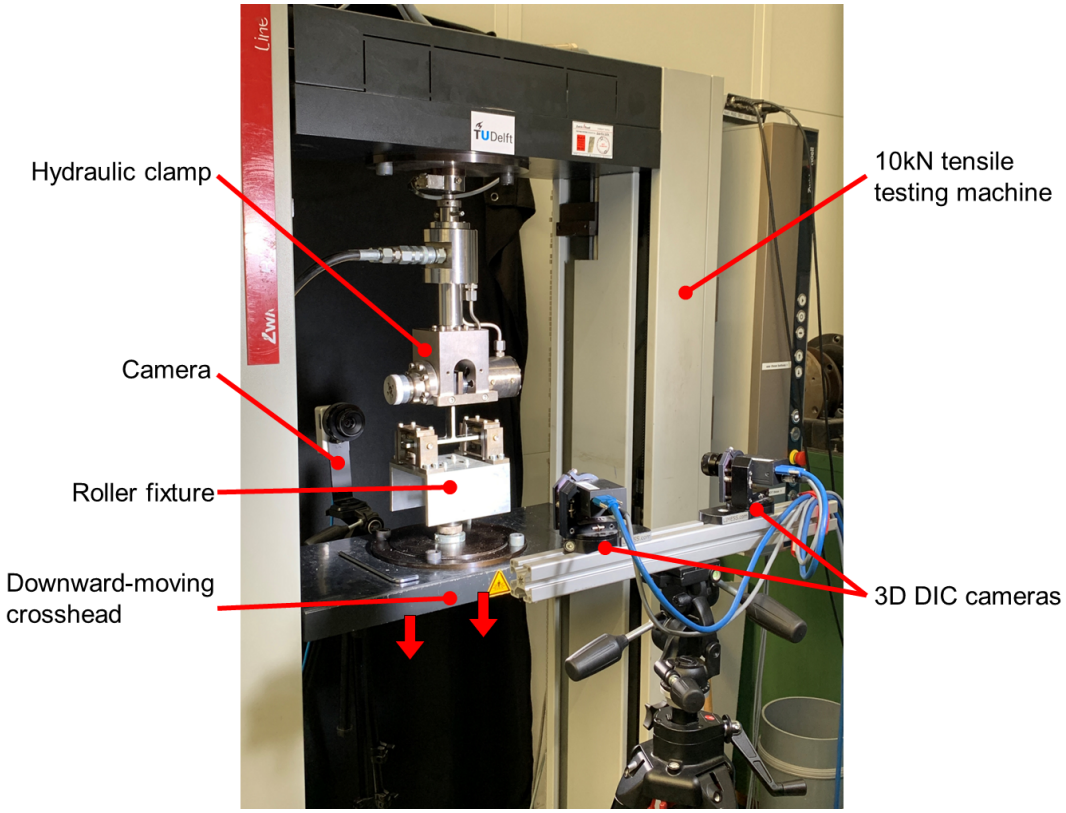

Figure 4.2: Equipment configuration for the T-joint pull-off test

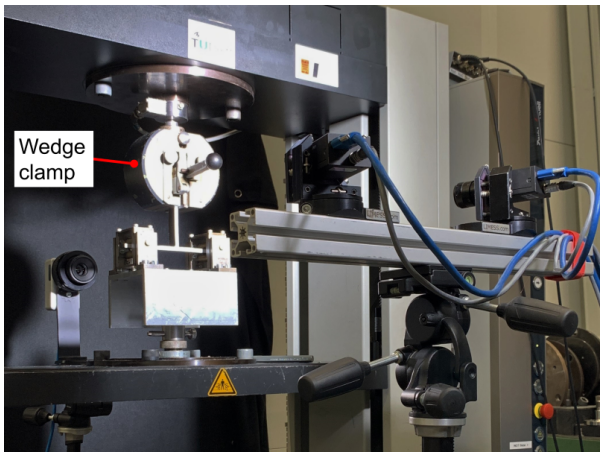

Figure 4.3: T-joint pull-off test setup with a wedge clamp

4.2. Instrumentation

During the test, load-displacement data were continuously acquired. The hydraulic clamp was mounted onto the test machine frame via a load cell with a 10kN range, which produced force readings. Displacement data were acquired from the crosshead. Load and displacement were sampled at an interval of 0.1s.

A 3D DIC system was configured to monitor the strain field during loading. During the last step of sample preparation, a matte black speckle pattern was spray painted onto the side of the samples as can be seen in Figure 3.26. In view of the small size of the sample, the pattern was made to be as fine as possible. Two 9-megapixel cameras with 50mm lenses were installed at a stereo angle of roughly 30° as recommended by the user manual [69], while a floodlight illuminated the DIC-speckled surface. Image capture was powered by the Vic-3D 8 system from Correlated Solutions. Calibration was performed by taking images of a calibration block placed on the focal plane, as shown in Figure 4.4. The calibration block was moved and tilted between images, and a total of 20 images were captured. The images with high errors were then removed from the calibration data set until the Vic-3D 8 software showed the calibration to be acceptable. The location of the calibration block with respect to the front face of the clamp was then marked. Subsequent tests were performed with the T-joint clamped at the same location so that the speckled surface of the specimen would remain in focus.

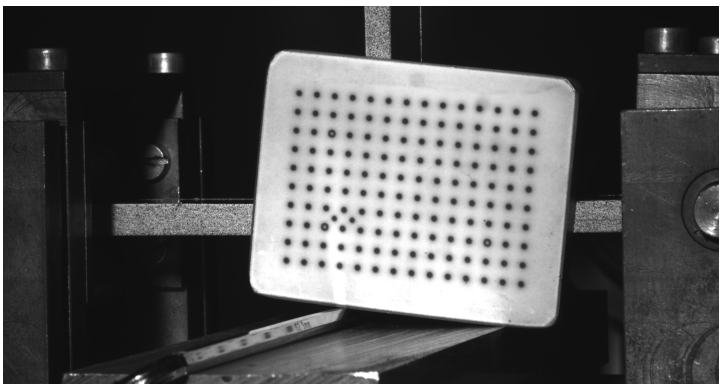

Figure 4.4: Calibration of the DIC system

An additional camera was placed behind the test machine to monitor crack growth from the other side of the specimens. The white-painted surface allowed for a better perception of the crack growth without distortion from the DIC speckle pattern. During post-processing, comparing images taken from both sides helped confirm that the cracks were propagating symmetrically across the width of the sample.

For both the DIC system and the additional camera, images were acquired at a rate of one frame per second. Load-displacement readings from the Zwick test machine were used to stamp all images such that the events captured on the camera could be mapped back onto the load-displacement data.

4.3. Test Procedure

The steps of the test are presented in Figure 4.5. At the beginning of the test, the force reading from the load cell was reset to zero to offset the weight of the hydraulic clamp. The sample was then placed between the rollers and the web was clamped at 60mm above the top surface of the flange. The clamp was adjusted to align the web with the centre line of the roller fixture. The distance between the speckled surface of the sample and the front of the clamp was measured and adjusted according to the marked value so that all cameras would be in focus. The clamp hydraulic was then engaged at a pressure of 150 bar. The crosshead was slightly adjusted to detach the T-joint from the rollers so that the structure was completely relaxed.

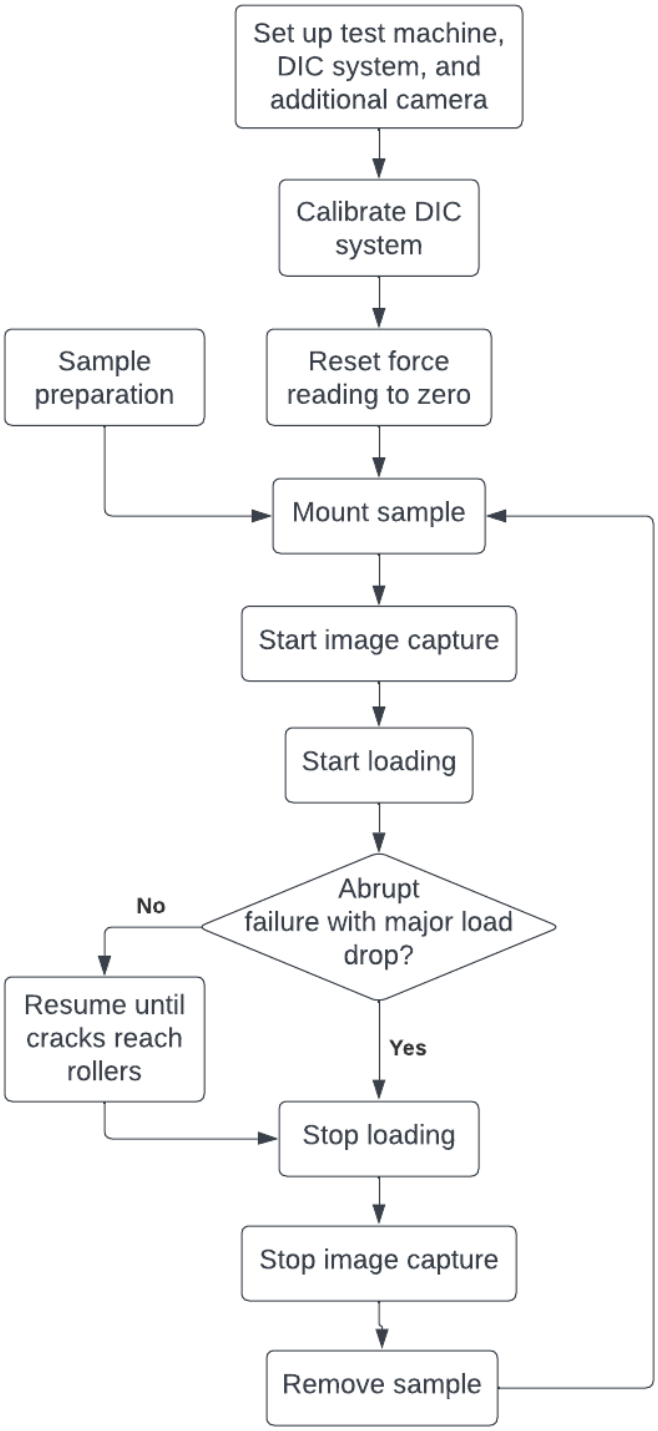

Figure 4.5: Test procedure flow chart

A displacement-controlled loading at a rate of 1mm per minute was applied. Due to manufacturing imperfections, one flange would come in contact with the roller first as the crosshead moved down, while the other flange quickly followed. A deflection point in the load-displacement curve marking a stiffness change would be observed, signalling full contact between the rollers and the flanges. A crosshead displacement limit (10mm for T-joint 1, 20mm for the later batches) was set for safety but was not reached. Instead, the tests were stopped manually after a major load drop accompanying the abrupt separation of the stiffener from the skin. In the absence of such an event, the tests were stopped when the cracks reached the roller supports. Images were captured throughout the duration of the test at a rate of one

frame per second by the DIC system and the additional camera.

After the loading was stopped, the crosshead moved back up to remove the load until it was under 10N. The hydraulic clamp could then be disengaged and the sample was removed from the testing machine. The procedure was repeated until all samples were tested.

5

Results and Discussion

This chapter presents the experimental results and discusses their implications. The sample measurements are first presented to help assess the quality of the samples. Data acquired during the stiffener pull-off tests are reported afterwards. Results from two sample groups with severe defects are discussed to highlight the influence of manufacturing quality. Finally, the rest of the samples are compared to reveal the effect of CNT interleaves.

5.1. Sample Measurements

A total of five specimen batches, each containing three samples, were manufactured and the key dimensions were measured. These include the weight, length, width, radii of the outer bend and the delta fillet, cross-section area of the fillet, and thickness of interleaves where applicable. The length and width were taken using a digital calliper and only one measurement was taken per sample. The thicknesses and radii were measured from both sides of each sample under a Keyence laser scanning confocal microscope with a 2.5X magnification lens. Table 5.1 presents the average values across the three samples from each batch, while the full measurement data are included in Appendix A. Letters A and B are assigned to the two flanges of each sample to denote dimensions defined by the same caul plate in the autoclave. The standard deviation is also reported and, where applicable, the deviation from design value as a percentage is included as an indicator for manufacturing quality. One image from each specimen batch is presented in Figure 5.1. Visual inspection of the microscopy images suggests good consistency among samples from the same batch. This is further supported by generally low standard deviation values.

After inspection of the sample measurement results, it was decided that batches 3 (200µNeat-FibreFillet), 4 (200µCNT) and 5 (500µCNT) were of satisfactory quality and were expected to yield meaningful conclusions regarding the effect of CNT interleaves, while batches 1 and 2 contained severe defects. Nevertheless, the quality of all sample groups is discussed below as a reference for future manufacturing efforts. The discussion follows the chronological order of manufacturing, to highlight the incremental improvements in production techniques.

T-joint 1 (NoInterleaf) was intended as a trial batch serving as the basis for further improvements. Consequently, the quality of the samples was deemed less satisfactory. Without caul plates, the laminates suffered from uneven compaction and fibre waviness was apparent in the surface plies (see Figure 5.1a). The vacuum bag pushed into the radius bend, creating a much smaller bend radius compared to the design. Severe fibre crimping and asymmetry could be observed in the radius bend area. A resin pocket could be observed on the outside of the crimp. The resin in the delta fillet was largely squeezed out during autoclave compaction. The web was noticeably tilted, as the brackets outside the vacuum bag were not sufficient to keep it vertical.

Table 5.1: Sample measurements. Data are averaged across all three samples in each batch. Standard deviation is included in square brackets. Full data are included in Appendix A

Group	NoInterleaf (T-joint 1)	200µNeat (T-joint 2)	200µNeat-FibreFillet (T-joint 3)	200µCNT (T-joint 4)	500µCNT (T-joint 5)
Interleaf	None	200µ neat API-60	200µ neat API-60	200µ 1% CNT epoxy	500µ 1% CNT epoxy
Delta fillet	Neat API-60	Neat API-60	UD IM7/8552 prepreg	CNT epoxy	CNT epoxy
Caul plates	-	3mm plates	3mm plates	2mm plates	3mm plates
Weight (g) [SD]	-	39.50 [0.52]	41.73 [0.31]	40.80 [0.61]	41.77 [0.40]
Length (mm) [SD]	164.85 [0.20]	165.00 [0.20]	164.03 [0.06]	165.00 [0.00]	165.50 [0.10]
[%deviation from design]	3.03%	3.13%	2.52%	3.13%	2.81%
Width (mm) [SD]	19.96 [0.04]	19.94 [0.05]	20.39 [0.03]	19.93 [0.07]	19.89 [0.09]
[%deviation from design]	-0.20%	-0.32%	1.95%	-0.35%	-0.57%
Flange + skin thickness (mm) [SD]	5.43 [0.14]	5.19 [0.02]	5.47 [0.05]	5.32 [0.06]	5.71 [0.05]
Web thickness (mm) [SD]	4.53 [0.13]	4.48 [0.07]	4.82 [0.05]	5.09 [0.04]	5.03 [0.03]
Outer bend radius					
- flange A side (mm) [SD]	1.06 [0.14]	6.00 [0.25]	6.08 [0.20]	4.53 [0.22]	6.14 [0.28]
[%deviation from design]	-78.82%	19.93%	21.67%	-9.50%	22.72%
- flange B side (mm) [SD]	0.46 [0.13]	6.13 [0.39]	6.12 [0.32]	4.42 [0.09]	6.36 [0.10]
[%deviation from design]	-90.83%	22.69%	22.35%	-11.53%	27.26%
Delta fillet radius					
- flange A side (mm) [SD]	0.43 [0.04]	-	8.08 [0.45]	7.14 [0.89]	9.00 [0.73]
[%deviation from design]	-94.18%	-	9.95%	-2.93%	22.41%
- flange B side (mm) [SD]	0.53 [0.08]	-	8.65 [0.59]	6.82 [0.60]	9.33 [1.32]
[%deviation from design]	-92.74%	-	17.63%	-7.28%	26.90%
Delta fillet area (mm^2) [SD]	0.07 [0.01]	-	26.20 [0.31]	19.23 [2.79]	31.78 [0.50]
[%deviation from design]	-99.71%	-	12.68%	-17.29%	36.68%
Post-cure interleaf thickness					
- skin-flange (µ) [SD]	-	-	-	53.60 [15.34]	114.54 [12.75]
[%deviation from design]	-	-	-	-73.20%	-77.09%
- web (µ) [SD]	-	-	-	137.09 [41.71]	101.44 [29.00]
[%deviation from design]	-	-	-	-31.46%	-79.71%

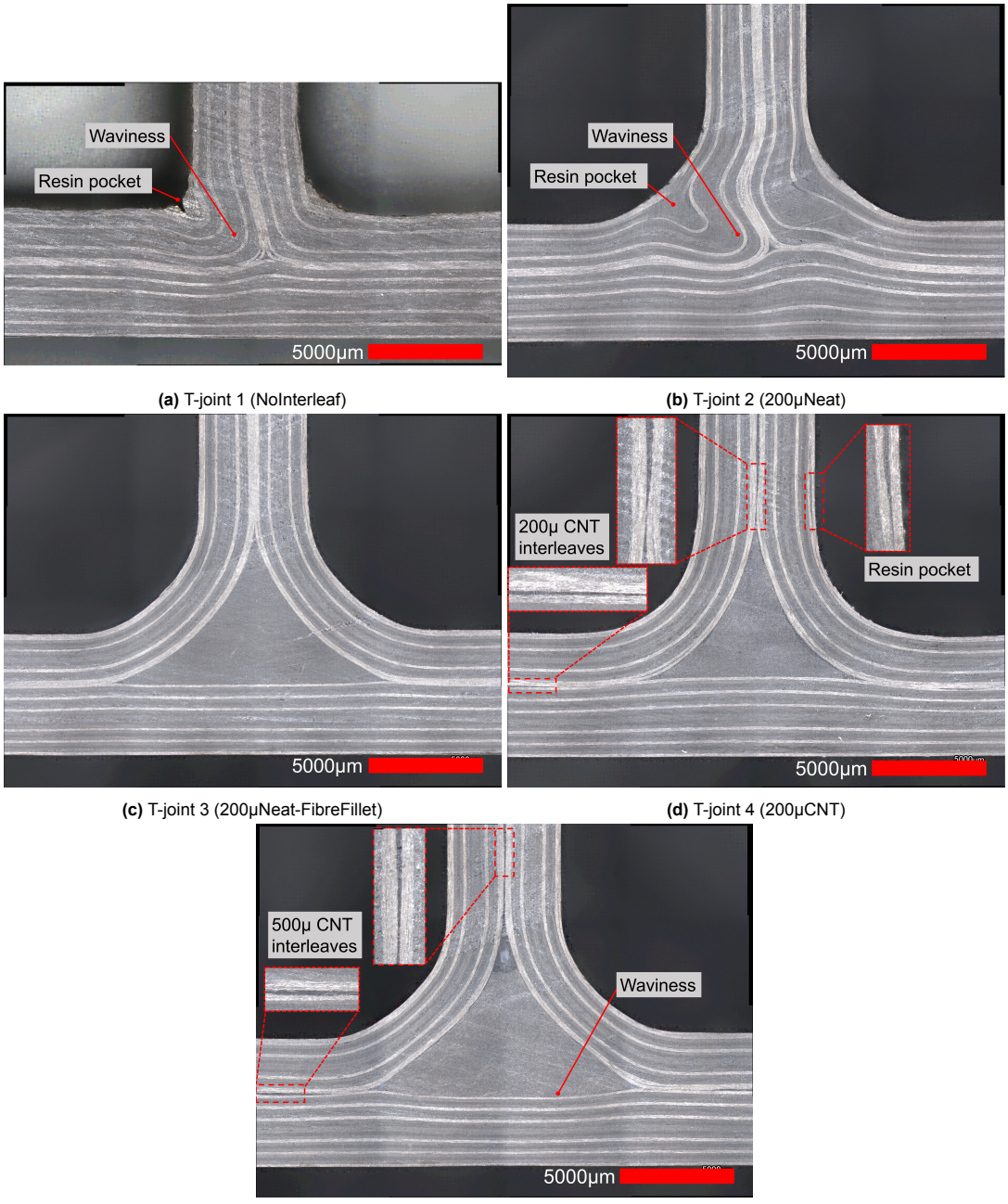

(a) T-joint 1 (NoInterleaf)

(b) T-joint 2 (200µNeat)

(c) T-joint 3 (200µNeat-FibreFillet)

(d) T-joint 4 (200µCNT)

(e) T-joint 5 (500µCNT)

Figure 5.1: Microscopic images of T-joint samples

Lessons from batch 1 were implemented in the manufacturing of T-joint 4 (200µCNT) to yield more satisfactory results. A pair of 2mm-thick caul plates were introduced inside the vacuum bag to define the radius bend and ensure even compaction. Under the microscope, the plies could be observed to smoothly follow the curvature of the bend. The cross-section area of the delta fillet was around 17% below the design values but was nevertheless deemed acceptable. It appears that heavier compaction took place at the corners, causing a local thinning of the interleaf layer. This can be observed in Figure 5.1d: the zoomed-in images show the interleaves tapering towards the delta fillet. The interleaf thickness was therefore measured away from the delta fillet, to accurately reflect the overall level of compaction. The CNT interleaves suffered a loss in thickness - the 200µ interleaves reduced to around 54µ (73.20% loss) in the flange-skin interface and 137µ (31.46% loss) in the web, an expected result of compaction in combination with squeeze-out. The thickness of the interleaf in the web exhibited a rather high standard deviation across samples, suggesting non-uniform compaction. Figure 5.1d also

highlights a resin pocket between the two external 0° plies. As a matter of fact, the caul plates became unsuitable for reuse when warpage was noticed after removal from the vacuum bag. A new pair of thicker caul plates were then prepared for later batches.

The three final batches were produced using the same manufacturing equipment and steps. As a result, the geometry was very consistent across all nine samples. The outer radius was more than 20% higher than designed due to the different manufacturing tolerances of the new caul plates. Unfortunately, the same delta fillet squeeze-out seen in T-joint 1 reoccurred in T-joint 2 (200µNeat). The defects are highlighted in Figure 5.1b. While the outer geometry conformed to the design, the volume that should have been occupied by the neat API-60 resin was filled instead by wavy fibre within the fillet region. Large resin pockets could be observed in between plies. It is worth noting, however, that fibre waviness was limited to the inner plies. Unlike the case of T-joint 1, the outer contour plies followed their predefined paths owing to the inclusion of caul plates.

The other CNT-modified sample group, T-joint 5 (500µCNT), also demonstrated satisfactory manufacturing quality. It is however not without deviations from the design. The area of the delta fillet was noticeably larger than the design. As a result, slight fibre waviness could be observed in the skin laminate. This is highlighted in Figure 5.1e. A reduction in the interleaf thickness (77.09% in skin-flange, 79.71% in the web) was again observed, but the non-uniform compaction seen in T-joint 4 (200µCNT) had been alleviated by the thicker caul plates.

In both T-joint 4 (200µCNT) and 5 (500µCNT), the thickness of the skin-flange interleaf reduced by roughly the same proportion (73.20% and 77.09%). The same could not be said about the web interleaf which, due to uneven compaction, was thicker in the 200µCNT T-joint than in 500µCNT. Nevertheless, the results to be presented in the following section will show that damage before final failure was restricted to the skin-flange interleaves. Therefore, the 500µCNT group remained eligible to be treated as samples with thicker CNT interleaves.

T-joint 3 (200µNeat-FibreFillet) displayed the best conformity to design in terms of the radius and the area of the delta fillet. The cross-section area of the delta fillet deviated from the design by only 12.68%, the lowest among all samples. No noticeable defects could be observed in Figure 5.1c. This was to be expected, as the adopted manufacturing techniques were able to control the dimensions of a UD fibre fillet with the most precision. The neat API-60 resin interleaves were difficult to observe under 2.5X magnification, likely due to squeeze-out as well as their similar visual properties to neighbouring plies and were therefore not measured.

While all batches were tested, only groups 3, 4 and 5 were of consistent enough quality to offer insights into the effect of CNT interleaves on the mechanical behaviour of T-joints. Nevertheless, the data from batches 1 and 2 would serve as evidence to prove the effect of manufacturing quality on the performance of the structure.

5.2. Experimental Results and Discussion

Results from the T-joint pull-off tests will be presented in two separate sections, following a brief account of the data post-processing scheme. In the first section, data from the two groups with manufacturing defects (NoInterleaf and 200µNeat) will be presented, and the effect of manufacturing techniques will be discussed. In the next section, the sample groups 200µNeat-FibreFillet, 200µCNT and 500µCNT will be compared. 200µNeat-FibreFillet serves here as the control group, against which the CNT-modified samples will be judged.

5.2.1. Data Post-Processing Scheme

The same data post-processing scheme was applied to all specimens. Due to slight imperfections in the samples and the fixtures, one T-joint flange usually touched the roller before the other. When raw data were inspected, a deflection point in the load-displacement curve marking a sudden change in stiffness could be observed at the beginning of the test. In order to facilitate comparison across samples, the curves were trimmed such that displacement was set to zero at the instant where both flanges

came in contact with the rollers.

The stiffness of the samples was measured by fitting a linear function onto the load-displacement curve from 0.5mm displacement to 1mm or until the first load drop, whichever came first. The strain energy till failure was calculated by integrating from the beginning of the test until the final failure, i.e. separation of the stiffener from the skin, giving the area under the curve. The peak loads of 200µNeat-FibreFillet, 200µCNT and 500µCNT samples mostly coincided with the final failure of the joint. The indicator was therefore useful for quantifying the amount of energy that could be absorbed by the structure before failure. For the two sample groups with defects where the peak load did not indicate final failure, the integration was performed until the peak load was reached for comparability.

Data from all but one test were deemed admissible after post-test inspection of the samples indicated good consistency across all batches. The one exception was the test of sample 200µCNT_3 during which clamp slippage occurred. The test data from this specimen was therefore omitted from further analysis. Comparison between images captured from both sides of the sample showed that the cracks propagated in a symmetrical manner across the width of the samples. As the sample dimensions lie in close proximity across all batches, no data normalisation was deemed necessary.

The maximum load (F_{max}), crosshead displacement (dL) at F_{max}, stiffness, and strain energy of each sample are presented in Table 5.2. The mean and standard deviation values of each sample group are also calculated. In the subsequent discussion, the sample with the highest F_{max} value is chosen as the representative sample for visualising strain fields and damage progression.

5.2.2. Influence of Manufacturing Quality

Load-displacement curves from NoInterleaf and 200µNeat specimens as well as the extracted data are presented in Table 5.2 and Figure 5.2. The performance indicators suggest significantly inferior performance compared to the three other groups. Between the two groups, 200µNeat shows marginally better performance in terms of the peak load and the strain energy absorbed, but it was difficult to determine whether the gains were a result of the neat epoxy interleaves or the better defined outer geometry. The curves show a rather high level of consistency across samples within the same batches. In all tests of these two batches, separation of the stiffener from the skin took place well before the displacement reached 3mm, but as the event was not accompanied by a major load drop, the tests were continued until the cracks propagated to reach the rollers.

Images captured by the DIC system were used to extract displacement and strain data. The major strain fields are plotted in Figure 5.7. Since the results were consistent within groups, only one sample was presented to represent each group. The black dashes on the contour plots represent the direction of major strain e1. Strain fields are plotted at instances when the load is around 250N, 500N, and immediately before the appearance of the first crack. Since DIC images were captured at a relatively low rate, the instances with forces closest in value are presented. The exact load and displacement values are included in the plots. Due to the very different manufacturing quality and geometry of NoInterleaf and 200µNeat specimens, the strain fields could not be plotted on the same scales without compromising readability. Therefore, all contours are plotted using their own scales and the same colour across different plots does not indicate the same strain values.

The strain field plots are only presented for the linear regime, up till the moment of the first failure. This was because the DIC software could not process the speckle patterns once they were distorted by the cracks. In the plots presented in Figure 5.3, asymmetric strain fields can be observed. Comparing the contour plots to the micrographs in Figure 5.1a and Figure 5.1b reveals that the peak strain values correspond to resin pockets and wavy fibre straightening up under the pull-off load. Note that, since Figure 5.3 and Figure 5.1 depict opposite surfaces of the same T-joint samples, the comparison should be made by mirroring one of the two images. Strain in the horizontal direction constitutes the main component of major strains.

Table 5.2: Pull-off test result data

Sample	F_{max} (N)	Average [SD]	dL at F_{max} (mm)	Average [SD]	Initial stiffness (N/mm)	Average [SD]	Strain energy to failure (mJ)	Average [SD]
NoInterleaf_1	613.92	568.93 [41.07]	2.84	2.29 [0.49]	305.08	351.28 [40.87]	1034.16	779.77 [229.36]
NoInterleaf_2	533.42		1.89		382.71		588.76	
NoInterleaf_3	559.46		2.15		366.05		716.40	
200µNeat_1	838.00	772.45 [83.06]	2.87	2.81 [0.20]	365.04	341.42 [36.05]	1384.11	1229.88 [134.12]
200µNeat_2	800.31		2.59		359.31		1140.57	
200µNeat_3	679.04		2.98		299.93		1164.97	
200µNeat-FibreFillet_1	1218.65	1195.15 [40.7]	3.70	3.45 [0.36]	420.72	426.27 [5.94]	2550.74	2304.43 [382.48]
200µNeat-FibreFillet_2	1148.16		3.04		425.56		1863.79	
200µNeat-FibreFillet_3	1218.64		3.61		432.53		2498.75	
200µCNT_1	1215.74	1188.35 [38.74]	6.73	7.18 [0.65]	369.85	357.36 [17.66]	5349.12	5673.73 [459.07]
200µCNT_2	1160.96		7.64		344.87		5998.34	
500µCNT_1	1229.33	1132.42 [125.46]	7.09	5.67 [1.33]	458.51	442.17 [24.52]	5865.11	4429.17 [1415.89]
500µCNT_2	1177.21		5.47		454.03		4388.18	
500µCNT_3	990.71		4.46		413.97		3034.23	

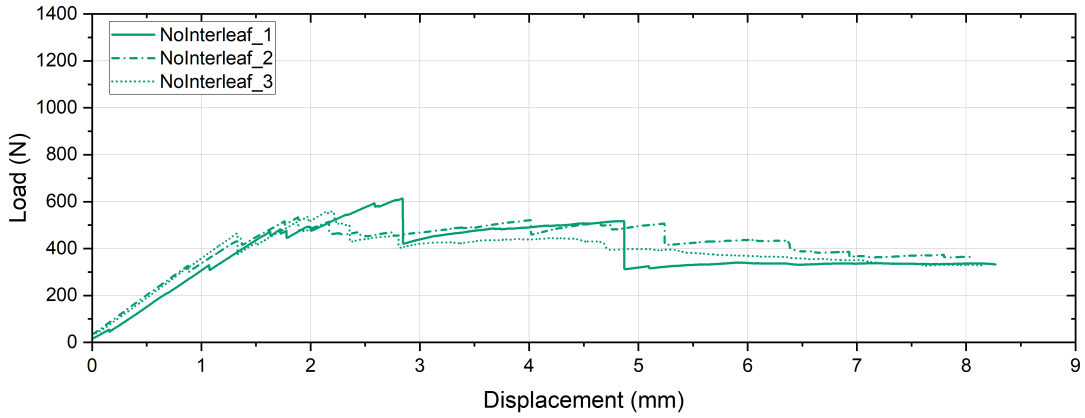

(a) NoInterleaf

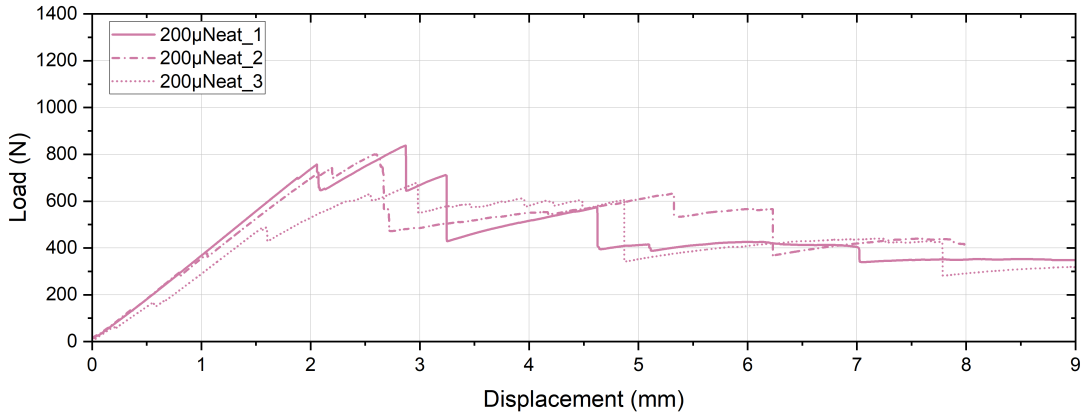

(b) 200µNeat

Figure 5.2: Load-displacement curves from groups NoInterleaf and 200µNeat

After the initial linear regime, the NoInterleaf and 200µNeat T-joint samples would attain their peak loads very briefly after the onset of cracks. The load drop after the peak load usually corresponded to the straightening up of the crimping fibres. Following the slight relaxing of the fibre crimps, the cracks migrated to the interface between the L-shaped half laminates and the skin and steady propagation could be observed, but the load remained low and relatively constant. The cracks would continue to expand steadily until they reached the fixtures on either end of the sample. The T-joints remained rather compliant throughout the tests and no sudden failure occurred. Figure 5.4 shows the fully developed crack patterns towards the end of tests. It can be observed that the three constituent laminates were fully separated at the intersection.

Despite not contributing to the primary conclusion of the research, results from the NoInterleaf and 200µNeat samples still revealed lessons for the design and manufacturing of T-joints. First of all, the critical role of the delta fillet was confirmed. Without the filler ensuring a smooth bend, load transfer in the laminate was severely disrupted, causing the joint to fail prematurely at significantly lower loads.

In addition, the subpar quality of the samples points to the need for further research into the B-staging of neat epoxy. After the complete squeeze-out of the neat API-60 delta fillet in T-joint 1 (NoInterleaf), it was suspected that overcompaction due to the lack of caul plates was the cause. Yet, despite caul plates ensuring more even compaction for T-joint 2 (200µNeat), the fillet was once again pushed out. The B-staging cycle adopted was likely unable to form enough bonds to allow a mass of neat epoxy as large as the filler to maintain its shape under the autoclave pressure. It may be worth investigating whether a lower autoclave curing pressure contributes to retaining the geometry of the B-staged delta fillet. However, deviation from the standard cure cycle can also adversely affect prepreg quality.

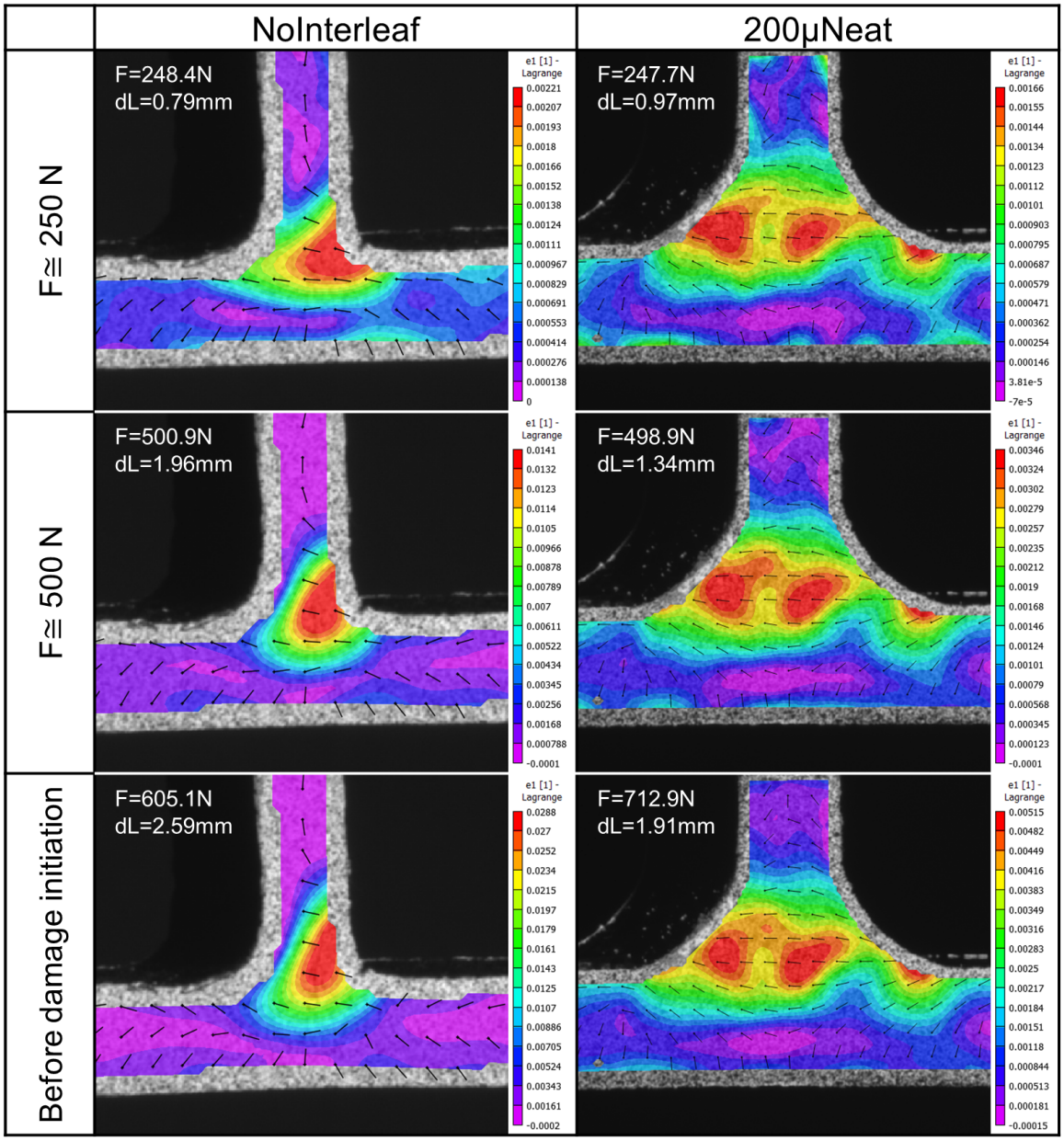

Figure 5.3: T-joint major strain field at various points during test - part 1

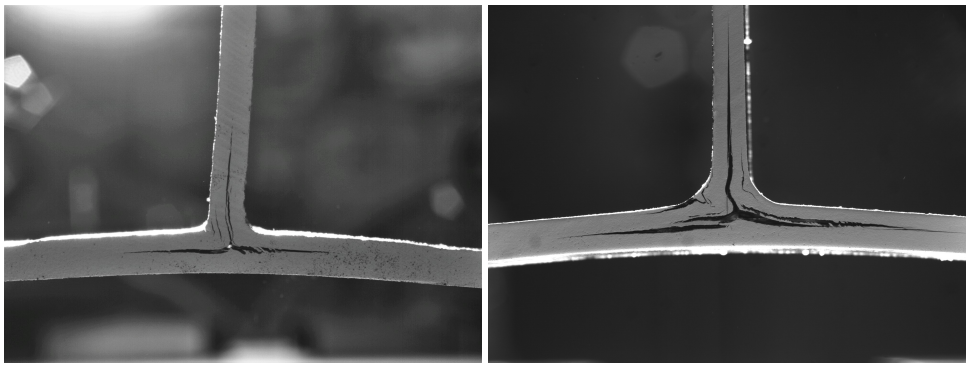

(a) NoInterleaf **(b)** 200µNeat

Figure 5.4: Crack patterns of samples NoInterleaf_1 and 200µNeat_1 near the end of tests

5.2.3. Effect of CNT Interleaves

Peak load, displacement, stiffness and strain energy data of 200µNeat-FibreFillet, 200µCNT, and 500µCNT samples are presented in Table 5.2 alongside group-wise mean and standard deviation values. The load-displacement curves of these samples are presented in Figure 5.5.

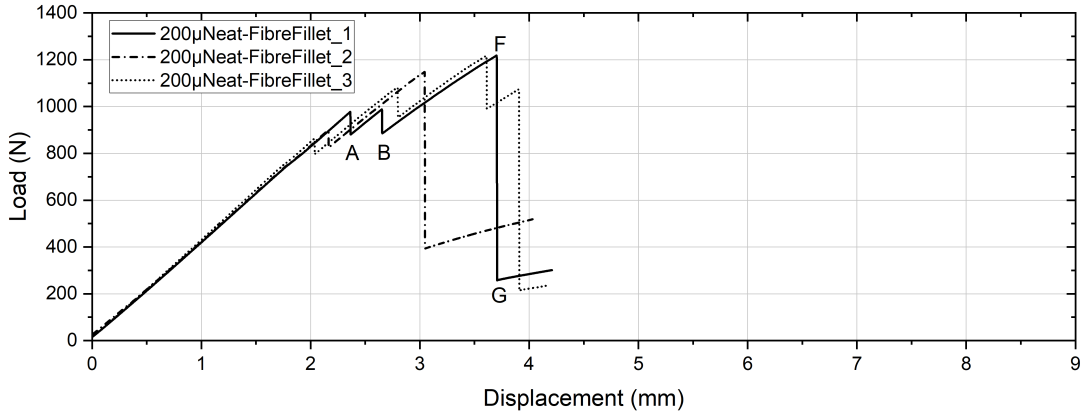

(a) 200µNeat-FibreFillet

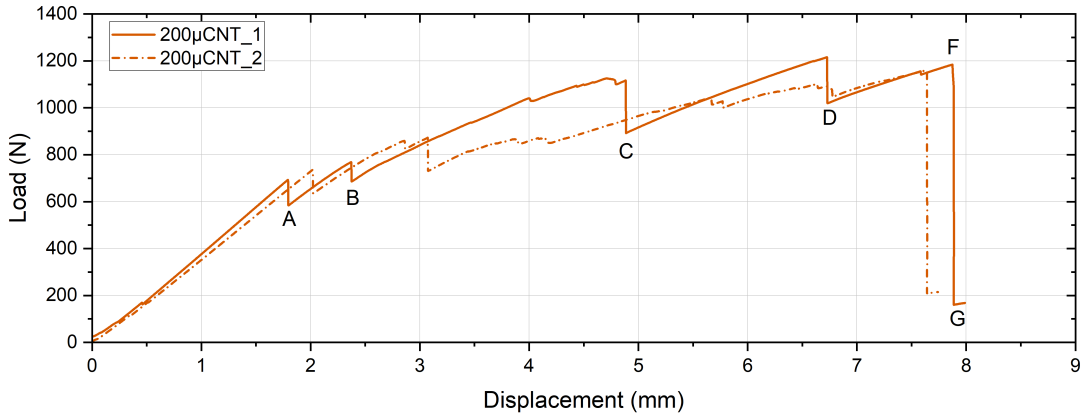

(b) 200µCNT

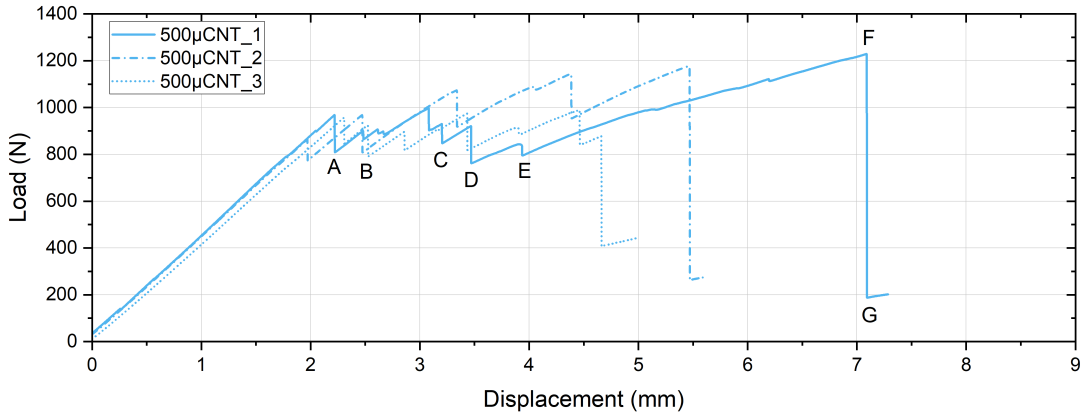

(c) 500µCNT

Figure 5.5: Load-displacement curves from 200µNeat-FibreFillet, 200µCNT and 500µCNT. Letters marking the solid line curves correspond to images in Figure 5.9

The peak loads are similar across the sample groups, although the CNT-modified samples reached the peak loads at higher displacements. No significant change in stiffness was caused by the inclu-

sion of CNT interleaves. While 200µCNT samples do demonstrate a lower stiffness value, this is more likely a result of different geometry (the 200µCNT samples were produced using 2mm-thick caul plates which had a smaller bend radius) than of the difference in material, since the 200µNeat-FibreFillet and 500µCNT samples (both formed by the 3mm-thick caul plates) were very similar in stiffness. Significant improvement in strain energy could be noticed. The 200µCNT group absorbed on average 146% more strain energy in comparison to the baseline 200µNeat-FibreFillet samples. The 500µCNT group also showed gains, albeit less and with more scatter.

The load-displacement curves that exhibit the highest peak load F_{max} within their batch were extracted and plotted together in Figure 5.8 so that the differences could be highlighted. The linear regions of these curves are visualised by the major strain field plots in Figure 5.6 and Figure 5.7. These representative curves were also marked by letters denoting damage progression events. The camera images acquired at these instances are shown in Figure 5.9.

Strain Field Analysis
Figure 5.6 and Figure 5.7 show the major strain fields at F≅250N, 500N and 750N, as well as right before damage initiation. Each row in Figure 5.6 contains contours plotted on the same colour scale, as the strain values are comparable in value. An additional contour was plotted for the 200µNeat-FibreFillet sample since its speckle pattern remained mostly intact despite the initial cracks.

Several observations can be made about all three specimens. First, the overall strain field shape is much more symmetric compared to the defective samples presented earlier, suggesting improved manufacturing quality. Second, the highest strain is concentrated in the delta fillet region and in the horizontal direction. This indicates that the stress state in the delta fillet region is a result of the stiffener half laminates attempting to straighten up at the radius bend.

At F≅250N and 500N, shown in Figure 5.6, higher strains can be noticed in the 200µCNT sample compared to the other two. This is, however, more likely a result of the different geometry than the material. The 200µCNT samples had the smallest delta fillet and outer bend radius, which may have resulted in slightly higher stresses under the same forces. The hypothesis is further supported by the similar strain fields in the 200µNeat-FibreFillet and 500µCNT samples, which were more similar geometrically. In fact, these two samples were so close in terms of the strain contours that no significant conclusions could be made regarding whether the inclusion of CNT in the delta fillet alters the strain field.

Damage Progression
At the end of the initial linear regimes, damage progression began in all samples but followed rather different trends. The behaviour of each sample group is first separately discussed before cross-group comparisons are made to shed light on the effect of CNT interleaves on the mechanical behaviour of T-joints.

The 200µNeat-FibreFillet samples saw damage initiation at loads between 800N and 1000N. A series of two small load drops (points A and B in Figure 5.5a) correspond to two small delaminations in the outermost 0/45 ply interface in the radius bend region, away from the delta fillet. While not initially expected, this was not surprising as the test specimens' flanges were longer than in the reference literature, exerting higher bending moments at the bend. The damage events are visualised in Figure 5.9. The cracks are highlighted in red in the bottom row of the table and overlaid onto the sample cross-section micrographs captured before testing to indicate their locations.

After the outer ply cracks formed, further damage progression began to engage delta fillets and interleaves. The 200µNeat-FibreFillet samples saw the load continue increasing linearly at almost the same rate with no visible crack propagation (as shown by point F in Figure 5.5a and Figure 5.9) until a sudden failure event took place in which a crack split the UD fibre delta fillet into two, propagated upwards in between the fillet and the innermost ply then further in the web, while the flanges separated from the skin. The small load drop seen in the load-displacement curve of 200µNeat-FibreFillet_3 immediately preceding the final failure corresponds to additional delamination in the radius bend, but the sudden

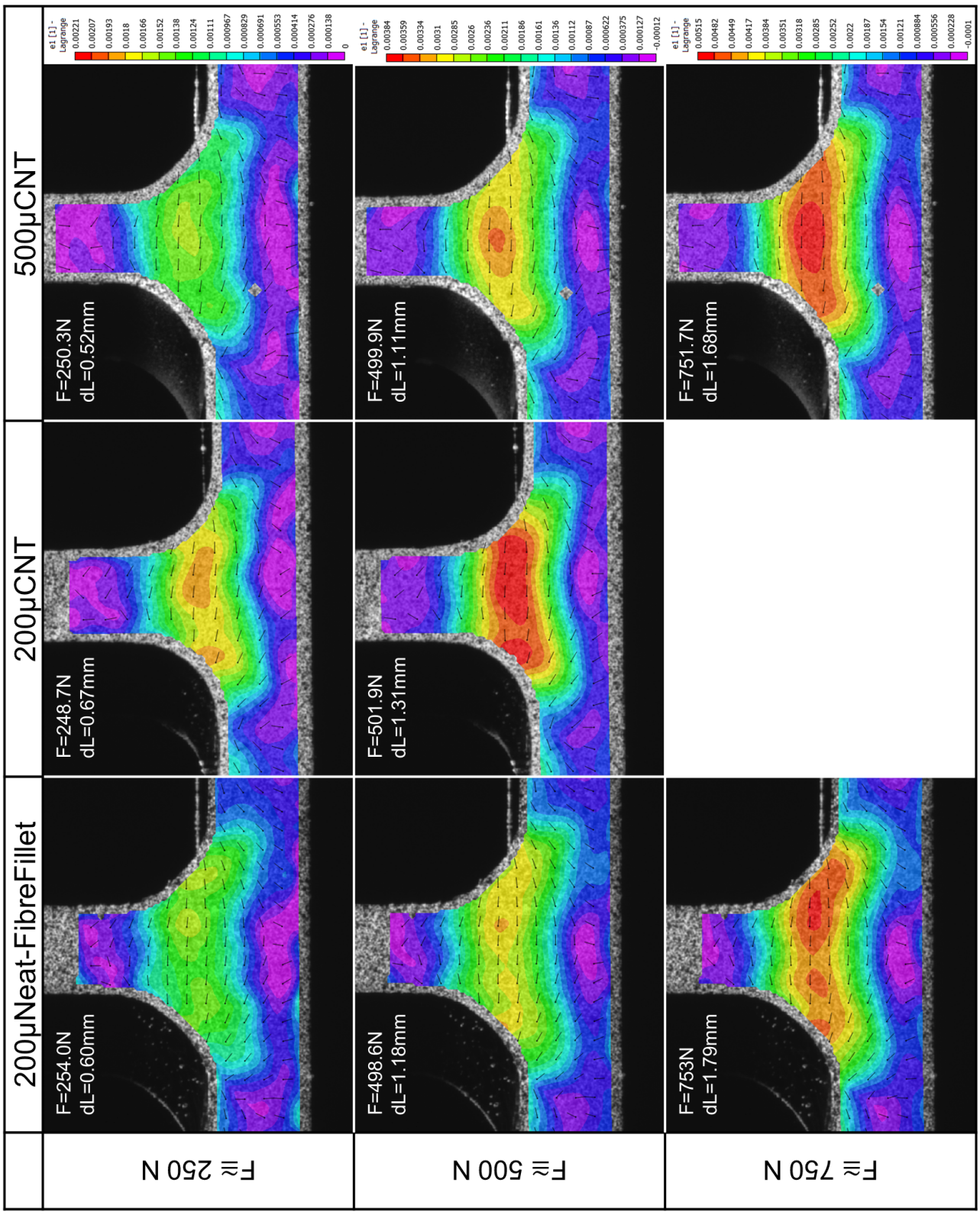

Figure 5.6: T-joint major strain field at various points during test - part 2

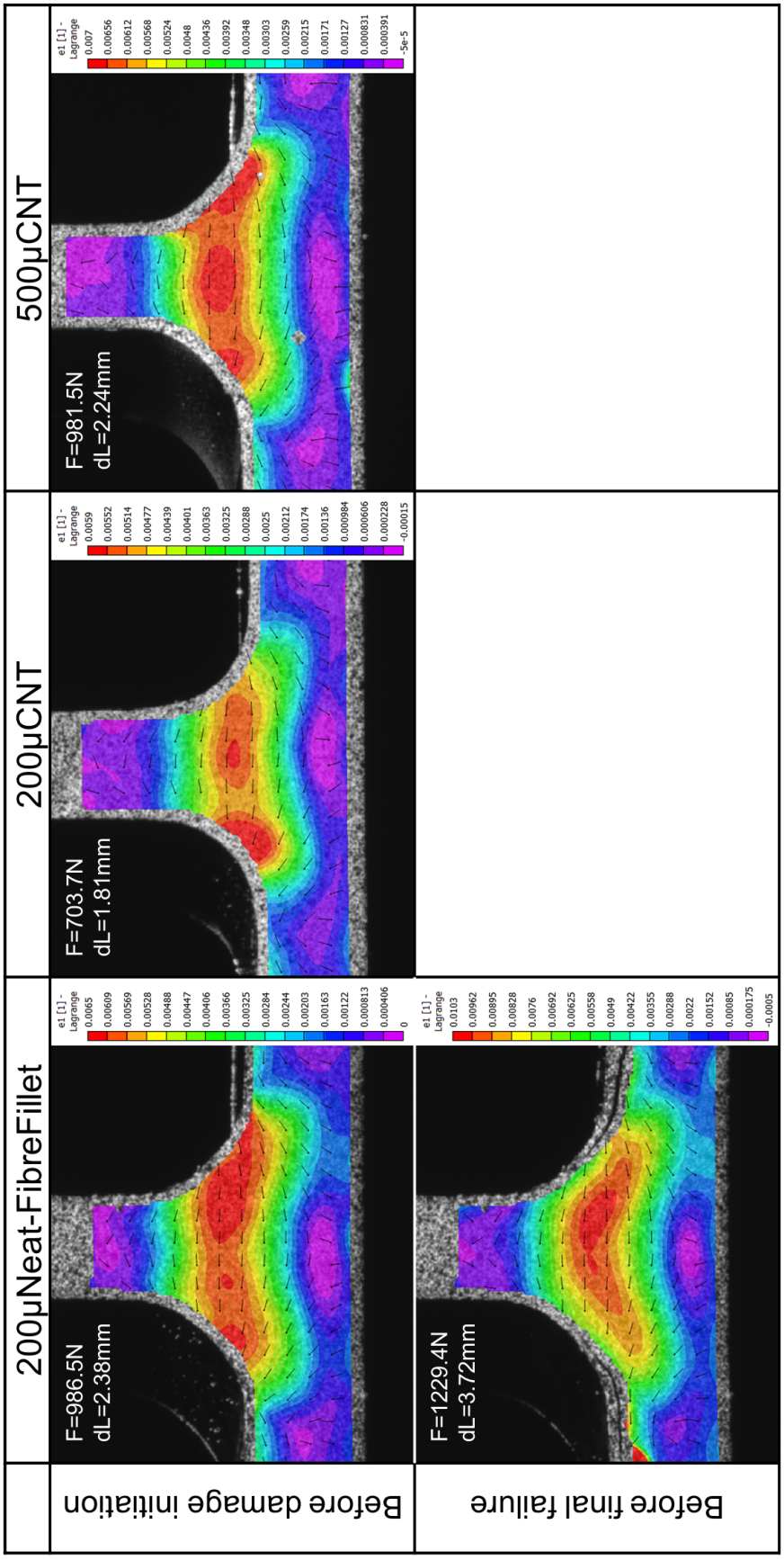

Figure 5.7: T-joint major strain field at various points during test - part 3

manner in which the joint failed was consistent across all three samples.

In the 200µCNT samples, damage also began with delaminations in between outer plies. The cracks appeared earlier, under a load of around 700N, and in the second 0/45 interface counting from the surface as can be seen in Figure 5.9. After the outer ply cracks formed, damage migrated into the interface between the laminate and the delta fillet and propagated into the interleaves between the skin and the flange. Points C and D in Figure 5.5b and Figure 5.9 represent two larger crack openings in the interleaves. Otherwise, the cracks expanded slowly and in small steps, which created tortuous curves and numerous small load drops. As cracks lengthened, the stiffness of the structure gradually decreased. The steady damage progression would continue until the peak load was reached, at which point the stringer and the delta fillet would explosively separate from the skin laminate. Points F and G show the T-joint immediately before and after the final failure. It can be seen that cracks have fully propagated through the interleaves before failure took place. The two 200µCNT samples failed at similar loads and displacements.

Initial damage in the 500µCNT samples appeared in the outermost 0/45 ply interface at similar loads and displacements as 200µNeat-FibreFillet. The damage progression that followed was similar to what was observed in the 200µCNT samples, which saw cracks migrating to the interleaves. The difference was that in the 500µCNT groups, cracks also developed simultaneously in a 0/45 ply interface parallel to the delta fillet radius. The parallel crack development can be observed in images C, D, E and F in Figure 5.9. The three samples in the group exhibited similar trends of damage progression, but a large scatter can be observed in terms of the displacement at failure and strain energy. Geometric imperfections are a probable cause for the scatter. As presented in Table 2.1, the 500µCNT samples showed the highest deviation in delta fillet area, which has been identified as a cause of statistical variation [7].

Load-displacement curves from the three representative samples are combined in one graph in Figure 5.8. No significant difference in stiffness or peak load could be observed. However, the CNT-modified samples were able to delay the final failure to higher displacements. The area under the curve, i.e. strain energy absorption, was also much higher. Steady crack propagation was thought to be the main contributor to the improved strain energy absorption capabilities. As already pointed out, the CNT-modified samples tolerated multiple cracks before failure, while the neat sample failed abruptly with minimum visible damage evolution. The fully developed crack patterns are compared in the bottom row in Figure 5.9.

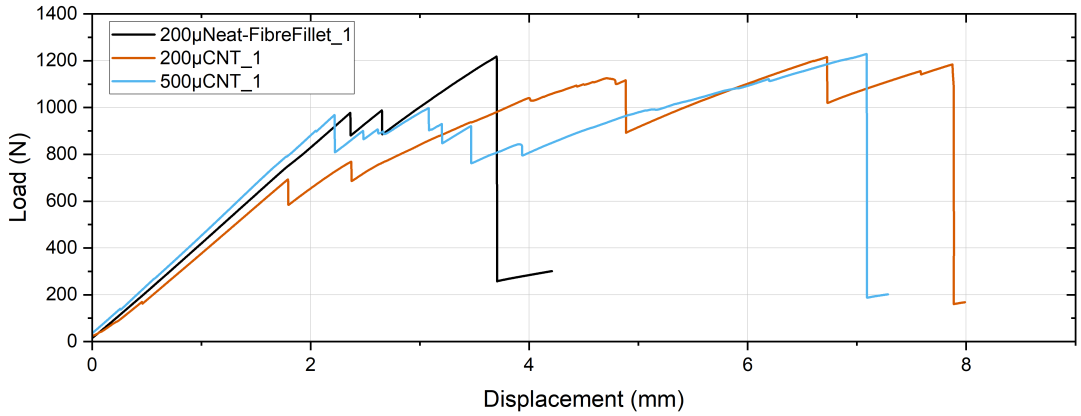

Figure 5.8: Comparison between the load-displacement curves of three representative samples: 200µNeat-FibreFillet_1, 200µCNT_1, and 500µCNT_1

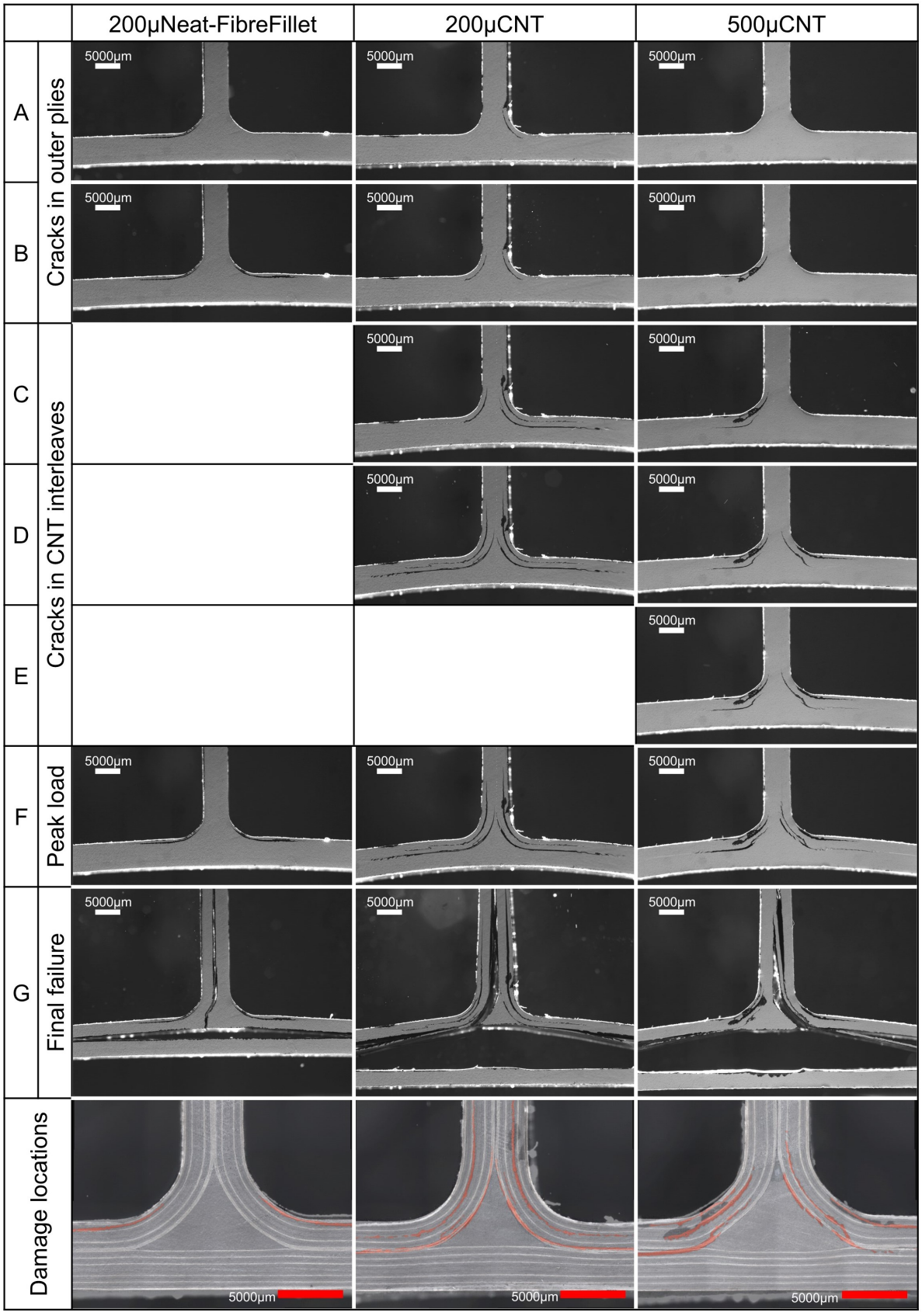

Figure 5.9: Images showing damage progression in the T-joints. The letters map the images onto the load-displacement curves in Figure 5.5. The bottom row shows the crack patterns before final failure (highlighted in red) overlaid onto microscopic images acquired before testing to indicate locations of damages

Crack Surface Inspection

The role of the CNT interleaves was confirmed when the crack surfaces were observed under the microscope. The skin was separated by hand from the samples, as shown in Figure 5.10. The highlighted area - the skin-flange interface close to the delta fillet - was placed under the scope of a Wide-Area 3D Measurement System VR-5000 from Keyence. The micrographs are presented in Figure 5.11. Residual CNT interleaves can be observed on the crack surfaces of 200µCNT and 500µCNT samples, with exposed fibres in between. This suggests that the crack advanced in the interleaf through a mixture of adhesive and cohesive failure. Striations are visible in the residual 500µCNT interleaf, as highlighted in Figure 5.11c. These patterns point to a tortuous crack path which increased the strain energy absorption. The pattern echoes what was previously observed in DCB test sample crack surfaces [19]. While the same striations were not observed in the 200µCNT interleaf in Figure 5.11b, the similar T-joint crack progression patterns suggest that striations might also exist, only on a smaller scale due to the thinner interleaf.

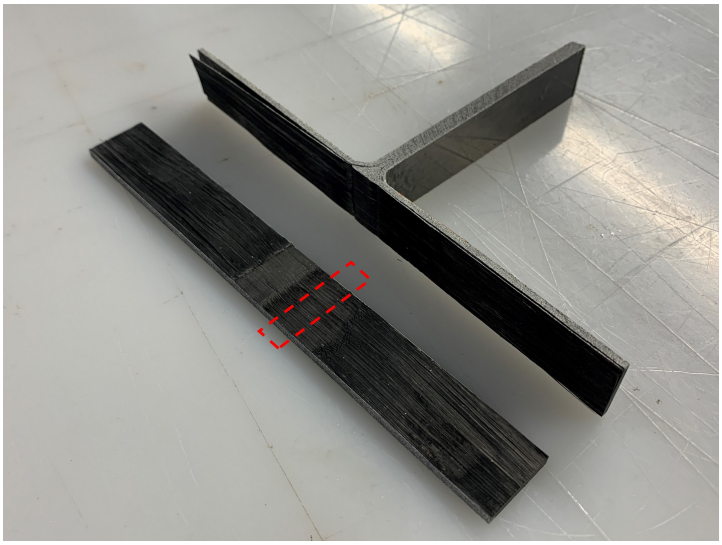

Figure 5.10: T-joint broken for microscopic observation. Box highlights area of observation

In the crack surface of the 200µNeat-FibreFillet sample shown in Figure 5.11a, small echelon cracks can be observed between the fibres. They can be observed in the zoomed-in view. It remains to be investigated whether this pattern was produced by the neat API-60 epoxy interleaf since there were no eligible samples without interleaves to offer the comparison.

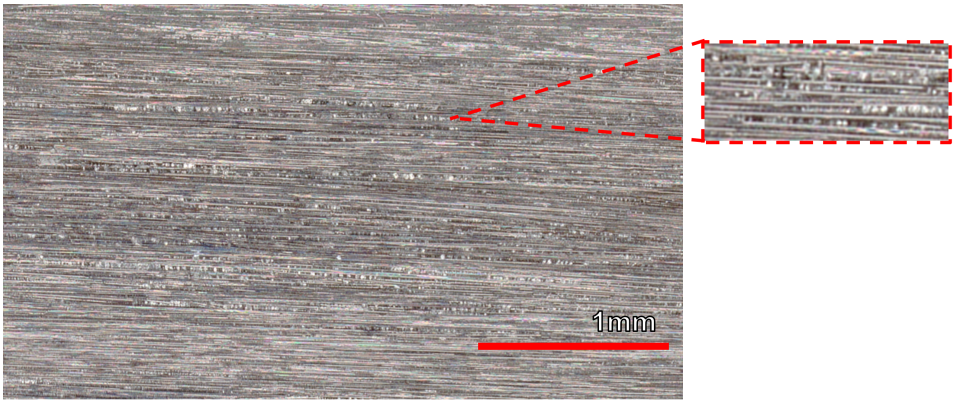

(a) 200µNeat-FibreFillet

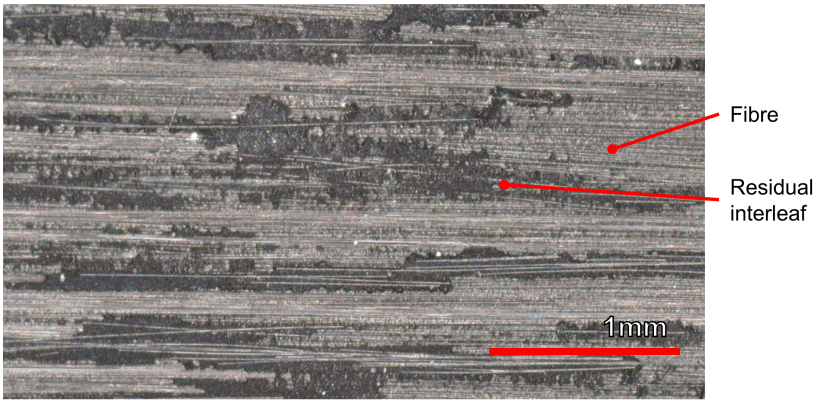

(b) 200µCNT

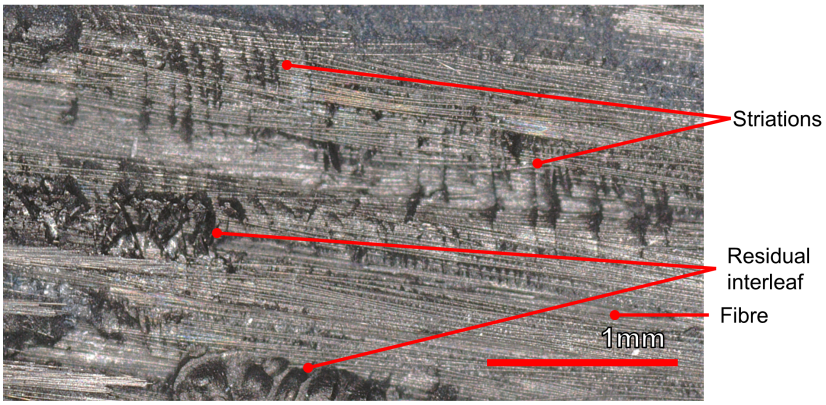

(c) 500µCNT

Figure 5.11: Fracture surfaces

While significant improvements were observed through the inclusion of CNT interleaves, it is difficult to conclude for now whether the thickness of the interleave was the main cause for the differences between the 200µCNT and 500µCNT samples. While it may seem that the 200µCNT group outperformed the 500µCNT group by further delaying failure and absorbing higher strain energy, the variance in geometry and manufacturing quality adds to the uncertainty. Therefore, a definitive conclusion was not made regarding the effect of CNT interleaf thickness.

In summary, test results have demonstrated that the inclusion of CNT interleaves and delta fillets modified the behaviour of the T-joint under a stiffener pull-off load. Despite some scatter in the results arising from geometrical deviations, significant improvements were observed in terms of the displacement at failure and strain energy absorption. The stiffness and ultimate strength were not altered, suggesting that the interleaf targets specifically the damage resistance of the structure. While the baseline

samples would fail abruptly at low displacements, the CNT interleaves delayed the failure by arresting and releasing cracks in the interleaves through a series of small load drops. While the structure displayed softening behaviour as the cracks expanded, it was able to absorb up to 146% higher strain energy before the complete failure of the joint. Micrographs confirmed the existence of tortuous crack paths which likely contributed to the delay of failure. Due to the variability in manufacturing quality, conclusions could not be made about the effect of CNT interleaf thickness on the damage resistance of T-joints.

6

Conclusion and Recommendations

The current research investigated the effect of carbon nanotube (CNT) interleaves on the structural behaviour of carbon fibre composite T-joints. This was achieved by developing a manufacturing pathway for T-joint samples, producing these samples, and testing them mechanically. The test results suggest that the incorporation of CNT interleaves was an effective method to delay the failure of the structure under the given loading conditions.

A composite T-joint is formed when two orthogonal laminates are joined to enable out-of-plane load transfer, forming a T shape. The structure is common in aerospace primary structures including wing boxes [2], [3]. The horizontal laminate of the T-joint is usually referred to as the skin, while the vertical part is termed the web. At the intersection point, the web has to split and make two bends to become the flanges, which are joined to the skin. The web and flanges together form the stiffener. For the sake of fibre continuity and load transfer, carbon fibre plies cannot be bent into a right angle [4]. Instead, a radius bend needs to be formed, leaving a cavity at the intersection between the laminates. The cavity is usually filled by a piece of material called the delta fillet. Typical delta fillet materials include neat resin, continuous fibre, or chopped fibre [5]. In addition to facilitating load transfer, the delta fillet also helps define the geometry of surrounding laminates [3].

The stiffener pull-off test is a common method to evaluate the mechanical behaviour of a T-joint. In such a test, the flanges and skin of the structure are fixed while the web is clamped and a tensile load is applied. The test simulates an out-of-plane load transfer scenario. During the test, structural failure usually occurs as a result of damage within or around the delta fillet, and inside the flange-skin interface [1], [3], [5], [7], [15]. Current methods to reinforce T-joints such as mechanical fasteners, z-pinning [6] and stitching [10], [58] tend to cause different degrees of load discontinuity and stress concentration. In comparison, an interleaf, i.e. a thin layer of material incorporated in between laminates, does not distort fibre orientation, is easy to implement, and has the potential to change the damage resistance of the structure by modifying interfacial bonding properties [14]–[16].

The application of CNT as an interleaf material to composite structures is a topic of ongoing research. As the name suggests, CNT are thin tubes formed by carbon atoms and measure hundreds of nanometers or less [20]. The high strength and surface area of CNT make it a suitable reinforcing phase for modifying interfacial bonding properties. The addition of CNT to polymers [17], [18] saw improved elastic properties, while its inclusion in composite matrix [1] enhanced damage resistance. Compared to modifying the composite matrix with CNT, incorporating CNT interleaves in critical interfaces represents a more efficient and targeted philosophy. Coupon-level testing has recorded significantly higher fracture toughness in samples with CNT-modified epoxy interleaves [19]. The application of CNT interleaves to T-joints is an effort to investigate the method's effectiveness on a structural element level.

A tailored manufacturing pathway was developed for the production of T-joint samples. Forming tools were designed and fabricated, notably employing 3D printing as an efficient production method. T-joint samples were manufactured out of carbon fibre prepreg material (Hexcel IM7/8552) and co-cured in an

autoclave using a vacuum bagging process. Interleaves and delta fillets made of CNT-modified epoxy were embedded in the test group samples, while the control groups contained neat epoxy interleaves or no interleaves at all, and neat epoxy or continuous fibre delta fillets. A semi-curing (B-staging) step was applied to the epoxy interleaves and fillets to ensure geometrical accuracy and facilitate integration [19], [38]. The co-cured samples were measured to assess the quality, and severe defects were identified in the samples with neat epoxy interleaves due to squeeze-out during the cure cycle. The samples with neat epoxy interleaves and continuous fibre delta fillets were of admissible quality, as were the ones with CNT-modified delta fillets and interleaves.

Stiffener pull-off tests were conducted to characterise the mechanical behaviour of T-joint samples. The test was performed on a tensile testing machine with displacement-controlled loading. A Digital Image Correlation (DIC) system was set up to extract displacement and strain information which complemented the load-displacement output from the testing machine. Data post-processing enabled comparison between samples based on stiffness, strength, displacement at failure, strain energy absorption, strain fields and damage evolution patterns.

Test results revealed significant improvements in the T-joint's damage resistance owing to the incorporation of CNT interleaves. Notably, the CNT-modified samples failed at higher displacements and were able to absorb up to 146% higher strain energy up to failure compared to the neat samples. The delay of failure was enabled by steady crack propagation in the CNT interleaves. In most cases, damage initiated in outer ply interfaces, migrated inwards to the border of the delta fillet, and expanded in the stiffener-skin interface in gradual steps accompanied by small load drops. Observation of the crack surface revealed evidence of tortuous crack paths. In comparison, the neat samples failed abruptly after minimum visible damage evolution, at lower displacements, and absorbed lower strain energy. On the other hand, the stiffness and ultimate strength of the T-joint were not significantly altered by the inclusion of CNT interleaves.

The results suggest that the CNT interleaves were able to modify the failure resistance of the T-joint structure in a targeted manner, without altering other mechanical characteristics such as the stiffness and ultimate strength. The finding has several implications for structural applications. First, the CNT interleaf can be added to existing structural designs without requiring major design reviews or changes to the manufacturing process. Second, the steady damage progression opens up a bigger window for structural health inspection. Overloaded joints can be identified in a more timely manner. If a correlation between the damage size and loading capability were established, inspection results could be used to determine the worthiness or predict the remaining life of the structure.

6.1. Recommendations

Upon examination of the thesis research, several areas were identified where further improvements would be possible. The findings of the experiments also point to new research directions. Therefore, the following recommendations are made for future efforts to investigate similar topics:

- **Control over post-cure interleaf thickness.** A high degree of thickness reduction was observed in the CNT-modified epoxy interleaf layers, likely the combined result of squeeze-out and compaction. The former can potentially be alleviated by the addition of resin dams [15] to the autoclave setup, while the latter requires more extensive characterisation.

- **Tooling design for even compaction.** While the caul plates adopted in the manufacturing procedures greatly improved the quality of test specimens, non-uniform compaction was noted as a disadvantage of the technique. The plates were successful in evenly distributing the compaction pressure over flat parts of the T-joints, but had trouble handling more complex geometry, i.e. the radius bend. As a result, the interleaf thickness was inconsistent at the bend region and, in rare cases, resin pockets formed between plies. Flexible tooling [9], [70] is a potential solution.

- **Delta fillet forming technique.** The deviation from the design of the CNT-epoxy delta fillets was a major source of scattering in the results. The CNT-modified epoxy paste was difficult to shape

accurately using the current methods. More precise moulding techniques should be developed.

- **Partial curing (B-staging) of neat epoxy.** The squeeze-out of the neat API-60 epoxy delta fillet was the most prominent manufacturing defect encountered. As far as the current research is concerned, UD prepreg was a better solution for making the delta fillet compared to B-staged epoxy. Further research into the applications of B-staged epoxy can benefit from a better understanding of the relationship between its properties and the B-staging and autoclave curing cycles.

- **Modified layup design.** The test sample could benefit from a thicker and stiffer skin laminate layup. The adopted layup was susceptible to excess deformation under loading and introduced undesired strain to the stiffener, causing damage to initiate in between the outer plies. A thicker skin that deforms less under the same bending moment would help limit the stress concentration to the delta fillet region and allow for a better evaluation of material properties.

- **In-situ C-scan for crack propagation monitoring.** A handheld ultrasonic C-scanner or a similar device could be employed during the test campaign. Intermittent scans can be performed to construct a holistic picture of the crack front as it propagates through the structure.

- **Control group without interleaves.** Due to severe manufacturing defects, the NoInterleaf samples were not able to provide useful test data for comparison with the CNT-modified samples. However, such a control group would serve as a more ideal baseline, as the neat epoxy interleaf was also shown to improve interfacial fracture toughness [38].

- **Interleaves in more realistic layups.** In this research, the interleaves were only embedded in 0/0 interfaces. While this was the logical choice based on previous research, it does not faithfully represent aerospace structural components where delamination usually occurs between 45° surface plies [71]. It would therefore be interesting to investigate the performance of CNT interleaves embedded in a 45° ply interface between the skin and the stiffener.

- **Structure health monitoring (SHM) applications.** The progressive crack propagation enabled by CNT interleaves promises the potential establishment of a correlation between the remaining life of the structure and the crack size detected by SHM methods such as ultrasonic C-scan. Measuring the electrical properties of CNT interleaf-modified structures could also potentially help detect and measure cracks [8], [44].

References

[1] A. R. Ravindran, R. B. Ladani, C. H. Wang, and A. P. Mouritz, "Strengthening of composite T-joints using 1D and 2D carbon nanoparticles," *Composite Structures*, vol. 255, p. 112 982, 2021. DOI: https://doi.org/10.1016/j.compstruct.2020.112982.

[2] P. B. Stickler and A. Ramulu, "Experimental study of composite T-joints under tensile and shear loading," *Advanced Composite Materials*, vol. 15, no. 2, pp. 193–210, 2006. DOI: 10.1163/156855106777873914.

[3] V. Dahmen, A. J. Redmann, J. Austermann, A. L. Quintanilla, S. J. Mecham, and T. A. Osswald, "Fabrication of hybrid composite T-joints by co-curing with 3D printed dual cure epoxy," *Composites Part B: Engineering*, vol. 183, p. 107 728, 2020. DOI: https://doi.org/10.1016/j.compositesb.2019.107728.

[4] Z. Sápi, R. Butler, and A. Rhead, "Filler materials in composite out-of-plane joints – a review," *Composite Structures*, vol. 207, pp. 787–800, 2019. DOI: https://doi.org/10.1016/j.compstruct.2018.09.102.

[5] L. Burns, A. P. Mouritz, D. Pook, and S. Feih, "Strengthening of composite T-joints using novel ply design approaches," *Composites Part B: Engineering*, vol. 88, pp. 73–84, 2016. DOI: https://doi.org/10.1016/j.compositesb.2015.10.032.

[6] F. Bianchi, T. M. Koh, X. Zhang, I. K. Partridge, and A. P. Mouritz, "Finite element modelling of z-pinned composite T-joints," *Composites Science and Technology*, vol. 73, pp. 48–56, 2012. DOI: https://doi.org/10.1016/j.compscitech.2012.09.008.

[7] R. S. Trask, S. R. Hallett, F. M. M. Helenon, and M. R. Wisnom, "Influence of process induced defects on the failure of composite T-joint specimens," *Composites Part A: Applied Science and Manufacturing*, vol. 43, no. 4, pp. 748–757, 2012. DOI: https://doi.org/10.1016/j.compositesa.2011.12.021.

[8] Y. Wan, W. L. Hu, B. Yang, *et al.*, "On-line tensile damage monitoring of WGF/epoxy T-joint by the embedded MWCNT@WGF sensor," *Composites Communications*, vol. 23, p. 7, 2021. DOI: 10.1016/j.coco.2020.100541.

[9] X. Wang, F. Xie, M. Li, and Z. Zhang, "Experimental investigation of the compaction and tensile strength of co-cured skin-to-stiffener structures," *Applied Composite Materials*, vol. 18, no. 5, pp. 371–383, 2011. DOI: 10.1007/s10443-010-9162-y.

[10] J. Bigaud, Z. Aboura, A. T. Martins, and S. Verger, "Analysis of the mechanical behavior of composite T-joints reinforced by one side stitching," *Composite Structures*, vol. 184, pp. 249–255, 2018. DOI: 10.1016/j.compstruct.2017.06.041.

[11] J. Chen, E. Ravey, S. Hallett, M. Wisnom, and M. Grassi, "Prediction of delamination in braided composite T-piece specimens," *Composites Science and Technology*, vol. 69, no. 14, pp. 2363–2367, 2009. DOI: https://doi.org/10.1016/j.compscitech.2009.01.027.

[12] T. Ekermann and S. Hallstrom, "Pull-off tests of CFRP T-joints with conventional and 3D reinforced fillets," *Composite Structures*, vol. 223, 2019. DOI: 10.1016/j.compstruct.2019.110893.

[13] H. Gulasik and D. Coker, "Delamination-debond behaviour of composite T-joints in wind turbine blades," in *5th Science of Making Torque from Wind Conference*, ser. Journal of Physics Conference Series, vol. 524, 2014. DOI: 10.1088/1742-6596/524/1/012043.

[14] Q. A. Li, M. Zhu, G. Q. Tao, and C. Xie, "Experimental and numerical investigation of T-joints with multiwalled carbon nanotubes," *Polymer Composites*, vol. 42, no. 4, pp. 2135–2146, 2021. DOI: 10.1002/pc.25965.

[15] Z. Sápi, S. Hutchins, R. Butler, and A. Rhead, "Novel filler materials for composite out-of-plane joints," *Composite Structures*, vol. 229, 2019. DOI: 10.1016/j.compstruct.2019.111382.

[16] Y. Wang and C. Soutis, “Fatigue behaviour of composite T-joints in wind turbine blade applications,” *Applied Composite Materials*, vol. 24, no. 2, pp. 461–475, 2017. DOI: 10.1007/s10443-016-9537-9.

[17] T. Liu, I. Y. Phang, L. Shen, S. Y. Chow, and W.-D. Zhang, “Morphology and mechanical properties of multiwalled carbon nanotubes reinforced nylon-6 composites,” *Macromolecules*, vol. 37, no. 19, pp. 7214–7222, 2004. DOI: 10.1021/ma049132t.

[18] S. L. Ruan, P. Gao, X. G. Yang, and T. X. Yu, “Toughening high performance ultrahigh molecular weight polyethylene using multiwalled carbon nanotubes,” *Polymer*, vol. 44, no. 19, pp. 5643–5654, 2003. DOI: https://doi.org/10.1016/S0032-3861(03)00628-1.

[19] N. Subramanian and C. Bisagni, “Damage arrest mechanisms in nanoparticle interleaved composite interfaces,” in *Composites Meet Sustainability: Proceedings of the 20th European Conference on Composite Materials*, 2022.

[20] D. De Cicco, Z. Asaee, and F. Taheri, “Use of nanoparticles for enhancing the interlaminar properties of fiber-reinforced composites and adhesively bonded joints—a review,” *Nanomaterials*, vol. 7, no. 11, p. 360, 2017.

[21] B. W. Grimsley, R. J. Cano, M. C. Kinney, *et al.*, “Characterization of hybrid CNT polymer matrix composites,” in *SAMPE Technical Conference*, pp. 18–21.

[22] F. H. Gojny, M. H. G. Wichmann, B. Fiedler, and K. Schulte, “Influence of different carbon nanotubes on the mechanical properties of epoxy matrix composites – a comparative study,” *Composites Science and Technology*, vol. 65, no. 15, pp. 2300–2313, 2005. DOI: https://doi.org/10.1016/j.compscitech.2005.04.021.

[23] J. M. Wernik and S. A. Meguid, “On the mechanical characterization of carbon nanotube reinforced epoxy adhesives,” *Materials & Design*, vol. 59, pp. 19–32, 2014. DOI: https://doi.org/10.1016/j.matdes.2014.02.034.

[24] M. C. Weisenberger, E. A. Grulke, D. Jacques, A. T. Rantell, and R. Andrewsa, “Enhanced mechanical properties of polyacrylonitrile/multiwall carbon nanotube composite fibers,” *Journal of Nanoscience and Nanotechnology*, vol. 3, no. 6, pp. 535–539, 2003. DOI: 10.1166/jnn.2003.239.

[25] W. Zhang, R. C. Picu, and N. Koratkar, “The effect of carbon nanotube dimensions and dispersion on the fatigue behavior of epoxy nanocomposites,” *Nanotechnology*, vol. 19, no. 28, p. 285 709, 2008. DOI: 10.1088/0957-4484/19/28/285709.

[26] Y. Han and J. Elliott, “Molecular dynamics simulations of the elastic properties of polymer/carbon nanotube composites,” *Computational Materials Science*, vol. 39, no. 2, pp. 315–323, 2007. DOI: https://doi.org/10.1016/j.commatsci.2006.06.011.

[27] N. Subramanian, A. Rai, and A. Chattopadhyay, “Atomistically informed stochastic multiscale model to predict the behavior of carbon nanotube-enhanced nanocomposites,” *Carbon*, vol. 94, pp. 661–672, 2015. DOI: https://doi.org/10.1016/j.carbon.2015.07.051.

[28] Q. Liu, S. V. Lomov, and L. Gorbatikh, “Spatial distribution and orientation of nanotubes for suppression of stress concentrations optimized using genetic algorithm and finite element analysis,” *Materials & Design*, vol. 158, pp. 136–146, 2018. DOI: https://doi.org/10.1016/j.matdes.2018.08.019.

[29] Q. Liu, S. V. Lomov, and L. Gorbatikh, “The interplay between multiple toughening mechanisms in nanocomposites with spatially distributed and oriented carbon nanotubes as revealed by dual-scale simulations,” *Carbon*, vol. 142, pp. 141–149, 2019. DOI: https://doi.org/10.1016/j.carbon.2018.10.005.

[30] Q. Liu, S. V. Lomov, and L. Gorbatikh, “Enhancing strength and toughness of hierarchical composites through optimization of position and orientation of nanotubes: A computational study,” *Journal of Composites Science*, vol. 4, no. 2, p. 34, 2020.

[31] “Standard test method for mode I interlaminar fracture toughness of unidirectional fiber-reinforced polymer matrix composites,” ASTM International, Standard, 2007.

[32] "Standard test method for determination of the mode II interlaminar fracture toughness of unidirectional fiber-reinforced polymer matrix composites," ASTM International, Standard, 2019.

[33] R. B. Ladani, A. R. Ravindran, S. Wu, *et al.*, "Multi-scale toughening of fibre composites using carbon nanofibres and z-pins," *Composites Science and Technology*, vol. 131, pp. 98–109, 2016. DOI: https://doi.org/10.1016/j.compscitech.2016.06.005.

[34] F. H. Gojny, M. H. G. Wichmann, B. Fiedler, W. Bauhofer, and K. Schulte, "Influence of nano-modification on the mechanical and electrical properties of conventional fibre-reinforced composites," *Composites Part A: Applied Science and Manufacturing*, vol. 36, no. 11, pp. 1525–1535, 2005. DOI: https://doi.org/10.1016/j.compositesa.2005.02.007.

[35] H. Mei, J. Xia, D. Zhang, H. Li, Q. Bai, and L. Cheng, "Mechanical properties of carbon fiber reinforced bisphenol a dicyanate ester composites modified with multiwalled carbon nanotubes," *Journal of Applied Polymer Science*, vol. 134, no. 29, p. 45 100, 2017. DOI: https://doi.org/10.1002/app.45100.

[36] J. A. Rodríguez-González, C. Rubio-González, M. Jiménez-Mora, L. Ramos-Galicia, and C. Velasco-Santos, "Influence of the hybrid combination of multiwalled carbon nanotubes and graphene oxide on interlaminar mechanical properties of carbon fiber/epoxy laminates," *Applied Composite Materials*, vol. 25, no. 5, pp. 1115–1131, 2018. DOI: 10.1007/s10443-017-9656-y.

[37] K. N. Shivakumar, R. Panduranga, and M. Sharpe, "Interleaved polymer matrix composites-a review," in *54th AIAA/ASME/ASCE/AHS/ASC structures, structural dynamics, and materials conference*, p. 1903.

[38] N. Subramanian and C. Bisagni, "Multiscale damage in co-cured composites—perspectives from experiments and modelling," in *ASC 36th Annual Technical VIRTUAL Conference: Composites Ingenuity Taking on Challenges in Environment-Energy-Economy*, 2021, pp. 1479–1492.

[39] J. Rouchon, "Certification of large airplane composite structures," in *ICAS Congress Proceedings*, vol. 2, pp. 1439–1447.

[40] T. J. Hank, J. Lee, S. Cassady, S. Kessler, S. Steiner, and B. L. Wardle, "Void-free vacuum-bag-only composite manufacturing with autoclave-grade prepreg using capillary effects of polymer electrospun nanofibers and aerogel nanoporous networks," in *AIAA SCITECH 2022 Forum*. 2022. DOI: 10.2514/6.2022-1094.

[41] J. Lee, S. S. Kessler, and B. L. Wardle, "Void-free layered polymeric architectures via capillary-action of nanoporous films," *Advanced Materials Interfaces*, vol. 7, no. 4, p. 1 901 427, 2020. DOI: https://doi.org/10.1002/admi.201901427.

[42] X. Yao, S. C. Hawkins, and B. G. Falzon, "An advanced anti-icing/de-icing system utilizing highly aligned carbon nanotube webs," *Carbon*, vol. 136, pp. 130–138, 2018. DOI: https://doi.org/10.1016/j.carbon.2018.04.039.

[43] Y. Show, T. Nakashima, and Y. Fukami, "Anticorrosion coating of carbon nanotube/polytetrafluoroethylene composite film on the stainless steel bipolar plate for proton exchange membrane fuel cells," *J. Nanomaterials*, vol. 2013, no. 2514103, Article 2, 2013. DOI: 10.1155/2013/378752.

[44] X. F. Sanchez-Romate, A. Coca, A. Jimenez-Suarez, M. Sanchez, and A. Urenna, "Crack sensing mechanisms of mode-II and skin-stringer joints between dissimilar materials by using carbon nanotubes," *Composites Science and Technology*, vol. 201, p. 10, 2021. DOI: 10.1016/j.compscitech.2020.108553.

[45] H. Toftegaard and A. Lystrup, "Design and test of lightweight sandwich T-joint for naval ships," *Composites Part a-Applied Science and Manufacturing*, vol. 36, no. 8, pp. 1055–1065, 2005. DOI: 10.1016/j.compositesa.2004.10.031.

[46] T. L. Qin, L. B. Zhao, and H. Huang, "Damage investigation and design of woven composite bonded joint," *Key Engineering Materials*, vol. 417-418, pp. 861–864, 2010. DOI: 10.4028/www.scientific.net/KEM.417-418.861.

[47] H. J. Phillips and R. A. Shenoi, "Damage tolerance of laminated tee joints in FRP structures," *Composites Part A: Applied Science and Manufacturing*, vol. 29, no. 4, pp. 465–478, 1998. DOI: https://doi.org/10.1016/S1359-835X(97)00081-X.

[48] R. A. Shenoi and G. L. Hawkins, “Influence of material and geometry variations on the behaviour of bonded tee connections in FRP ships,” *Composites*, vol. 23, no. 5, pp. 335–345, 1992. DOI: https://doi.org/10.1016/0010-4361(92)90333-P.

[49] R. D. Cope and R. B. Pipes, “Design of the composite spar-wingskin joint,” *Composites*, vol. 13, no. 1, pp. 47–53, 1982. DOI: https://doi.org/10.1016/0010-4361(82)90170-7.

[50] S. K. Panigrahi and B. Pradhan, “Delamination damage analyses of FRP composite spar wingskin joints with modified elliptical adhesive load coupler profile,” *Applied Composite Materials*, vol. 15, no. 4, p. 189, 2008. DOI: 10.1007/s10443-008-9067-1.

[51] Z. Sápi, R. Butler, and A. Rhead, “High fidelity analysis to predict failure in T-joints,” *Composite Structures*, vol. 225, p. 111 143, 2019. DOI: https://doi.org/10.1016/j.compstruct.2019.111143.

[52] F. Hélénon, M. R. Wisnom, S. R. Hallett, and R. S. Trask, “Numerical investigation into failure of laminated composite T-piece specimens under tensile loading,” *Composites Part A: Applied Science and Manufacturing*, vol. 43, no. 7, pp. 1017–1027, 2012. DOI: https://doi.org/10.1016/j.compositesa.2012.02.010.

[53] G. A. O. Davies and J. Ankersen, “Virtual testing of realistic aerospace composite structures,” *Journal of Materials Science*, vol. 43, no. 20, pp. 6586–6592, 2008. DOI: 10.1007/s10853-008-2695-x.

[54] J. W. H. Yap, M. L. Scott, R. S. Thomson, and D. Hachenberg, “The analysis of skin-to-stiffener debonding in composite aerospace structures,” *Composite Structures*, vol. 57, no. 1, pp. 425–435, 2002. DOI: https://doi.org/10.1016/S0263-8223(02)00110-1.

[55] J. Van Rijn and J. Wiggenraad, “A seven-point bending test to determine the strength of the skin-stiffener interface in composite aircraft panels,” National Aerospace Laboratory NLR, Report, 2000.

[56] P. B. Stickler, M. Ramulu, and P. S. Johnson, “Experimental and numerical analysis of transverse stitched T-joints in bending,” *Composite Structures*, vol. 50, no. 1, pp. 17–27, 2000. DOI: https://doi.org/10.1016/S0263-8223(00)00006-4.

[57] C. K. Huang and C. Y. Hsu, “Structural integrity of co-cured composite panels,” *Materials and Manufacturing Processes*, vol. 20, no. 5, pp. 739–746, 2005. DOI: 10.1081/AMP-200055132.

[58] D. D. R. Cartié, G. Dell’Anno, E. Poulin, and I. K. Partridge, “3D reinforcement of stiffener-to-skin T-joints by z-pinning and tufting,” *Engineering Fracture Mechanics*, vol. 73, no. 16, pp. 2532–2540, 2006. DOI: https://doi.org/10.1016/j.engfracmech.2006.06.012.

[59] J.-H. Byun, S.-W. Song, C.-H. Lee, M.-K. Um, and B.-S. Hwang, “Impact properties of laminated composites with stitching fibers,” *Composite Structures*, vol. 76, no. 1, pp. 21–27, 2006. DOI: https://doi.org/10.1016/j.compstruct.2006.06.004.

[60] T. M. Koh, S. Feih, and A. P. Mouritz, “Experimental determination of the structural properties and strengthening mechanisms of z-pinned composite T-joints,” *Composite Structures*, vol. 93, no. 9, pp. 2222–2230, 2011. DOI: https://doi.org/10.1016/j.compstruct.2011.03.009.

[61] C. A. Steeves and N. A. Fleck, “In-plane properties of composite laminates with through-thickness pin reinforcement,” *International Journal of Solids and Structures*, vol. 43, no. 10, pp. 3197–3212, 2006. DOI: https://doi.org/10.1016/j.ijsolstr.2005.05.017.

[62] Hexcel Corporation. “Hexply 8552 epoxy matrix product data sheet.” (2020), [Online]. Available: https://www.hexcel.com/user_area/content_media/raw/HexPly_8552_eu_DataSheet.pdf.

[63] Kaneka Aerospace LLC. “Kaneka composite resin API-60.” (2020), [Online]. Available: https://www.kaneka-aerospace.com/.

[64] NanoSperse. “Nanosperse - supply.” (2022), [Online]. Available: https://nanosperse.com/nanosperse-supply/.

[65] Y. C. Shin, W. I. Lee, and H. S. Kim, “Mode II interlaminar fracture toughness of carbon nanotubes/epoxy film-interleaved carbon fiber composites,” *Composite Structures*, vol. 236, p. 111 808, 2020. DOI: https://doi.org/10.1016/j.compstruct.2019.111808.

[66] Ultimaker Support. “Infill settings.” (2022), [Online]. Available: https://support.ultimaker.com/hc/en-us/articles/360012607079-Infill-settings (visited on 05/10/2022).

[67] Agustín Arroyo. “Ultimate guide: How to design for 3D printing.” (2022), [Online]. Available: https://wikifactory.com/+wikifactory/stories/ultimate-guide-how-to-design-for-3d-printing (visited on 01/05/2022).

[68] Correlated Solutions. “Vic-3D 8 testing guide.” (2020), [Online]. Available: https://correlated.kayako.com/article/57-vic-3d-8-manual-and-testing-guide.

[69] Correlated Solutions. “Vic-3D 8 reference manual.” (2020), [Online]. Available: https://correlated.kayako.com/article/57-vic-3d-8-manual-and-testing-guide.

[70] X. Wang, F. Xie, M. Li, and Z. Zhang, “Influence of tool assembly schemes and integral molding technologies on compaction of T-stiffened skins in autoclave process,” *Journal of Reinforced Plastics and Composites*, vol. 29, no. 9, pp. 1311–1322, 2010. DOI: 10.1177/0731684409102765.

[71] A. Raimondo, I. Urcelay Oca, and C. Bisagni, “Influence of interface ply orientation on delamination growth in composite laminates,” *Journal of Composite Materials*, vol. 55, no. 27, pp. 3955–3972, 2021. DOI: 10.1177/00219983211031636.

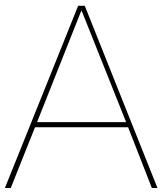

T-Joint Sample Measurements

Table A.1: T-joint sample measurements - part 1

Group	NoInterleaf (T-joint 1)							200µNeat (T-joint 2)						
Interleaf	None							200µ neat API-60						
Delta fillet	Neat API-60							Neat API-60						
Caul plates	-							3mm plates						
Sample	NoInterleaf_1		NoInterleaf_2		NoInterleaf_3		Average [SD]	200µNeat_1		200µNeat_2		200µNeat_3		Average [SD]
Weight (g)	-		-		-		-	39.80		39.80		38.90		39.50 [0.52]
Length (mm)	165.04		164.88		164.64		164.85 [0.20]	164.80		165.00		165.20		165.00 [0.20]
Width (mm)	19.99		19.91		19.98		19.96 [0.04]	19.96		19.97		19.88		19.94 [0.05]
Cross-section measured	1	2	1	2	1	2		1	2	1	2	1	2	
Flange + skin thickness (mm)	5.19	5.48	5.46	5.56	5.53	5.34	5.43 [0.14]	5.21	5.20	5.22	5.17	5.20	5.16	5.19 [0.02]
Web thickness (mm)	4.31	4.62	4.59	4.43	4.64	4.58	4.53 [0.13]	4.37	4.43	4.47	4.50	4.53	4.57	4.48 [0.07]
Outer bend radius - flange A side (mm)	1.06	1.03	0.90	1.07	1.32	0.97	1.06 [0.14]	6.12	6.21	5.74	5.91	6.30	5.71	6.00 [0.25]
Outer bend radius - flange B side (mm)	0.60	0.35	0.38	0.30	0.51	0.61	0.46 [0.13]	5.71	6.61	6.61	6.14	5.86	5.88	6.13 [0.39]
Delta fillet radius - flange A side (mm)	0.42	0.39	0.44	0.41	0.51	0.41	0.43 [0.04]	-	-	-	-	-	-	-
Delta fillet radius - flange B side (mm)	0.45	0.46	0.52	0.63	0.53	0.62	0.53 [0.08]	-	-	-	-	-	-	-
Delta fillet area (mm^2)	0.05	0.08	0.07	0.06	0.06	0.08	0.07 [0.01]	-	-	-	-	-	-	-
Post-cure interleaf thickness - skin-flange (µ)	-	-	-	-	-	-	-	-	-	-	-	-	-	-
Post-cure interleaf thickness - web (µ)	-	-	-	-	-	-	-	-	-	-	-	-	-	-

Table A.2: T-joint sample measurements - part 2

Group	200µNeat-FibreFillet (T-joint 3)							200µCNT (T-joint 4)						
Interleaf	200µ neat API-60							200µ 1% CNT-modified epoxy						
Delta fillet	UD IM7/8552 prepreg							CNT-modified epoxy						
Caul plates	3mm plates							2mm plates						
Sample	200µNeat-FibreFillet_1		200µNeat-FibreFillet_2		200µNeat-FibreFillet_3		Average [SD]	200µCNT_1		200µCNT_2		200µCNT_3		Average [SD]
Weight (g)	41.40		42.00		41.80		41.73 [0.31]	41.20		41.10		40.10		40.80 [0.61]
Length (mm)	164.00		164.00		164.10		164.03 [0.06]	165.00		165.00		165.00		165.00 [0.00]
Width (mm)	20.36		20.39		20.42		20.39 [0.03]	20.00		19.87		19.92		19.93 [0.07]
Cross-section measured	1	2	1	2	1	2		1	2	1	2	1	2	
Flange + skin thickness (mm)	5.53	5.47	5.52	5.46	5.42	5.39	5.47 [0.05]	5.33	5.39	5.36	5.34	5.27	5.24	5.32 [0.06]
Web thickness (mm)	4.85	4.81	4.85	4.75	4.88	4.75	4.82 [0.05]	5.04	5.08	5.07	5.13	5.09	5.14	5.09 [0.04]
Outer bend radius - flange A side (mm)	6.02	6.03	6.37	5.87	6.27	5.94	6.08 [0.20]	4.90	4.57	4.58	4.44	4.45	4.22	4.53 [0.22]
Outer bend radius - flange B side (mm)	5.75	6.32	6.46	6.32	5.71	6.14	6.12 [0.32]	4.41	4.52	4.39	4.54	4.31	4.38	4.42 [0.09]
Delta fillet radius - flange A side (mm)	7.85	7.75	8.56	8.53	8.33	7.48	8.08 [0.45]	6.65	7.66	7.56	8.43	6.58	5.99	7.14 [0.89]
Delta fillet radius - flange B side (mm)	7.66	8.45	9.11	9.18	9.04	8.44	8.65 [0.59]	6.47	7.29	7.47	7.30	6.01	6.41	6.82 [0.60]
Delta fillet area (mm^2)	25.67	26.20	26.10	26.57	26.37	26.29	26.20 [0.31]	19.71	18.81	18.35	17.24	16.77	24.50	19.23 [2.79]
Post-cure interleaf thickness - skin-flange (µ)	-	-	-	-	-	-	-	66.63	46.59	59.57	29.70	47.73	71.37	53.60 [15.34]
Post-cure interleaf thickness - web (µ)	-	-	-	-	-	-	-	153.50	102.72	138.74	199.65	80.32	147.59	137.09 [41.71]

Table A.3: T-joint sample measurements - part 3

Group	500µCNT (T-joint 5)						
Interleaf	500µ 1% CNT -modified epoxy						
Delta fillet	CNT-modified epoxy						
Caul plates	3mm plates						
Sample	500µCNT_1		500µCNT_2		500µCNT_3		Average [SD]
Weight (g)	41.70		42.20		41.40		41.77 [0.40]
Length (mm)	164.40		164.50		164.60		165.50 [0.10]
Width (mm)	19.87		19.98		19.81		19.89 [0.09]
Cross-section measured	1	2	1	2	1	2	
Flange + skin thickness (mm)	5.73	5.69	5.76	5.69	5.74	5.63	5.71 [0.05]
Web thickness (mm)	5.01	5.03	5.00	5.08	5.03	5.03	5.03 [0.03]
Outer bend radius - flange A side (mm)	5.71	6.56	6.24	6.06	6.02	6.21	6.14 [0.28]
Outer bend radius - flange B side (mm)	6.20	6.41	6.36	6.33	6.51	6.36	6.36 [0.10]
Delta fillet radius - flange A side (mm)	7.76	9.22	8.98	8.66	9.78	9.58	9.00 [0.73]
Delta fillet radius - flange B side (mm)	7.47	9.43	9.99	11.40	8.87	8.80	9.33 [1.32]
Delta fillet area (mm^2)	32.21	31.55	31.73	31.00	31.76	32.43	31.78 [0.50]
Post-cure interleaf thickness - skin-flange (µ)	113.66	100.69	132.14	115.08	125.18	100.49	114.54 [12.75]
Post-cure interleaf thickness - web (µ)	136.20	86.44	96.94	121.05	54.34	113.66	101.44 [29.00]

B

Tool Design Drawings

The following drawings present the design and dimensions of the tools used in the manufacturing of the T-joint samples. Only final versions are shown.

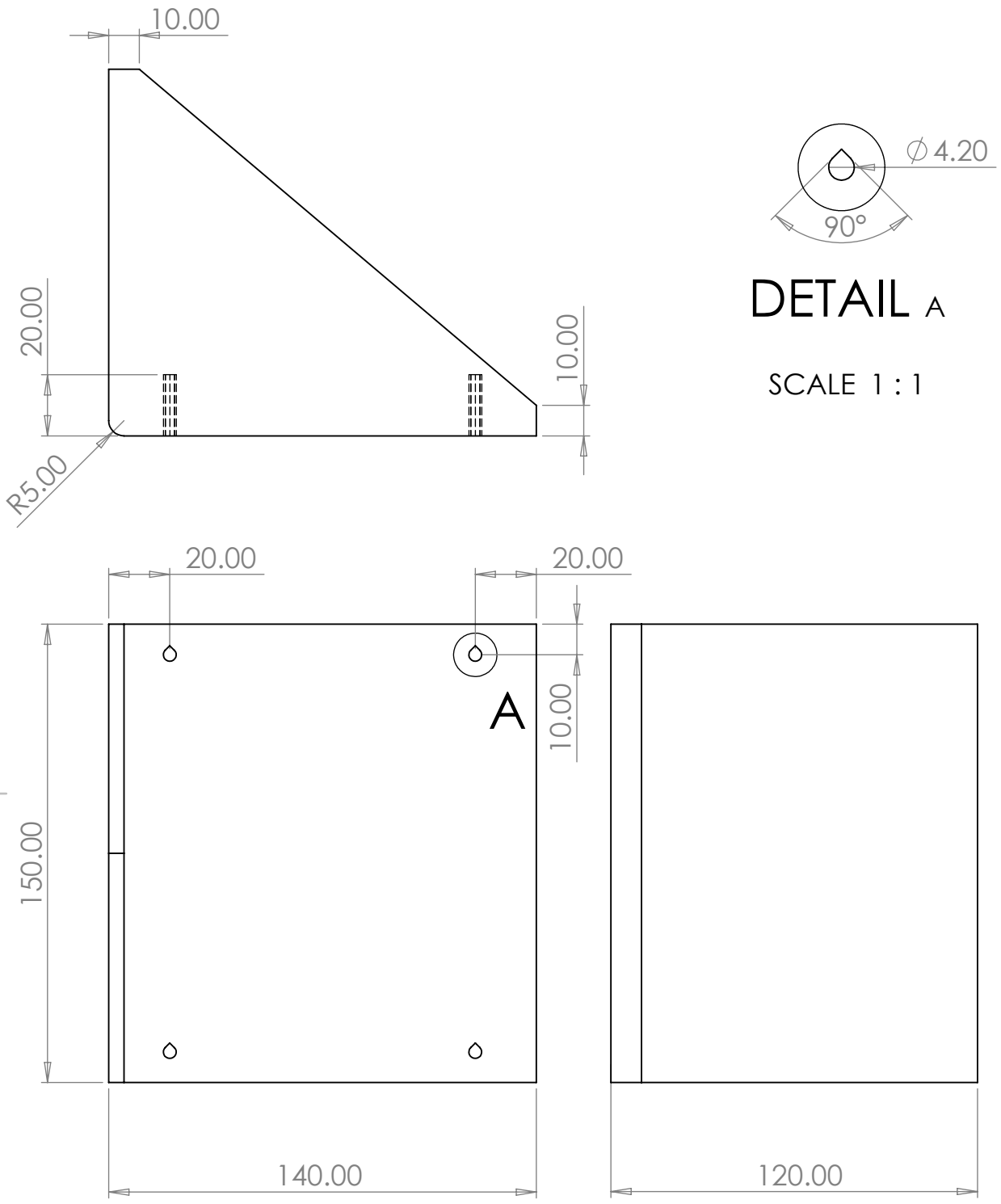

UNLESS OTHERWISE SPECIFIED: DIMENSIONS ARE IN MILLIMETERS

DO NOT SCALE DRAWING | REVISION

	NAME	SIGNATURE	DATE
DRAWN	Danyu Qiao		

TITLE:

3D Printed Wedge Layup Tool

MATERIAL: PLA

DWG NO. 3DPWedge2_1

A4

SCALE:1:2 | SHEET 1 OF 1

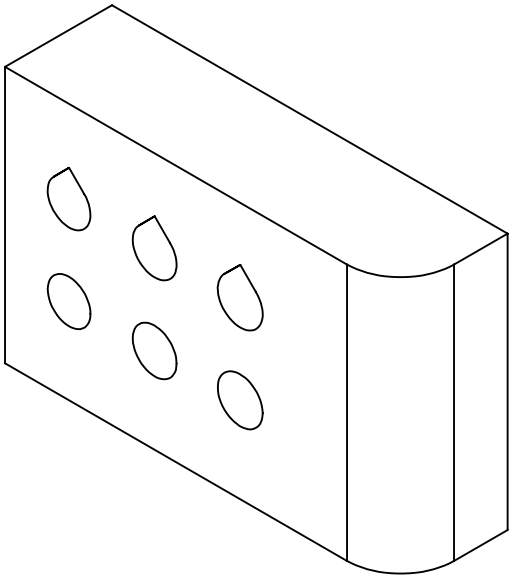

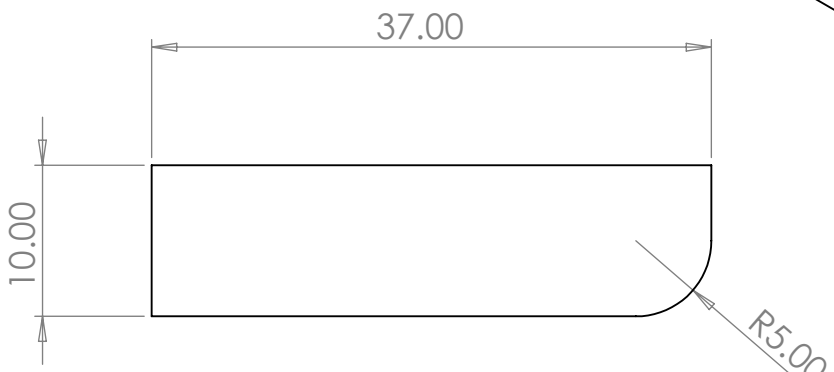

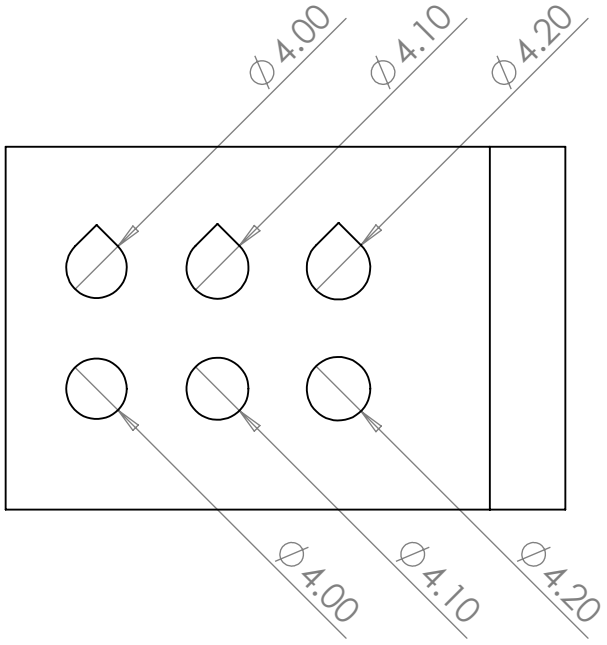

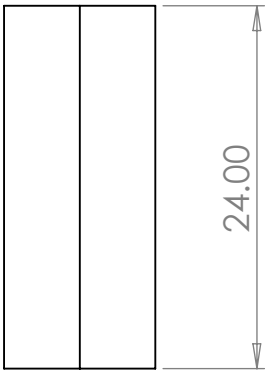

UNLESS OTHERWISE SPECIFIED: DIMENSIONS ARE IN MILLIMETERS

DO NOT SCALE DRAWING

REVISION

	NAME	SIGNATURE	DATE
DRAWN	Danyu Qiao		

TITLE:

3D Printing Test Piece

MATERIAL:

PLA

DWG NO.

3DPTests

A4

SCALE:2:1

SHEET 1 OF 1

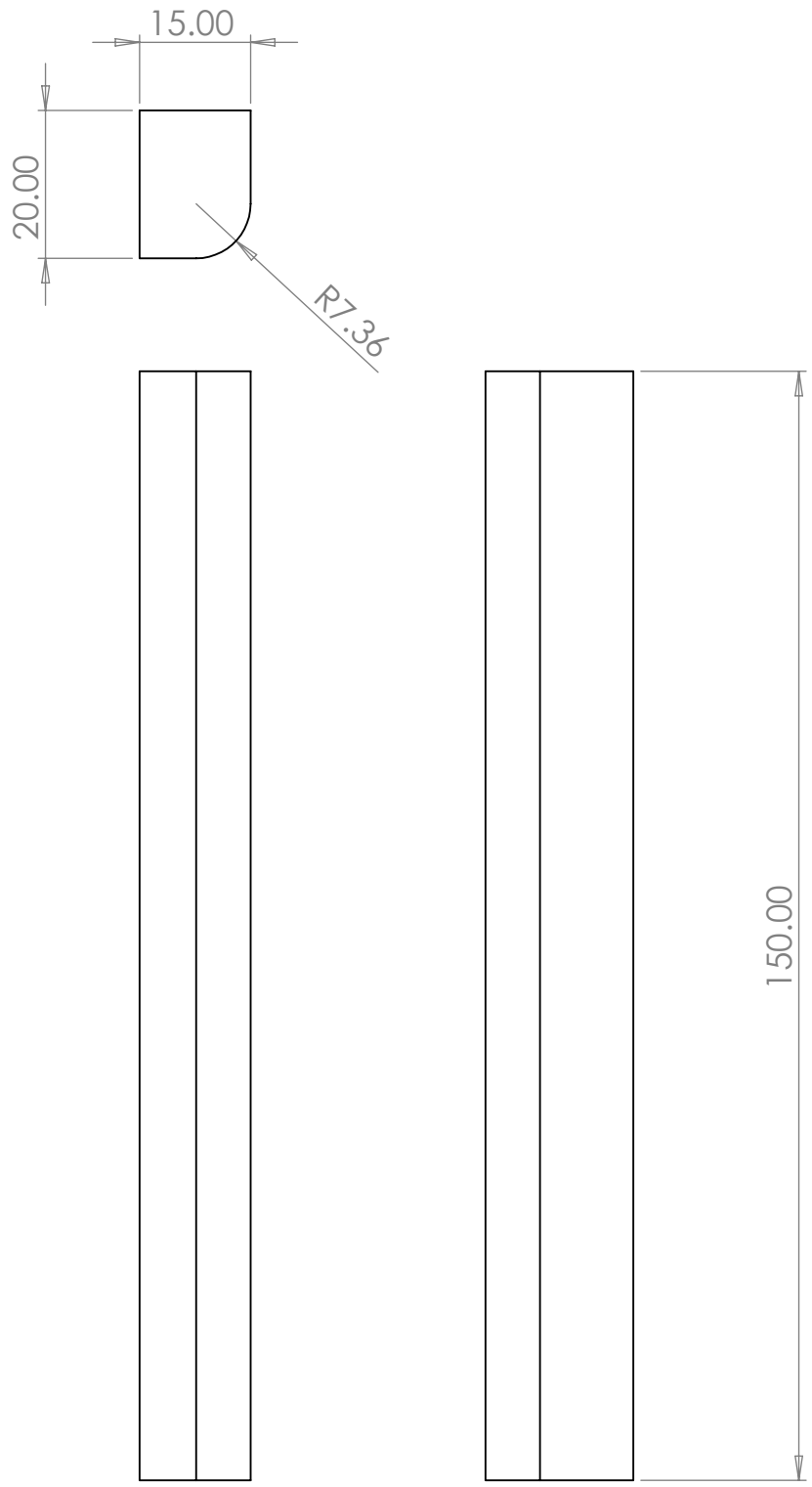

UNLESS OTHERWISE SPECIFIED: DIMENSIONS ARE IN MILLIMETERS

DO NOT SCALE DRAWING

REVISION

	NAME	SIGNATURE	DATE
DRAWN	Danyu Qiao		

TITLE:

Delta Fillet Mould

MATERIAL: PTFE

DWG NO. FilletHalfMould2_0

A4

SCALE:1:1

SHEET 1 OF 1

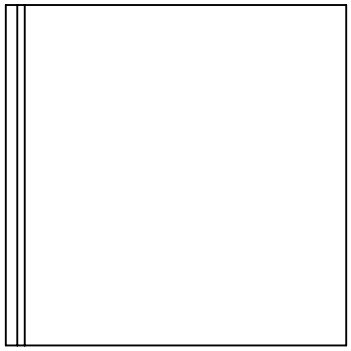

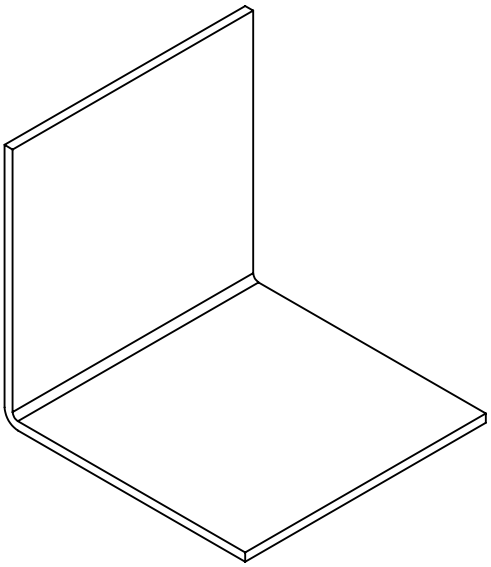

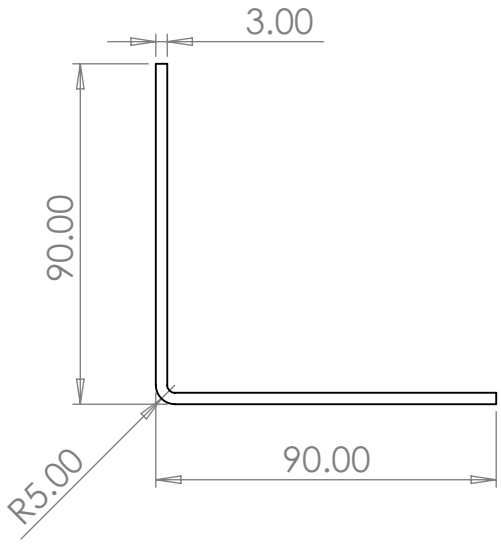

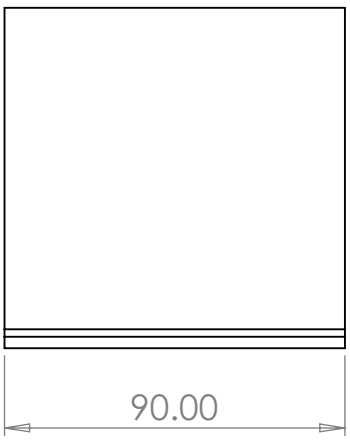

UNLESS OTHERWISE SPECIFIED: DIMENSIONS ARE IN MILLIMETERS						DEBURR AND BREAK SHARP EDGES	DO NOT SCALE DRAWING / REVISION
	NAME	SIGNATURE	DATE				TITLE: Caul Plate
DRAWN	Danyu Qiao						
MFG	DEMO TU Delft						
					MATERIAL: Sheet Aluminium		DWG NO. MouldInBag2_0 / A4
							SCALE:1:2 / SHEET 1 OF 1